FY-2013 FES Joint Research Target Report

JRT 2013 Planning Committee
M. Fenstermacher, A. Garofalo, S.P. Gerhardt, A. Hubbard, R. Maingi, D. Whyte,

Milestone*:*

Conduct experiments and analysis on major fusion facilities, to evaluate stationary enhanced confinement regimes without large Edge Localized Modes (ELMs), and to improve understanding of the underlying physical mechanisms that allow acceptable edge particle transport while maintaining a strong thermal transport barrier. Mechanisms to be investigated can include intrinsic continuous edge plasma modes and externally applied 3D fields. Candidate regimes and techniques have been pioneered by each of the three major US facilities (C-Mod, D3D and NSTX). Coordinated experiments, measurements, and analysis will be carried out to assess and understand the operational space for the regimes. Exploiting the complementary parameters and tools of the devices, joint teams will aim to more closely approach key dimensionless parameters of ITER, and to identify correlations between edge fluctuations and transport. The role of rotation will be investigated. The research will strengthen the basis for extrapolation of stationary regimes which combine high energy confinement with good particle and impurity control, to ITER and other future fusion facilities for which avoidance of large ELMs is a critical issue.

4th Quarter Milestone:

Complete the required experiments and analysis. Prepare a joint report summarizing the contributions toward the development of high-performance stationary regimes devoid of large ELMs, and identifying important paths for future exploration.

This milestone has been completed by the submission of this report.

Table of Contents

Complete Contributor List:

A.M. Garofalo, K.H. Burrell, T.E. Evans, T.H. Osborne, P. Snyder
General Atomics, USA

K. Tritz
Johns Hopkins University, USA

M.E. Fenstermacher
Lawrence Livermore National Laboratory, USA

A. Hubbard, D.G. Whyte, R.M. Churchill, M. Greenwald, N. Howard, J. Hughes, E. Marmar, C. Sung, C. Theiler, J. Walk, A. White
Massachusetts Institute of Technology, USA

J. M. Canik, M.W. Shafer
Oak Ridge National Laboratory, USA

S.P. Gerhardt, R. Maingi, D.J. Battaglia, R.E. Bell, A. Diallo, A. Dominguez, R.J. Goldston, B.A. Grierson, W. Guttenfelder, B.P. LeBlanc, Y. Ren, F. Scotti, W.M. Solomon
Princeton Plasma Physics Laboratory, USA

S. Kubota, N. Crocker
University of California, Los Angeles, USA

I. Cziegler, D. M. Orlov
University of California, San Diego, USA

S. Parker, W. Wan
University of Colorado, Boulder, USA

D.R. Smith
University of Wisconsin-Madison, USA

This research was funded by the United States Department of Energy, under contracts DE-FC02-99ER54512-CMOD, DE-AC52-07NA27344, DE-AC02-09CH11466, DE-FG02-04ER54698, DE-AC05-00OR22725, DE-FG02-04ER54762, DE-FG02-05ER54809, DE-FG02-99ER54527, DE-SC0001288, DE-AC05-00OR22725, DE-FG02-09ER55012 and DE-AC02-09CH11466.

Chapter 1: Executive Summary

1.0 Overview

The H-mode confinement regime is characterized by a region of good thermal and particle confinement at the edge of the confined plasma, and has generally been envisioned as the operating regime for ITER and other next step devices. This good confinement is often interrupted, however, by edge-localized instabilities, known as ELMs. On the one hand, these ELMs provide particle and impurity flushing from the plasma core, a beneficial effect facilitating density control and stationary operation. On the other hand, the ELMs result in a substantial fraction of the edge stored energy flowing in bursts to the divertor and first wall; this impulsive thermal loading would result in unacceptable erosion of these material surfaces if it is not arrested. Hence, developing and understanding operating regimes that have the energy confinement of standard H-mode and the stationarity that is provided by ELMs, while at the same time eliminating the impulsive thermal loading of large ELMs, is the focus of the 2013 FES Joint Research Target (JRT):

Annual Target:

Conduct experiments and analysis on major fusion facilities, to evaluate stationary enhanced confinement regimes without large Edge Localized Modes (ELMs), and to improve understanding of the underlying physical mechanisms that allow acceptable edge particle transport while maintaining a strong thermal transport barrier. Mechanisms to be investigated can include intrinsic continuous edge plasma modes and externally applied 3D fields. Candidate regimes and techniques have been pioneered by each of the three major US facilities (C-Mod, D3D and NSTX). Coordinated experiments, measurements, and analysis will be carried out to assess and understand the operational space for the regimes. Exploiting the complementary parameters and tools of the devices, joint teams will aim to more closely approach key dimensionless parameters of ITER, and to identify correlations between edge fluctuations and transport. The role of rotation will be investigated. The research will strengthen the basis for extrapolation of stationary regimes which combine high energy confinement with good particle and impurity control, to ITER and other future fusion facilities for which avoidance of large ELMs is a critical issue.

Data from the Alcator C-Mod tokamak (MIT), DIII-D tokamak (General Atomics), and NSTX spherical tokamak (PPPL) contribute to this report. Experiments specifically motivated by this research target were conducted on DIII-D, with a national team of researchers from GA, LLNL, PPPL, MIT and ORNL contributing. Both the Alcator C-Mod and NSTX-U teams contributed analysis of previously collected data, as those two facilities did not operate in FY2013. Within each of the three research groups, members from both the host institutions and collaborating institutions made critical contributions. Highlights from these research activities are provided below, with additional details provided in chapters 2-5.

2.0 Highlights from the Alcator C-Mod Contributions

Alcator C-Mod contributions to the JRT focus on the I-mode confinement regime. This regime is characterized by H-mode like temperature pedestals, but L-mode like edge density profiles. As a consequence, ELMs are largely absent in this regime. Particle and impurity transport is provided by a broadband edge fluctuation known as the Weakly Coherent Mode (WCM). Normalized energy confinement at the level needed for ITER has been obtained at low safety factor q_{95} and collisionality. The upper limit in plasma pressure is set either by transitions to H-mode or by available heating power. Stability calculations, and initial experiments with density control, indicate potential to further expand the operating regime to higher density and pressure.

Highlights from the C-Mod contribution towards understanding the physics mechanisms of the particle and thermal transport, and the absence of ELMs, include:

- In the area of assessing operating space and extrapolability of the I-mode regime, databases of global and pedestal I-mode parameters have been significantly expanded to a wide range of plasma dimensional (magnetic field, current, density and power) and dimensionless parameters.
- A major emphasis of 2013 research has been the analysis of profiles in the plasma edge; an extensive recalibration of the edge Thomson scattering system was completed as part of this process. This has revealed that I-mode pedestals are wider than those in H-mode, with widths up to 5% of the poloidal flux. This pedestal width does not follow any clear trend with $\beta_{P,ped}$, unlike in H-mode where a $\beta_{P,ped}^{1/2}$ scaling of the width was observed.
- These profiles have been used for edge stability analysis with the ELITE code. As anticipated from their ELM-free nature, these regimes are far from the MHD stability boundary, potentially allowing for further increases in performance.
- Gyrokinetic stability calculations have been performed using GYRO and GS2; excellent agreement has been found between the codes for the growth rates and real frequencies. Promising results include linearly unstable modes in the k_θ and frequency range of the observed WCM, propagating in the electron diamagnetic direction.
- Considerable progress has been made studying the relationship between pedestal turbulence and transport. There is a reduction in 60-150 kHz broadband turbulence following the L→I transition, accompanied by the formation of T_e and T_i pedestals; this is in contrast to the typical increase in turbulence in this frequency range following an increase in heating power in L-mode.

- The decrease in lower frequency turbulence is accompanied in I-mode by an increase in turbulence in the range 150<f [kHz]<300. These, Weakly Coherent Mode (WCM) fluctuations, have $\delta T_e/T_e$~2% (from ECE), but $\delta n_e/n_e$~10%, potentially consistent with the WCM driving more particle than energy transport.
- The WCM fluctuation amplitude has been found to be proportional to the particle flux in experiments where the plasma current was held fixed and the heating power varied. This provides strong evidence that the WCM provides critical contributions to the edge particle transport.
- Geodesic Acoustic Modes (GAMs) have been observed for the first time in Alcator C-Mod, in I-mode discharges; indeed, these fluctuations are present in all I-mode discharges analyzed to date that have GPI data available. These ~20 kHz GAMs interact and exchange energy with the WCM, and this fluctuating flow may be responsible for the broad frequency of the WCM.
- A reduction of core turbulence in I-mode has also been observed. The density fluctuation level $\delta n_e/n_e$ can decrease by 30%, and reductions in temperature fluctuations at the innermost point (ρ=0.74) have also been observed.

These C-Mod results are described in greater detail in Chapter 3.

3.0 Highlights from DIII-D Contributions

DIII-D contributions to the 2013 JRT came across a range of plasma configurations, targeting a range of physics goals. Specific regimes under consideration include:

- RMP studies: Resonant Magnetic Perturbations (RMP) are an important technique to control the H-mode edge transport and avoid type-I ELMs. In these experiments 3D fields of various types are applied to the plasma, creating 3D distortions, and potentially magnetic islands and magnetic stochasticity. These effects limit the width of the pedestal, thus avoiding the onset of type-I ELMs. This is a well established regime in DIII-D, and is now extended to ITER's I_p/aB_T.
- QH-mode: The Quiescent H-mode operating regime has H-mode like confinement, with pedestals in both the temperature and density, but with no large ELMs. Edge particle and impurity transport is provided by an Edge Harmonic Oscillation (EHO). This regime is also a well established in DIII-D, operating close to ITER-relevant torque and performance levels, and now extended to ITER-relevant Greenwald fractions.
- I-mode: The I-mode regime was described in section 2.0 of this chapter. A number of cases with temperature pedestals but no density barrier have been demonstrated in initial DIII-D experiments, although confinement is not yet as high as on C-Mod.
- VH-mode: The VH-mode is a very high confinement, ELM-free regime observed in DIII-D, with $H_{98(y,2)}$ up to 1.8. These regimes are associated with expanded pedestal widths and broader regions of flow shear, but with density accumulation rendering them non-stationary; arresting this density rise was a key goal of experiments in FY-13.

Given these various plasma regimes, experiments were conducted to both understand the transport physics and to test the physics limits of the operational regimes.

In the area of understanding the physics mechanisms that can provide the necessary particle transport in the absence of ELMs, the following key observations have been made:

- Experiments using fluorine as a tracer impurity were conducted to understand the impurity flushing in QH-mode. These experiments showed that the EHO in QH-mode can actually flush edge impurities more efficiently than type-I ELMs. Furthermore, the impurity confinement time does not increase as the toroidal rotation is reduced at constant density, despite the significant improvement in energy confinement.
- Experiments designed to explore and understand I-mode transport physics in DIII-D were executed. Numerous I-mode candidate examples were found in discharges with power ramps, distinguished by cases where the edge temperature increases by a fraction larger than the associated increase in the input power. These are not H-mode transitions, although the D_α recycling light indicates a complex evolution, as do related density fluctuations as measured by BES. These fluctuations are presently being analyzed and compared to type-III ELM regimes.

In the area of extending the operating space of these attractive regimes, the following key contributions are documented in this report:

- Experiments explored the achievable I-mode operating space by varying key parameters (I_P, q_{95}, δ_L, and κ). As noted above, a range of I-mode scenarios were identified. However, the observed confinement in these cases was less than in C-Mod, with $H_{98(y,2)}<0.75$ in all cases. Preliminary assessment shows that the expected pedestal evolution was cut short by sawtooth-triggered I->H transitions. This conclusion is reinforced by the observation that the lowest plasma currents had the higher electron temperature. These lower I_P cases had smaller sawtooth heat pulses, allowing the pedestal temperature to reach higher values before the H-mode transition. This effect is strong enough to overcome the degradation of the pedestal temperature with decreasing I_P, as observed in the C-Mod I-modes. As observed on Alcator C-Mod, the I-mode pedestal were found to be wider than H-mode pedestals, and wider than suggested by the EPED $\beta_P^{1/2}$ scaling.
- Experiments were conducted with the goal of extending QH-mode operation to high-normalized fusion performance. QH-mode performance corresponding to Q=10 in ITER was demonstrated for q_{95}=3.2, but only at high counter neutral beam torque. Reducing the counter torque results in locked mode formation. The toque threshold for locking was lower at higher q_{95}, and the NB torque can be reduced to zero at q_{95}=4.7 without locked mode onset.
- An additional set of experiments focused on increasing the density in QH-mode. As anticipated, no correlation with the Greenwald density limit was found, and Greenwald fractions of ~80% have been achieved with strong shaping. This is

consistent with ELITE calculations, which indicate that strong shaping expands the kink/peeling stability boundary to higher pressure and current.

- VH-mode experiments were conducted in order to i) attempt to extend the duration of the VH-mode phase via the application of 3D fields, and ii) make comparison to the NSTX Enhanced Pedestal H-mode regime (see Section 4.0 below). Several high-quality VH-mode examples were produced, and their equilibrium and fluctuation characteristics documented with the state of the art DIII-D diagnostic set. However, subsequent attempts to extend the duration with n=3 fields were unsuccessful, with the 3D fields apparently hastening the onset of ELMs in some cases. Density pump-out was not observed in the VH-mode phase, possibly due to the relatively high collisionality and q_{95} of these plasmas.
- An experiment was conducted to understand RMP ELM suppression with less than the full set of 3D field coils (I-coils in this case). These experiments showed that ELM suppression could be achieved with only very modest increases in coil current as the number of coils decreased. This is likely due to the n=1 & 2 sidebands produced when a coil is removed, which could help to increase the magnetic stochasticity in the edge plasma.

These DIII-D results are described in greater detail in Chapter 4.

4.0 Highlights from the NSTX-U Contributions

NSTX-U contributions to the 2013 JRT come in three distinct physics areas: the enhanced pedestal H-mode (EP H-mode), improved understanding of transport in the ELM-free pedestal, and better understanding of observed Edge Harmonic Oscillations.

The EP H-mode is a confinement regime showing a separation between the thermal and particle transport, in this case manifest as a significant reduction in thermal transport beyond the level achieved in H-mode. Key observations presented in this report include.

- An automated analysis program was used to identify a large number of additional EP H-mode examples. These include a newly observed, quiescent long-pulse case.
- A wider range of EP H-mode edge profiles shapes has been observed compared to previous examples, from cases with the steep gradient region located at the very edge of the plasma, to cases where it is shifted inward by ~10 cm.
- The correlation of the EP H-mode ion temperature gradient with the edge rotation shear has been confirmed for a much larger database of EP H-mode examples.
- A comprehensive analysis of edge fluctuations in EP H-mode has been conducted. However, no clear changes in the fluctuations have been observed.
- Prospects for triggering EP H-mode in NSTX-U have been addressed. A scheme to trigger EP H-modes via a single triggered ELM appears feasible.

NSTX has a high performance ELM-free regime with Lithium conditioning of the PFCs. While this regime does have some impurity accumulation, understanding those impurity and transport dynamics can be critical for devising mechanisms to eliminate those undesirable features. Key observations presented in this report include:

- The lack of ELMs, along with changes to the carbon transport due to modifications of the main-ion temperature and density profiles, explains the core carbon accumulation in discharge with lithium PFC conditioning, though anomalous carbon transport in the pedestal is required to explain the details of the profile shapes. The enhancement of neoclassical lithium diffusivities due to the high carbon concentration is partly responsible for the low lithium core concentration.
- Experimental analysis of pedestal turbulence amplitudes from beam emission spectroscopy show trends consistent with TEM/KBM turbulence drives; the trends are notably inconsistent with a ITG driven turbulence. These trends are consistent with linear microstability calculations made with the GENE code.

Regimes such as the QH-mode and I-mode have shown that the global particle inventory can be regulated by edge fluctuations that take the place of ELMs. NSTX has had similar edge fluctuations, though their amplitude appears to be too small to influence the global transport. Key observations presented in this report include:

- Measurements of the mode structure from Beam Emission Spectroscopy and reflectometry confirm that these modes are indeed located at the plasma edge, with maximum amplitude near the separatrix.
- The pedestal stability of an example discharge has been examined, and the operating point is near the peeling boundary, as in QH-mode in DIII-D.
- Studies of the potential to drive EHOs using the NSTX-U High Harmonic Fast Wave (HHFW) antenna show that it may be possible, especially at low q_{95}, though the driven amplitudes may be smaller than what could have been possible in NSTX.

These NSTX results are described in greater detail in Chapter 5.

5.0 Implications for ITER

RMP ELM control offers strong prospects for providing a stationary, ELM-free regime for ITER, and has been adopted as part of the baseline design. It has been adapted to ITER conditions (shape, I_P/aB_T, collisionality, beta), and demonstrated with various coil configurations. Indeed, experience around the world has shown a very wide range of different coil configurations have strongly beneficial effects to reduce the ELM size (if not always completely suppressing them). Work must continue to focus on physics mechanisms and extension to low torque, to provide fuller confidence of its applicability in ITER.

QH-mode provides prospects for an ELM free regime with high performance; when using the Neoclassical Toroidal Viscosity (NTV) effect, extension of this regime to low torque has been demonstrated. Further, the 3D fields used to generate the strong shear in the plasma edge that saturates the ELM precursor also appear to create increased core confinement. The regime has now also been extended to high Greenwald density fraction, and the role of the Edge Harmonic Oscillation (EHO) for expelling impurities was demonstrated. Nevertheless, confidence for ITER rests in gaining a predictive understanding of the EHO behavior onset, saturation and induced transport; demonstration of the regime on multiple devices would greatly assist this goal.

I-mode has the highly advantageous property of H-mode thermal confinement and L-mode particle confinement. It has been demonstrated in C-Mod to operate at the ITER q_{95} with high performance, and shows high confinement at ITER-relevant low collisionality and external torque. While there are no known physics barriers to extrapolate the I-mode regime to burning plasmas, projection of this regime to ITER requires an improved understanding of the physics governing the onset and saturation of the Weakly Coherent Mode (WCM), as well as the transport driven by these fluctuations. Refinement of techniques to avoid I→H transitions is needed. Continued multi-machine comparisons will be critical in making progress in this area.

VH-mode and EP H-mode both offer access to very broad pedestals and very high performance. However, their application to ITER remains more speculative. In particular, means of regulating the profile build-up must be developed, in order to arrest the density ramp and impurity accumulation. Furthermore, mechanisms of reliably triggering the EP H-mode configuration must be developed.

In conclusion, these various techniques offer increased optimism for the achievement and practical implementation of stationary ELM-free regimes in ITER, particularly with its flexible 3D coil set and other tools. Results in 2013 have made key further steps towards more ITER-relevant parameters, and addressed some key elements in the underlying physics. But in each case there is more to do, particularly to understand the physics of the mechanisms involved and to demonstrate robust control at the most ITER-relevant parameters.

Chapter 2: Comparison of the Regimes Studied as Part of the FY-13 JRT

1.0 Database Motivation and Definitions

As part of the JRT2013 research activity, a database has been constructed allowing comparisons between the various regimes discussed in this report. The motivation for this exercise was to i) assess progress relative to the goals of the JRT, ii) provide multi-machine context for the subsequent single facility reports, and iii) assist in guiding future experiments on DIII-D and NSTX-U, and potentially C-Mod. Brief descriptions of the various confinement regimes can be found in Chapter 1, with additional details in the facility report chapters.

This database includes equilibrium quantities from EFIT (or equivalent), such as the plasma current and toroidal field, parameters describing the plasma shape (R_0, a, κ, δ), and parameters describing the plasma energy content, such as the total stored energy and various measures of β. The database also contains a number of pedestal parameters, including most importantly the pedestal top T_e, n_e, and in some cases, T_i and Z_{eff}. Finally, a number of additional parameters, such as the line average density, auxiliary heating powers and global confinement multipliers are included. Note that edge turbulence/fluctuation data are not included in the database, as these data tend to be quite facility and even discharge specific.

For DIII-D, the regimes under consideration in the database include RMP H-mode, QH-mode, and I-mode examples. These DIII-D points appear as squares in the figures in this section. The pedestal parameters come from the standard post-shot fitting routines, not the specialized kinetic EFIT pedestal reconstructions utilized at other places in this report. Note that most of the I-mode points were collected as part of the JRT 2013 related experiments, and that additional data may be collected as part of the October 2013 DIII-D National Campaign.

The C-Mod data in these figures includes data from a large range of I-mode experiments. The pedestal parameters come from two different sets of analysis. One large data set uses the kinetic variable values taken at the 95% poloidal flux surface as representative of the pedestal top points; these ψ_N=0.95 values of density and temperature are scaled by 0.95 and 0.9, respectively. These scale factors come from a second smaller data set that additionally includes dedicated pedestal fits. The pedestal Z_{eff} is set to unity for these calculations.

The NSTX data comes from Enhanced Pedestal H-mode (EP H-mode) examples, and a limited number of cases where Edge Harmonic Oscillations (EHOs) have been observed. The pedestal fits utilized here are computed as a function of major radius, as the NSTX profile diagnostics are located on the device midplane. Note that, as described in Chapter 5, no NSTX regime has simultaneously achieved high confinement, complete elimination of large ELMs, and stationary conditions. The density is typically slowly rising in these discharges, and this should be borne in mind when inspecting the plots.

For more information on any of these topics, please see chapters 3-5, where the results from the individual machines are discussed in greater detail.

2.0 Comparisons Between Regimes Studied as Part of the 2013 JRT

2.1 Comparisons of 0D Quantities

The first set of comparisons made with this database involve the dimensional parameters from the various devices, and are shown in Fig. 2.1. The top frame shows the current and field utilized for the various regimes. The NSTX data clusters around a field of 0.4-0.5 T and plasma currents in the range 700<I_P [kA]<1300. The DIII-D data operate at currents up to 2000 kA, and fields up to 2.2 T.

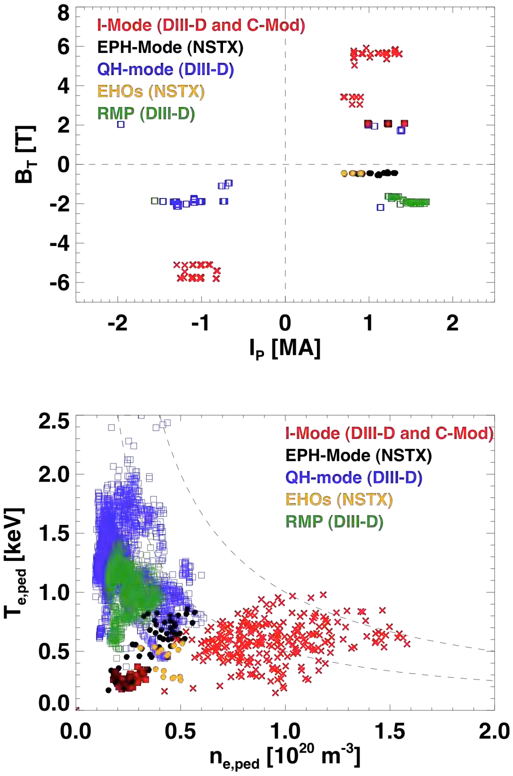

Fig. 2.1 Plots of (top) toroidal field vs. plasma current, and (bottom) the pedestal top temperature vs. the pedestal top density. NSTX data points are indicated as solid circles, DIII-D points by squares, and C-Mod points by the 'X' symbol.

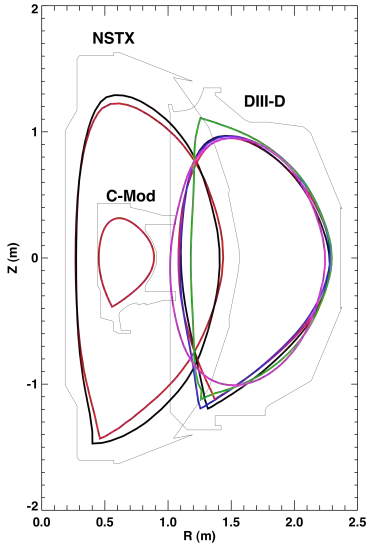

Fig. 2.2: Limiter and plasma boundaries for C-Mod, DIII-D, and NSTX. The plasma shapes shown are from discharges discussed in this report.

Finally, the high-field Alcator C-Mod device has contributed data at toroidal fields of up to 5.9 T. Note the variations in the sign of I_P or B_T, in order to i) change the ∇B drift direction relative to the direction of the dominant divertor, or ii) switch between dominant co-I_P or counter-I_P neutral beam injection.

The lower frame in Fig. 2.1 illustrates the absolute pedestal-top parameters for these discharges. As could be anticipated from the higher plasma current density, the C-Mod I-mode edge density is higher than the other devices, with values up to 1.5x10^{20} m^{-3}, and pedestal temperatures up to 1 keV. The DIII-D and NSTX pedestal densities are lower, and have comparable values of 1.5-6x10^{19} cm^{-3}. The DIII-D pedestals, however, have substantially higher temperature, with the best RMP cases approaching 1.5 keV and the hottest QH-mode cases exceeding $T_{e,ped}$ of 2 keV. The exception to this observation comes from the DIII-D I-mode cases, where pedestal top temperatures of 200-400 eV were common. As discussed in Section 4, the temperature pedestal evolution was often truncated by I→H mode transitions, often initiated by sawtooth heat pulses; the stated I-mode edge temperature and global confinement levels achieved to date may thus not represent the ultimate potential of the regime. Hyperbolas of the form $T_{e,ped}n_{e,ped}$=constant, corresponding to constant pedestal electron pressure, are also shown on the figure. These curves indicated that the high electron pedestal pressures occur in the hottest I-mode and QH-mode cases. The highest performance EP H-mode cases in Fig. 2.1 are also among the highest pedestal pressures observed in NSTX.

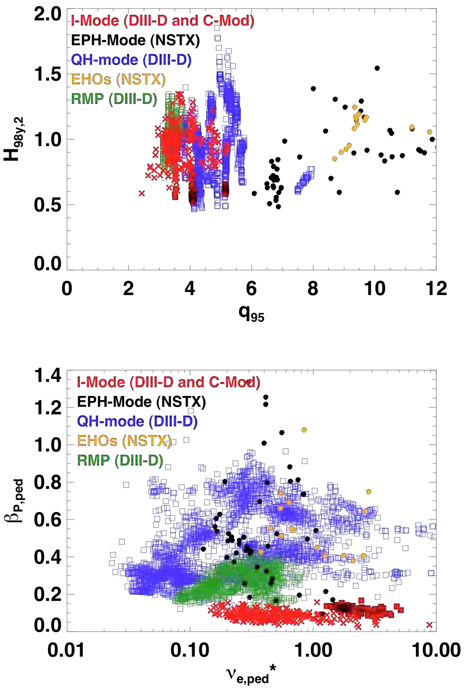

Fig 2.3: Plots from the multi-machine database showing dimensionless global and pedestal parameters for the different plasma regimes in DIII-D, NSTX and C-Mod.

A final dimensional comparison is provided in Fig. 2.2, where the plasma cross-sections are shown for representative discharges from this study. DIII-D and NSTX have similar plasma cross-sectional areas, but different aspect ratios. DIII-D and C-Mod have similar aspect ratios, but different major and minor radii. Hence, in terms of geometry, field and current values, and pedestal parameters, the machines in this report scan a wide range of parameters.

A number of dimensionless parameters for these regimes are shown in Fig. 2.3, starting with $H_{98(y,2)}$ plotted against q_{95} in the upper frame. All of these regimes can produce confinement factor in excess of $H_{98(y,2)}$=1.2 at relevant normalized β, with the highest multipliers in select EPH- and QH-mode examples. RMP and C-Mod I-mode cases have achieved $H_{98(y,2)}$~1 confinement level at q_{95} levels appropriate for ITER Q=10 operation. Additionally, some QH-mode data points, obscured in the figure, have achieved high-performance operation with q_{95}=3.2 and H~1, albeit with high levels of counter-NBI torque.

The bottom frame shows key dimensionless pedestal parameters, where the collisionality is calculated as. $\nu_{e,ped}* = 0.012 n_{e,ped,20} Z_{eff} q_{95} R / \varepsilon^{3/2} T^{2}_{e,ped,keV}$ This figure shows that all these regimes have been extended into the ITER relevant $\nu_{e,ped}*<1$ regime envisioned by the annual target language, with QH-mode achieved over the largest range of pedestal collisionality among the regimes under consideration in this analysis. The DIII-D I-mode examples achieved to date have a somewhat higher pedestal collisionality than the C-Mod points in this regime, and future DIII-D I-mode work may attempt to reduce the collisionality in this regime further. With regard to the poloidal β values, the highest values occur in the NSTX scenarios and the QH-examples. Interestingly, the poloidal β for I-mode is similar for DIII-D and C-Mod, despite the quite different operating points in terms of field and current. Again, the limit in β to date has been set by input power or I→H transitions; as noted in Chapters 3 and 4, these I-mode pedestals were well below stability limits. Dedicated studies of the I-mode pedestal width in both DIII-D and C-Mod show that the width does not scale with $\beta_{P,ped}^{1/2}$, as has commonly been observed in H-mode, and that the absolute width tends to be larger than in H-mode.

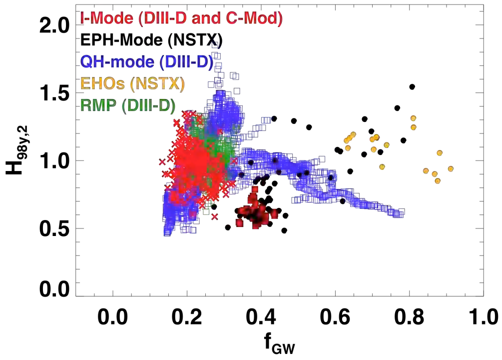

Fig 2.4:Plot of the confinement multiplier $H_{98(y,2)}$ vs. Greenwald Fraction, for the large database.

Finally, a recent focus of both I-mode and QH-mode studies has been to increase the density in these scenarios, towards the Greenwald fractions anticipated necessary for ITER [$f_{GW}=n_e/(I_P/\pi a^2)$, where the density is the line-average density in units of 10^{20} m^{-3}, the plasma current I_P is in MA, and the minor radius a is in meters]; progress towards achieving this goal is shown in Fig. 2.4. The achieved Greenwald fraction in these QH-mode regimes has now been increased to values of 0.8. These were achieved with gas puffing, and thus had a slow density ramp. However, all indications were that if the gas puffing were arrested, the density would have stabilized. The NSTX data also achieved good confinement at high density, including an EP H-mode case with H>1.5 with f_{GW}=0.8. The I-mode examples to date have been limited to lower Greenwald fractions, though still quite high values of absolute densities. However, experiments from C-Mod late in the FY12 campaign have had some success densifying the plasma after the L→I transition. Further increases appear possible, but have been precluded by lack of experimental time.

In summary, these plots and discussion show that:

- As envisioned in the target language, the three devices under consideration explore complementary portions of the achievable tokamak operating space.

- ITER relevant confinement and collisionality have been achieved in these various regimes.
- The prospects of achieving these regimes at the desired densities have been improved by recent experiments.
- The poloidal-β values of the DIII-D and C-Mod I-mode pedestals are similar, despite the vastly different absolute parameters. In any given machine, the I-mode pedestal has a larger width than of H-mode plasmas.

2.2 Comparisons of Key Physics Characteristics

Beyond these 0D comparisons, a number of common and divergent features have been noted when comparing the critical physics elements of these regimes.

Operating Points in Peeling-Ballooning Space: The macrostability of the edge plasma is generally considered to be constrained by current-driven low-n peeling modes and pressure driven intermediate-n ballooning modes. When these limits are crossed, an ELM is believed to occur. Studies described in this JRT report show that although the C-Mod Type-I ELMy H-mode cases are near the ballooning portion of this boundary, the I-mode cases tend to be far from any boundary; this provides justification for the statement above that there may be room to further increase the I-mode pedestal performance. The NSTX cases with EHOs, on the other hand, have been recently found to reside near the peeling boundary, as do the QH-mode examples. Mechanisms to potentially externally stimulate these presently weak EHOs in NSTX-U are discussed in Chapter 5.

Role of Edge Rotation and Rotation Shear: It is clear that the edge rotation plays a role in many of these regimes. The edge rotation-shear plays a key role in determining the onset condition for the EHO in the QH-mode plasmas; this rotation shear is believed to destabilize low-n peeling modes, which saturate as the EHO. There is some evidence that there are optimal values of the rotation shear in NSTX for achieving EHOs as well, though this result is more speculative. However, these recent studies have shown that the edge rotation shear plays a key role in providing the reduced transport in the NSTX EP H-mode. Finally, it appears likely that the edge rotation plays a role in the screening physics during RMP application. Hence, developing a self-consistent understanding of edge momentum generation and transport, including the interaction and damping of flows by internally and externally generated 3D fields, is critical for the extrapolation of these regimes.

Edge Fluctuations and Particle & Impurity Transport: Recent experiments have shown that edge fluctuations play a key role in flushing particles and impurities in stationary ELM free regimes. DIII-D results using fluorine as a traces gas have found that the EHO can flush impurities more efficiently than ELMs, while C-Mod results have shown that the edge particle flux is proportional to the amplitude of the WCM. These results increase confidence in the ability of these confinement regimes to support stationary operation in future devices.

External Torque Input: These studies have shown that the I-mode regime is accessible with both no external momentum input (ion cyclotron resonance heated plasmas in C-Mod), and with co-injected neutral beams (DIII-D), and that some pedestal parameters are similar with these two heating systems. Continued effort has been dedicated to generate low q_{95} QH-mode plasmas at ITER relevant torque, though locked mode formation remains problematic, and improved error field correction strategies will likely be implemented to mitigate this problem.

These physics element are discussed in greater detail in the following facility chapters.

Chapter 3

C-Mod Contributions to the FY2013 Joint Research Target

Amanda Hubbard[1], Dennis Whyte[1], John Canik[3], R. Michael Churchill[1], Istvan Cziegler[4], Arturo Dominguez[5], Martin Greenwald[1], Walter Guttenfelder[5], Nathan Howard[1], Jerry Hughes[1], Earl Marmar[1], Christian Theiler[1], Choongki Sung[1], Phil Snyder[2], John Walk[1], Anne White[1] and the Alcator C-Mod team

[1]Plasma Science and Fusion Center, Massachusetts Institute of Technology
[2]General Atomics
[3]Oak Ridge National Laboratory
[4]Center for Momentum Transport and Flow Organization, Univ. California San Diego,
[5]Princeton Plasma Physics Laboratory

1.0 Overview

This chapter of the FY2013 Joint Research Target report documents the contributions from the Alcator C-Mod team, including researchers at MIT and collaborators from other institutions. The Annual Target is:

> ***Annual Target***: *Conduct experiments and analysis on major fusion facilities, to evaluate stationary enhanced confinement regimes without large Edge Localized Modes (ELMs), and to improve understanding of the underlying physical mechanisms that allow acceptable edge particle transport while maintaining a strong thermal transport barrier. Mechanisms to be investigated can include intrinsic continuous edge plasma modes and externally applied 3D fields. Candidate regimes and techniques have been pioneered by each of the three major US facilities (C-Mod, D3D and NSTX). Coordinated experiments, measurements, and analysis will be carried out to assess and understand the operational space for the regimes. Exploiting the complementary parameters and tools of the devices, joint teams will aim to more closely approach key dimensionless parameters of ITER, and to identify correlations between edge fluctuations and transport. The role of rotation will be investigated. The research will strengthen the basis for extrapolation of stationary regimes which combine high energy confinement with good particle and impurity control, to ITER and other future fusion facilities for which avoidance of large ELMs is a critical issue.*

This report, and the research described in it, meet the requirements of the 4th Quarter Milestone, namely

> *Complete the required experiments and analysis. Prepare a joint report summarizing the contributions toward the development of high-performance stationary regimes devoid of large ELMs, and identifying important paths for future exploration.*

The target focusses on a crucial topic for fusion, since it is now clear that H-mode with Edge Localized Modes (ELMs), the standard high performance regime on most tokamaks, will have heat pulses which are unacceptable in ITER or a reactor. Active mitigation of ELMs, using magnetic perturbations or pellet injection, will be extremely challenging for ITER, and if it proves feasible will come at some penalty in confinement and fusion performance. Extrapolation of these techniques to a fusion reactor appears impractical, hence development of regimes with natural avoidance of ELMs is critical.

The Alcator C-Mod team has long been a leader in the development and study of quiescent, high performance, regimes. In fact, relatively few of its discharges have been in ELMy H-mode. The team pioneered the Enhanced D-alpha H-mode, in which increased particle transport and steady state are provided by an edge Quasicoherent Mode (QCM) [Greenwald 1999]. However, this regime is favored by relatively high collisionality and so may not extrapolate well to burning plasmas. Research in recent years has focused on the I-mode, also pioneered on Alcator C-Mod following early transient observations on both C-Mod and ASDEX Upgrade. This regime, described in the following section, combines several favorable characteristics: enhanced energy confinement with a strong thermal barrier near the last closed flux surface; little or no change in particle or impurity transport at the plasma edge, with L-mode like density profiles and global impurity confinement, hence no need for ELMs to regulate particle and impurity transport across the thermal barrier. Research for this milestone has focused on this regime, which as will be described appears to extrapolate well to the conditions of interest for fusion.

Since the Department of Energy did not fund operation of C-Mod in FY13, it has not been possible to do new experiments. However, analysis has been conducted of a large number of experiments conducted in FY12 and prior years. In particular, many discharges of the campaign in summer of 2012 were in the I-mode regime and had not been analysed at the start of FY13. Researchers from the Alcator C-Mod team also contributed strongly to the planning, execution and analysis of the DIII-D I-mode experiments described in Chapter 4.

This Chapter summarizes significant progress in the following areas:

- **Access conditions and operating space** (Section 2). A wide range of I-mode conditions have been achieved, closely approaching many key dimensionless and dimensional parameters of ITER.
- **Pedestal structure and stability** (Section 3). Detailed profile measurements and macrostability analysis explain the typical lack of ELMs in terms of distance from stability limits, and show key and favorable differences in pedestal width and height scaling from ELMy H-mode. Microstability analysis of the I-mode pedestal is beginning.
- **Turbulent fluctuations and role in transport** (Section 4). Density, temperature and velocity fluctuations have been analysed and new results shed light on the changes in, and separation of, particle and energy transport. Decreases in pedestal and core broadband turbulence correlate with reduced thermal transport in I-mode. A Weakly Coherent Mode usually observed in the pedestal region is linked to particle transport, and interacts with a newly identified

fluctuating zonal flow (Geodesic Acoustic Mode) which may play a key role in the regime and in transitions.

Finally Section 5 describes some of the many opportunities for further progress in this research which could be accomplished with continuing support of experiments on, and analysis of results from, Alcator C-Mod.

1.1: Description of the C-Mod I-mode regime and key prior results.

The key defining feature of the I-mode regime is the appearance of an edge *thermal* transport barrier, leading to pedestals in electron and ion temperature, without an accompanying *particle* transport barrier, hence L-mode like density pedestals and impurity transport. An example, presented at the 2010 IAEA Fusion Energy Conference [Whyte 2010], is shown in Figure 3.1-1.

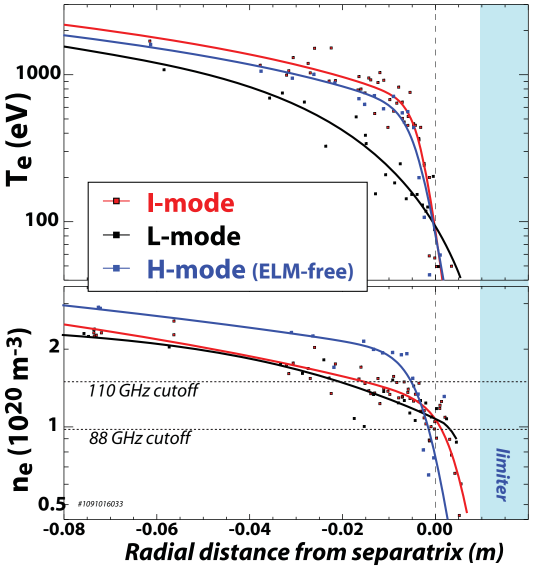

Figure 3.1-1: Examples of radial profiles from the outer third of the plasma for L-mode, I-mode and ELM-free H-mode phases of a C-Mod discharge (upper single-null, B_T = 5.6T, q_{95} ~ 3.2). Profiles are fitted to a modified tanh function. Slices are shown in (a) electron temperature from TS and ECE (b) electron density from TS. From [Whyte 2010]

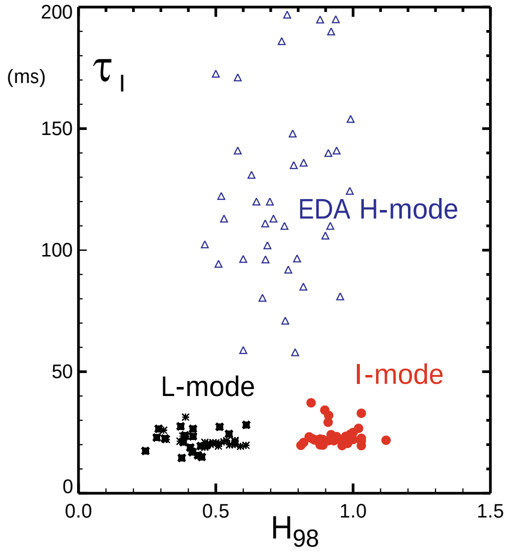

Figure 3.1-2: Measurements of particle confinement of injected Ca impurities vs. normalized energy confinement, for representative C-Mod L-mode, I-mode and EDA H-mode discharges. I-modes (red) have H-mode τ_E but L-mode τ_I.

These differences in edge particle and thermal transport are reflected in the global confinement properties. Figure 3.1-2 plots the impurity confinement time τ_I, measured using injection of Ca, and the energy confinement normalized by the

ITER98y2 scaling for H-modes [ITER 1999]. $H_{98,y2}$ reaches levels typical of H-modes, while τ_I remains at L-mode levels (20-30 ms) [Howard 2011]. Even the 'low particle confinement' EDA H-modes have τ_I up to 10 times higher, while standard "ELM-free" H-modes, such as the blue profile in Figure 3.1-1, have τ_I exceeding the pulse length of ~1 sec. ELM-free H-modes are thus intrinsically transient, with electron and impurity densities steadily rising and cooling the discharge; while confinement can be high they do not meet the requirements of stationarity which are the focus of this Joint Research Target. In contrast, I-mode has been developed by the C-Mod team into a highly robust, stationary, high performance regime.

An example discharge from the 2012 campaign is shown in Figure 3.1-3. The global energy confinement exceeds the ITER98y2 scaling. Errors bars on H_{98} represent the uncertainty in estimating fast particle contributions to the stored energy. There is no increase in density or radiated power after transition to I-mode. Safety factor q_{95} is 3.4; other examples have q_{95} below 3, spanning the planned range on ITER. Even at the maximum power available, nearly 5 MW of ICRH, there is no transition to H-mode; the I-mode phase continues until the heating is reduced.

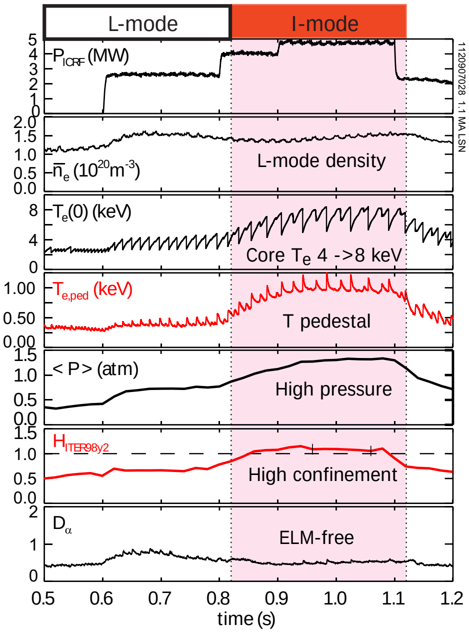

Figure 3.1-3: Time evolution of C-Mod discharge 1120907028 (5.8 T, 1.1 MA). I-mode is maintained up to the maximum ICRF power of 4.8 MW, with T_e (0) 8 keV, T_{ped} 1 keV and confinement at the H_{98y2} level.

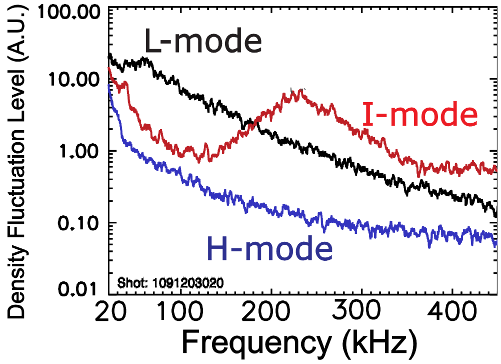

Figure 3.1-4: Reflectometer fluctuations (88 GHz, n_c= 9.6 x10^{19} m^{-3} ($r_c/a \cong 0.95$) for a typical q_{95}=3.1 C-Mod discharge 109120320 (1.3 MA, 5.8 T, upper single null). Spectra are averaged over 20 ms, in L-mode (black), I-mode (red) and H-mode (blue).

Historically, modest increases in edge temperature and confinement were observed, usually transiently, in discharges with ion **B**×∇B drift away from the active x-point, which is known to increase the H-mode power threshold [Greenwald 1997, Ryter 1998, Groebner 1998, Carlstrom 1998]. This phenomenon was termed 'improved L-mode' on ASDEX Upgrade [Ryter 1998]. It was shown on C-Mod that due to profile stiffness, global confinement also improved. As edge profile and fluctuation diagnostics improved, it was noted that changes in broadband fluctuation spectra accompanied the reduction in edge transport, with decreases at moderate f and increases at $f > 150$ kHz [Hubbard 2007].

From the 2009 operating campaigns, the regime was progressively extended to long duration and high confinement, and its potential for an attractive fusion regime was recognized. It was renamed "I-mode", since L-mode seemed a misnomer given the high confinement [McDermott 2009]. Improved fluctuation and profile diagnostics showed the typical presence of clear signatures – a decrease in broadband turbulence in the 50-150 kHz range when the T pedestal formed, along with a clear E_r well. At the same time a peak in fluctuations at typically 200-400 kHz is generally observed. This was named the 'Weakly Coherent Mode' (WCM) due to its broad spectrum, with $\Delta f/f \sim 0.3$-1. Representative spectra in each regime are shown in Figure 3.1-4. In the I-mode phase (red), mid-f turbulence decreases to levels near H-mode, while the peak of the 'weakly coherent mode' exceeds the L-mode level [Hubbard 2011].

The WCM has now been observed in electron temperature fluctuations as well as in density and magnetic turbulence (Figure 3.1-5) [White 2011]. The relative level of turbulent fluctuations is lower (1-1.6%) in T_e than in n_e (6-13%). All fluctuations are localized to the region of the T_e and T_i pedestal. Details of these fluctuations are presented in Section 4.2.

The I-mode regime is most often obtained in the unfavorable drift configuration, with ion **B**×∇B drift away from the active x-point. For C-Mod this can be achieved either by reversing the magnetic field and current for discharges with dominant x-points near the closed lower divertor, or in 'normal' field with an x-point near the open upper divertor. The power threshold for L-I transitions generally exceeds L-H scalings developed for favorable drift, and has somewhat different scaling [Hubbard 2012]. Access conditions are discussed further in the following section. Experiments in 2010 demonstrated that I-mode can be also robustly accessed in specific LSN shapes with *favorable* drift, and be extended to steady state ($> 10\ \tau_E$). In this case thresholds are near L-H scaling laws, and much lower [Hubbard 2011]. While normalized confinement remains at H-mode levels, the power range is small and absolute performance is thus modest. This report thus focusses on results obtained with the unfavorable drift configuration.

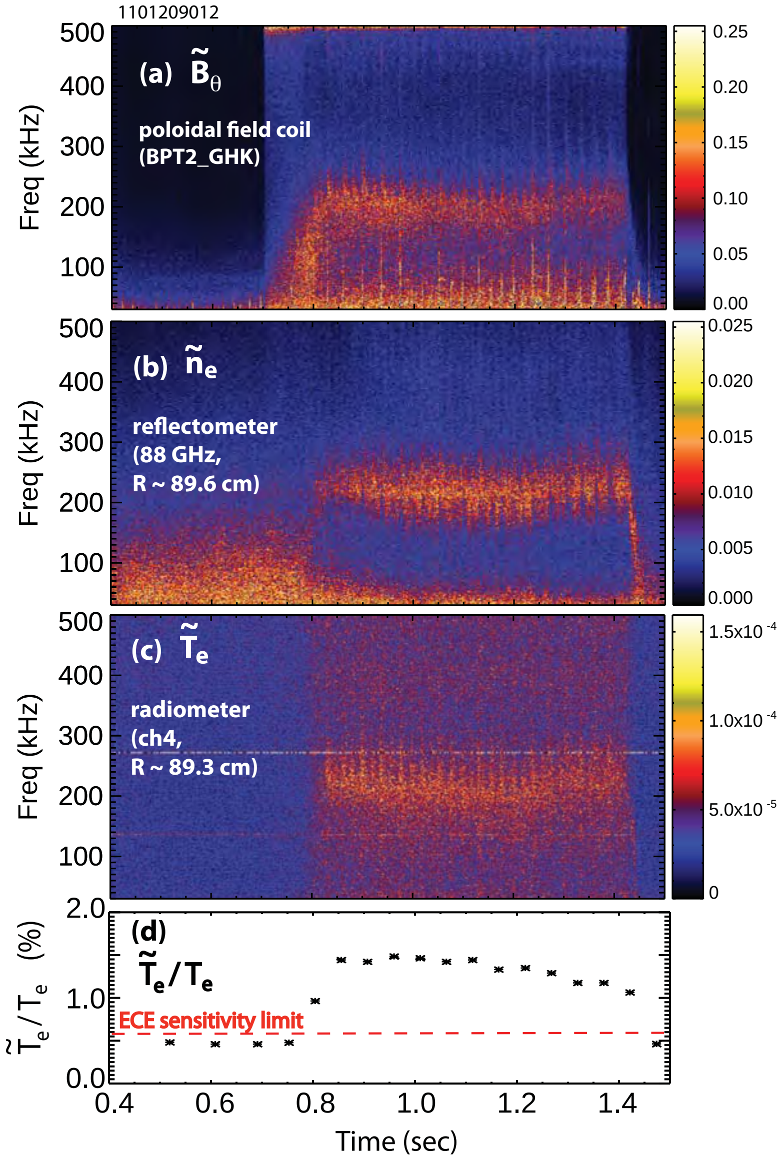

Figure 3.1-5: Contours of time-resolved spectra from edge fluctuations showing typical WCM features during I-mode (0.8 < t < 1.5). (a) Autopower spectrum of an edge poloidal magnetic field probe. (b) Autopower spectrum of an edge reflectometer signal ($f_{o\text{-}mode}$ = 88 GHz, R = 89.6 cm). (c) Autopower spectrum of edge ECE radiometer channel (f_{ece} = 241.8 GHz, R = 89.3 cm). (d) Temperature fluctuation level, $\delta T_e/T_e$ (%), in time, calculated from the radiometer channel. The sensitivity limit is shown as the red dashed line. From [White 2011]

2.0 Access and operating space of I-mode regime

2.1: Parameter space of C-Mod I-modes

The I-mode regime on C-Mod has proven remarkably robust, over extremely wide ranges of operating parameters, encouraging for its extrapolation to other devices. Over 260 discharges and time slices have been analysed and added to databases, with still more remaining to be added. These represent a wide range of plasma parameters, B_T=3.0-6.1 T, I_p=0.8-1.35 MA, q_{95}=2.5-5.3, loss power $P_{loss} \equiv P_{ohmic} + P_{RF,abs} - dW/dt$ =1.6-5.1 MW and average density $\bar{n}_e$=0.85-2.3x10^{20} m^{-3}. The field, q_{95} and density ranges span those of ITER and there is no apparent physics barrier to accessing the regime. Figure 3.2-1 shows the ranges of field and current in the scalar database, and in a newly created database of pedestal profiles, described in Section 3. In particular, I-modes extend to, and have highest performance in, low collisionality and q_{95}, both important for ITER. (Figure 3.2-2) This contrasts with the EDA H-mode which generally occurs at $\nu^* > 1$ and $q_{95} > 3.5$ [Greenwald 1997].

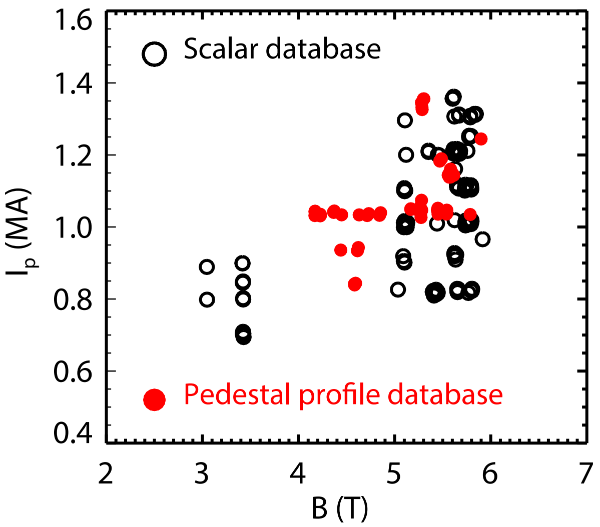

Figure 3.2-1: Ranges of plasma current and toroidal field in C-Mod I-modes covered by a database of scalar parameters (black), which has been extended during FY13 and a newly created database containing detailed pedestal fits (red).

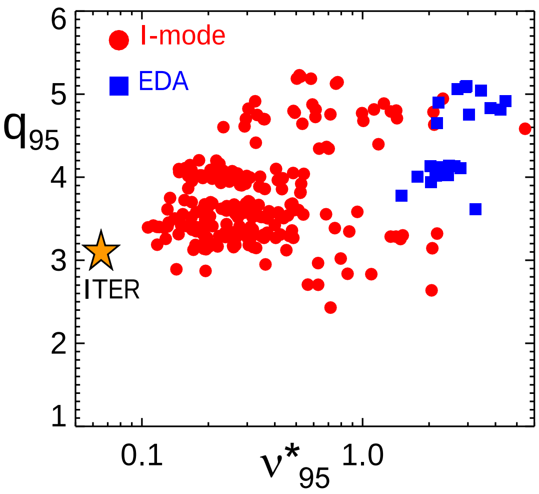

Figure 3.2-2: Range of safety factor q_{95} vs collisionality ν in C-Mod I-modes. A few representative discharges in the EDA H-mode regime are shown for comparison.*

Regions of configuration and parameter space have been identified in which I-mode is robustly accessed at moderate input power, and can be sustained at powers up to the maximum available (5 MW ICRF heating, a large power density for a device with 1.1 m^3 plasma volume). Stationary I-modes are now routinely sustained for the duration of the plasma discharge and heating power pulse, many energy and particle confinement times.

The optimal configuration to date uses reversed field and current, with upward ion B×∇B drift and the X-point towards the closed lower divertor, and moderate L-mode target densities, typically in the range $\bar{n}_e$=1.0-1.5x10^{20}m^{-3}. An example was shown in Figure 3.1-3.

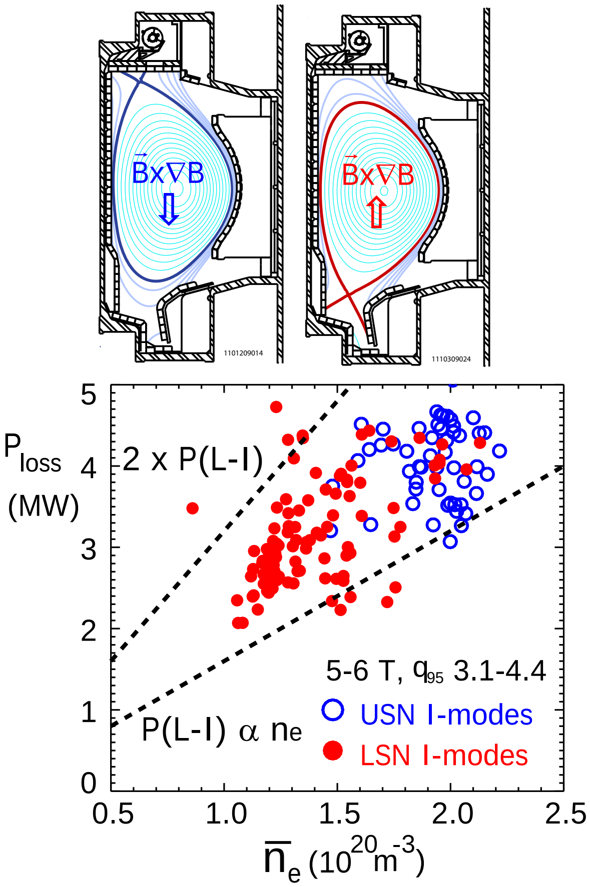

*Figure 3.2-3: Loss power vs. $\bar{n}_e$ for a subset of I-mode discharges with B_T 5-6 T and q_{95}=3.1-4.4, comparing two configurations with unfavorable ion **B**× ∇B drift. The LSN, reversed B_T configuration (closed red points) has a wider density and power range.*

Figure 3.2-3 compares the operating space achieved to date for a restricted current and field range, in the upper null, forward field (blue) and lower null, reversed field (red) configurations. The LSN I-modes extend to lower density, and have a wide power range at these reduced densities, robustly maintained with at least twice the power required to access the regime, and up to the maximum heating power available (5 MW ICRF). Higher powers are likely possible; transitions to H-mode are rare in these conditions. The reason for the difference between LSN and USN I-modes is not clear, but may be related to slight differences in shape, or to the interactions of the separatrix and SOL with the closed lower divertor. Due to high SOL power densities, a limited range of shapes is possible in each configuration. Impurity seeding, usually with Neon, is used in some cases to reduce heat fluxes, and due to the low impurity confinement characteristic of I-mode is found to be compatible with high performance.

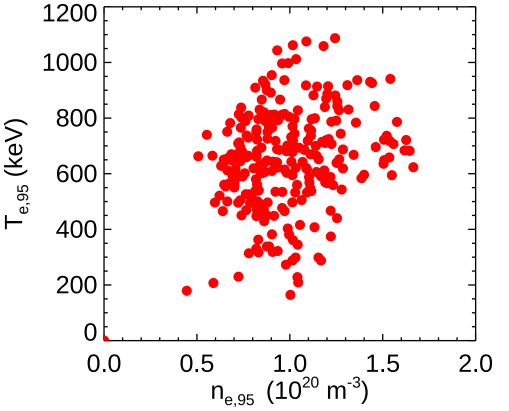

Figure 3.2-4: Temperature vs. n_e at ψ=0.95 for all C-Mod I-modes in the scalar database.

The C-Mod I-mode dataset also covers a very wide range of edge parameters. Density and electron temperature at the 95% flux surface are shown in Figure 3.2-4.

2.2: Thresholds and power range

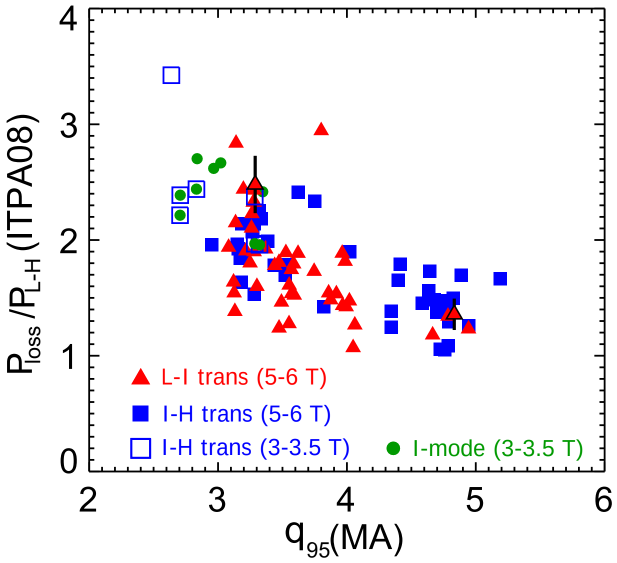

Figure 3.2-5: Threshold power for L-I transitions (red triangles) and I-H transitions (blue squares) in unfavorable drift, normalized to the ITPA08 scaling for L-H transitions with favorable drift. I-mode thresholds are higher and have a q_{95} dependence not present in the L-H scaling.

There has been extensive study of the conditions for accessing I-mode on C-Mod, and for remaining in the regime before I-H transitions. Scalings for the L-I transition were developed in 2012 and have since been extended with more experiments. Comparison of power thresholds with the ITPA scaling $P_{Thres,ITPA08} = 0.0488\ n_{e20}^{0.717}\ B_T^{0.80}\ S^{0.941}$ [Martin 2008] for L-H transitions in favorable drift is shown in Figure 3.2-5. The L-I threshold is 1-3 times higher, and has a q_{95} dependence not in the L-H scaling. The 2012 regression analysis of the data set of L-I transitions was restricted to discharges with B_T= 5-6 T which had widest variation of current and density. The best fit was $P_{thresh}=2.11\ I_p^{0.94 \pm 0.24}\ \bar{n}_e^{\ 0.65 \pm 0.18}$, confirming a strong current dependence as suggested by the normalized scaling above [Hubbard 2012].

Attempts to scale the I-H threshold have been less successful; there is a great deal of scatter even for fairly comparable conditions, in both power and local parameters. As noted above, the widest power range, at least a factor of two, is found in LSN, reversed B_T discharges with relatively low density. The density range in this configuration was extended to both higher and lower density in 2012 experiments. Fig 3.2-6 shows results from a dedicated experiment carried out in August and September 2012, with fixed LSN shape, field and current (5.8 T, 1.1 MA, q_{95}=3.5). These show for the first time the existence of a minimum in the P_{L-I} vs n_e dependence; power thresholds (green triangles) increase roughly linearly above about 1.3 x 10^{20} m^{-3}, but also increase at lower density. The lowest density for which I-mode was achieved was 0.89 x 10^{20} m^{-3}.

The upper limit of density for given parameters and configuration has in the past been set by the range for which L-I transitions occurred; above a certain density (1.8 x 10^{20} m^{-3} in the conditions of Figure 3.2-6), transitions directly from L to H-mode occur. In general the power range between L-I and I-H thresholds (blue squares) becomes narrow at higher density. This has been a potential concern for extrapolation to burning plasmas; while lower density is advantageous for accessing I-mode with moderate power, higher densities are optimal for fusion performance. It is thus desirable to increase density during the I-mode phase.

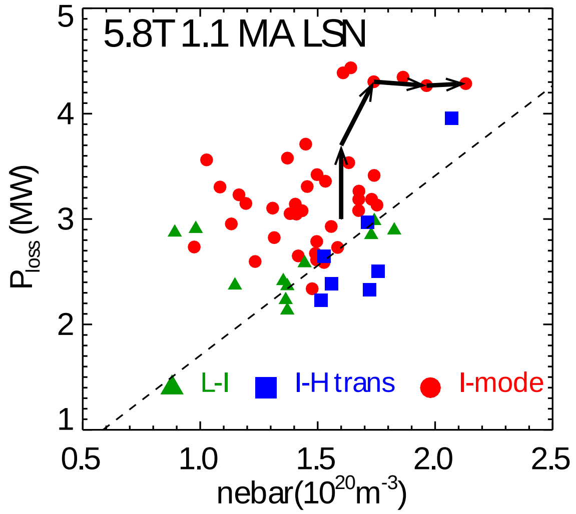

Figure 3.2-6: Loss power vs. line averaged density for an experiment with fixed conditions. This shows a minimum in the power threshold for L-I transitions (green triangles, and an upper limit to the density at which transitions to I-mode occurred. However, higher density could be achieved by fuelling into I-modes; the arrows show the time trajectory of the discharge in Fig. 3.2-7.

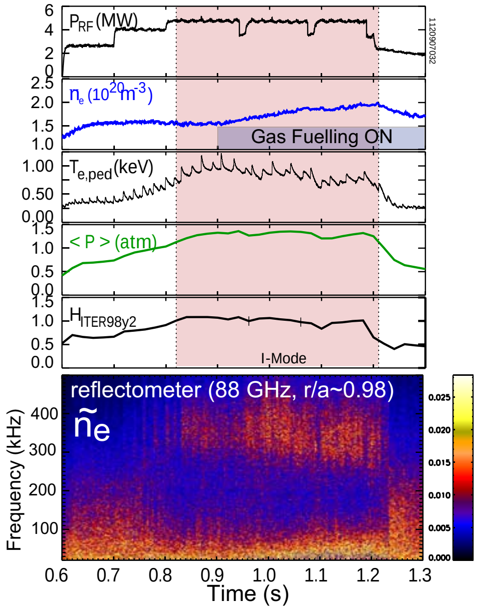

Figure 3.2-7: Time traces and edge density fluctuations for a discharge similar to that shown in Fig. 3.1-3 but with gas fuelling during I-mode. Density is increased 30% while maintaining core pressure and confinement.

Initial C-Mod experiments are quite encouraging in this regard. Gas fuelling was added to an I-mode phase similar to that of Figure 3.1-3, increasing $\bar{n}_e$ from 1.5 to 2 x $10^{20}$$m^{-3}$ (Fig. 3.2-7). Stored energy remained nearly constant, with $H_{98y2} \geq 1$, and I-mode turbulence features and transport barrier are clearly maintained. The trajectory of this discharge is shown on Fig. 3.2-6, and shows that I-mode is maintained for powers well above that which resulted in I-H transitions when starting from higher target density. In a subsequent discharge, an I-H transition resulted from a *decrease* in heating power at comparable density (top right blue square). This suggests that maintaining an edge T_e gradient is important in driving the higher frequency turbulence which appears to drive particle transport, and to avoid H-mode transitions. Thus, with further increases in power, from external sources or from alphas in a burning plasma, it could well be possible to extend the I-mode operating space to even higher densities and performance. In short, the limits of I-mode operating space on C-Mod have by no means been reached, and further experiments are highly desirable to assess the ultimate potential of the regime.

2.3: Global confinement and performance

Importantly, good global confinement is maintained across the wide parameter space of I-modes. Figure 3.2-8 shows H_{ITER89} vs q_{95}; levels exceeding the H-mode scaling which is the basis for ITER performance projections are achieved down to q_{95} below 3, the ITER H-mode operating point. H_{ITER89} ranges from 0.7 to 1.2. Stored energy is calculated from magnetics, so that there may be some contribution from fast particles in the highest temperature cases. A key and very positive difference between I-mode and H-mode confinement scaling is the much weaker, perhaps no, degradation with input power. The stored energy increases close to linearly with power, as shown in Figure 3.2-9. In contrast, the H-mode confinement scaling $\tau_{ITER\text{-}H98,Y2}$ decreases strongly with power, as $P^{-0.69}$. This means that for given global parameters, the normalized confinement generally increases with input power. The very favorable I-mode scaling likely reflects the fact that the boundary is away from stability limits. The height of the temperature and pressure barrier also scales approximately linearly with increasing heating power, unlike H-modes where it tends to saturate. Detailed measurements and analysis of the critical pedestal region are presented in the following section.

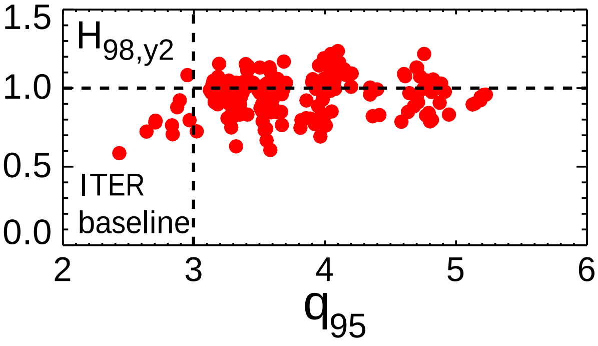

Figure 3.2-8: Normalized confinement $H_{98,y2}$ vs q_{95} in I-modes. The C-Mod discharges meet the requirements of the ITER baseline scenario in both parameters.

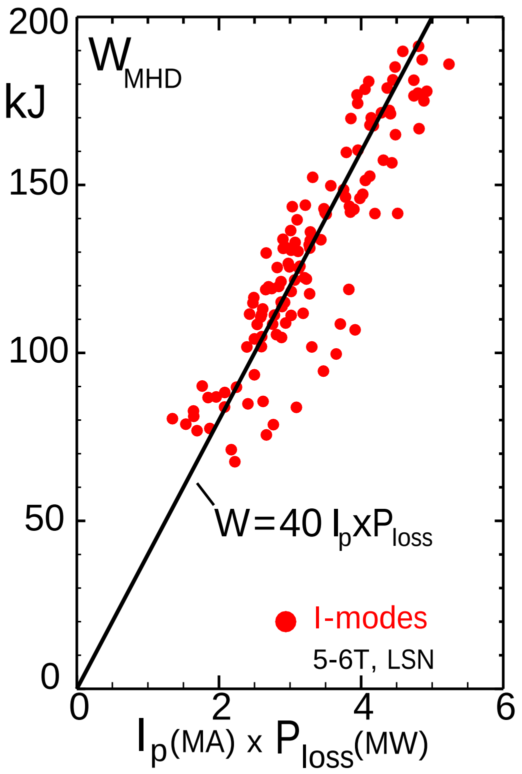

Fig 3.2-9: Stored energy vs I_p P_{loss} in lower single null I-modes. In contrast to H-modes, W scales linearly with power.

3.0 Pedestal and stability analysis

3.1: Pedestal structure

The structure and stability of the pedestal region in I-mode is key to understanding both its favorable transport properties and its general lack of large ELMs. A major emphasis of efforts in 2013 has been to analyse profiles in this region, from the extensive set of FY2012 experiments, using upgraded diagnostics and analysis techniques. These use data from a suite of high resolution diagnostics, including Edge Thomson Scattering (ETS) for n_e and T_e, and CXRS on both the high and low field side for ion profiles and flows, from which E_r profiles are being derived [Churchill 2013a]. An extensive recalibration of the ETS diagnostic was performed during the C-Mod shutdown. This has resulted in more accurate profiles, and revealed that T_e pedestals can be even higher than was previously thought. T_e profiles can be substantially modified by sawtooth heat pulses, necessitating carefully synchronized averaging. An example of electron profiles from the stationary high performance I-mode discharge of Figure 3.1-3 is shown in Figure 3.3-1.

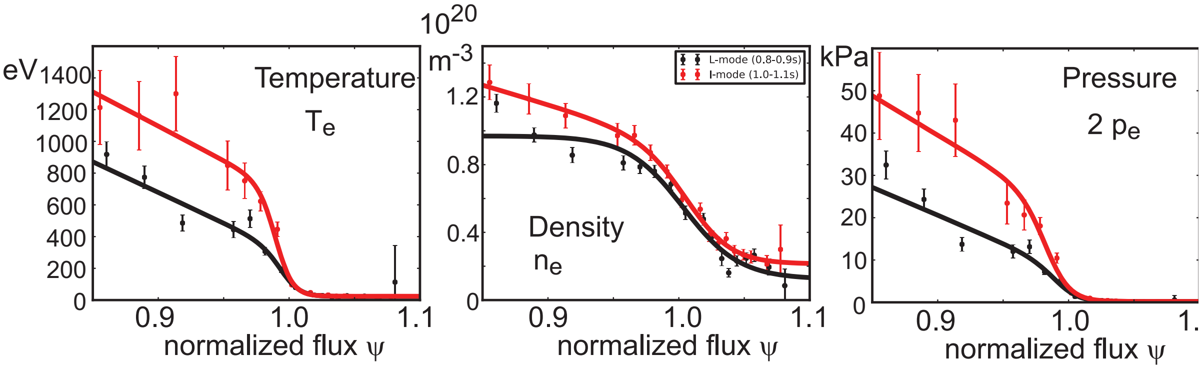

Figure 3.3-1: Electron pedestal profiles from an I-mode (red) vs L-mode (black) phase of a C-Mod discharge. The temperature exhibits a strong pedestal in I-mode, while the density structure is nearly identical to L-mode. The pedestal pressure and gradient are also higher in I-mode.

A new data set of global parameters and tanh fit parameters from such carefully analysed profiles has been created. It currently contains 72 time slices from a wide range of plasma parameters including dedicated scans in FY2012 (0.84-1.35MA current scan, 4.34-6.1T field scan, 1.0-1.9 scan in average density (equivalent to a Greenwald fraction scan of 0.13-0.25). Preliminary results from a smaller dataset were presented at the 2013 TTF meeting and included in the second quarter JRT report. The fitted profiles allow pedestals in I-mode to be compared with those previously studied, and simulated with models, in ELMy and EDA H-modes [Walk 2012, Hughes 2013].

The ELMy H-mode studies have shown that the pressure pedestal is well predicted by the EPED model [Synder 2009], in which the pressure limit is set by a combination of peeling-ballooning modes and kinetic ballooning modes. The pedestal width scales with the square root of pedestal poloidal beta β_{pol}, as shown in Figure 3.3-2. This is consistent with results from several other tokamaks. Together, this validation has resulted in a prediction for ITER [Groebner 2013, Hughes 2013]. In contrast, pedestals in I-mode are significantly wider than H-modes of comparable β_{pol}, up to 5% in normalized flux. As shown in the same figure, they do not show any scaling trend with β_{pol}. This is consistent with gradients being below kinetic ballooning limits, suggesting that a different physical mechanism regulates the pedestal. The broader pedestal gives the potential to further increase pedestal heights without violating MHD limits. Stability analysis is presented in the following section.

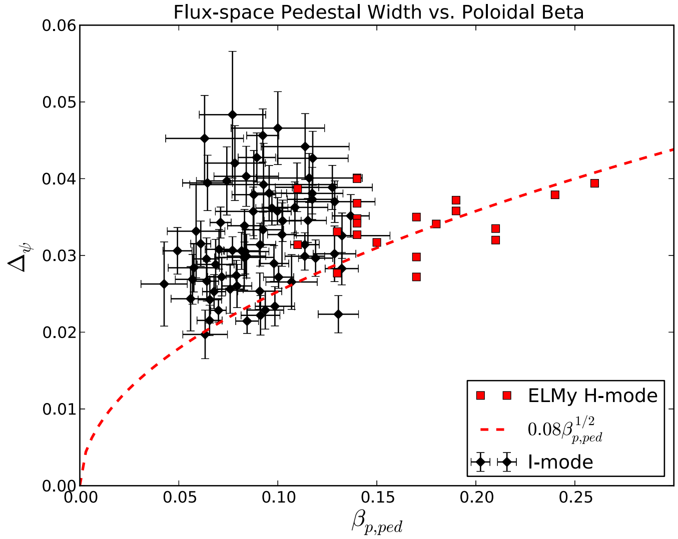

Figure 3.3-2: Measurements of pressure pedestal widths vs poloidal beta. ELMy H-modes follow the scaling predicted by the EPED model [ref], while I-mode pedestals are typically wider for comparable β_P.

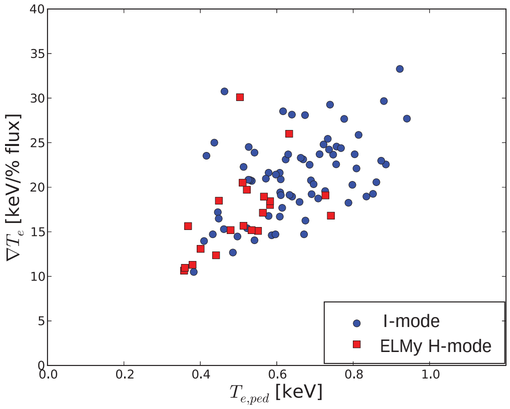

Figure 3.3-3: Electron temperature gradient vs pedestal height, for sets of I-modes (blue circles) and ELMy H-modes (red).

Analysis of trends in I-mode pedestal height, width and gradients is in progress. An example is shown in Figure 3.3-3, which compares the height and gradient of T_e pedestals with those in ELMy H-mode. While there is considerable overlap, the I-mode plasmas extend to hotter and steeper pedestals. This work will be presented by MIT graduate student John Walk in an invited talk at the APS-DPP meeting in November, 2013.

Charge Exchange Recombination Spectroscopy (CXRS) diagnostics, viewing both the high and low field side of C-Mod, are used to measure for ion profiles and flows. An ion temperature pedestal develops which is, within experimental uncertainties, equal to that in T_e. Toroidal rotation in the co-current direction also increases. This is correlated to temperature gradient; comparing rotation in I-mode and H-mode has been important in understanding the source of this intrinsic rotation [Rice 2011]. From these, E_r profiles are being derived. Steep E_r wells are observed in I-mode, in the region of the temperature pedestal, as shown in Figure 3.3-4. Both the diamagnetic and the poloidal flow term in the radial impurity force balance equation contribute significantly to E_r. Strong gradients in the poloidal flow, just inside the LCFS, make the E_r well asymmetric with a strong shear layer on its outer side. Besides an approximately 20% wider E_r well, this asymmetric structure is the main difference compared to E_r of EDA H-modes. Careful in-vessel calibrations have been performed to spatially align CXRS measurements with fluctuation measurements from GPI such that the location of the Weakly Coherent Mode inside the E_r well can be determined and the effect of the E_r shear on the WCM be investigated. Efforts to achieve this are still ongoing and possibly require a deconvolution of the measured profiles from instrumental effects. This has so far only been performed for the CXRS system. Measurements of boron density show an in-out asymmetry in the H-mode regime, but not in either I-mode or L-mode [Churchill 2013b]. This is again consistent with L-mode-like particle transport in the I-mode regime.

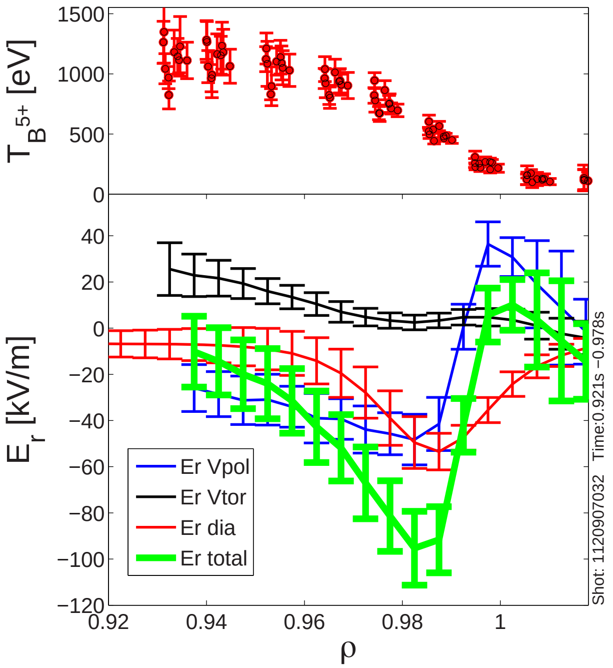

Figure 3.3-4: Profiles of boron temperature (top) and E_r components in a high power I-mode discharge, from CXRS.

3.2: Pedestal stability

The accurate pedestal profiles now available, in high performance I-modes, have enabled analysis of the MHD stability in the plasma region. This is important in understanding the avoidance of ELMs, one of the most important features of the regime, and in assessing the potential for further increases in pedestal pressure and global performance.

The theory of peeling-ballooning modes has been highly successful at explaining the onset conditions for Type I ELMs on a number of tokamaks, particularly through its model implementation in the ELITE code [Wilson 2002]. ELITE was used previously to test the peeling-ballooning stability of several EDA H-mode discharges, some of which exhibited small, irregular ELMs in addition to the usual QCM [Mossessian 2003]. In these cases, calculated stability to peeling-ballooning modes was indeed correlated with the absence of ELMs. More recent calculations take advantage of a technique to perturb the pressure gradient and current profile about the experimental reconstruction, and evaluate stability on a grid of $(p', j_{||})$. This technique yields contours of $\gamma_{max}/\omega_{eff}$, the maximum linear growth rate normalized to a stabilization rate. Here, $\gamma_{max}/(\omega_{eff}/2)<1$ is the criterion for stability where ω_{eff} is derived from earlier calculations done with the BOUT++ code [Dudson 2009], which gave a quantitative description of diamagnetic stabilization of ideal peeling-ballooning modes at moderate to high n-number [Snyder 2012].

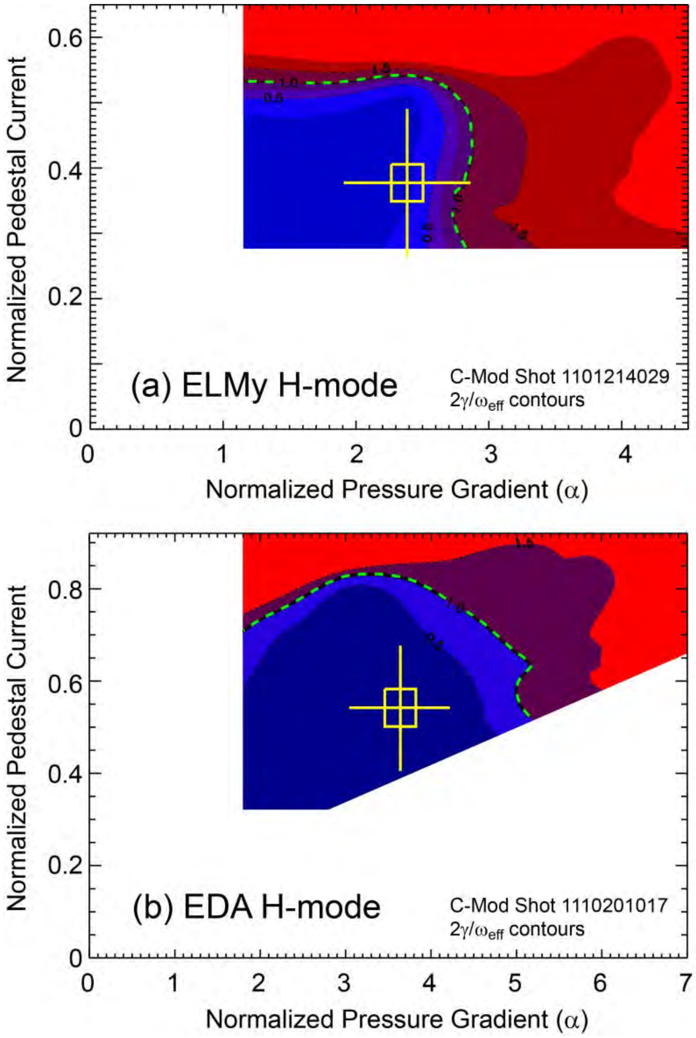

Figure 3.3-5: Peeling-ballooning stability calculated with ELITE in (a) ELMy H-mode and (b) EDA H-mode, with experimental points marked by cross-hairs [Hughes 2013].

Discharges with ELMy H-modes in C-Mod, analysed using the ELITE code, do indeed lie near the predicted stability boundary, consistent with the peeling-ballooning model. An example is shown in Figure 3.3-5(a) [Hughes 2013]. Within experimental uncertainties, the pedestal is at the calculated stability boundary, with the most unstable modes occurring at moderate n, and near the pressure-limited side of the stability contour.

Pedestals in the quiescent EDA H-mode regime, which in common with I-mode do not exhibit large ELMs, tend to exist farther in phase space from the contour of instability. This is illustrated in Fig. 3.3-5(b).

In comparison to ELMy H-modes, I-modes generally have comparable or higher temperature pedestals but much weaker density gradients, as illustrated in Figure 3.3-6 (a,b). Also, as noted above the pedestals tend to be wider. There is thus substantial reduction in pressure gradient and bootstrap current drive, relative to H-mode, making I-modes quite stable to peeling-ballooning modes. These profile differences are also evident in Figure 3.3-6(c,d).

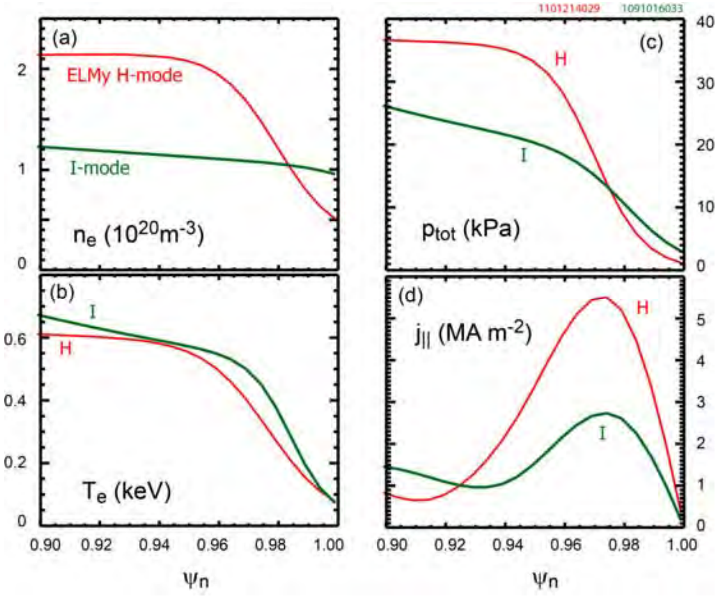

Figure 3.3-6: Model profiles, fitted from experimental data, used as inputs to MHD stability analysis of ELMy H-mode (red) and I-mode (green). Shown are (a—b) electron density and temperature, (c) total pressure, and (d) low-field side current density, all as a function of normalized poloidal flux [Hughes 2013].

For the I-mode shown, ELITE calculations find growth rates an order of magnitude or more below the instability criterion. Because I-modes of modest performance, such as this example, operate so far from the stability boundary, this boundary can be challenging to find with the perturbative technique outlined above. However, indications are that the boundary is very similar to that in an H-mode of similar pedestal pressure and thermal stored energy. As seen in Fig. 3.3-7, substantial increases in pedestal p′ are possible within the constraints of the peeling-ballooning limit, allowing for considerable increases in performance while still remaining ELM-suppressed.

Recently, stability analysis was performed for a higher performance I-mode discharge 1120913026. In this case the peeling-ballooning boundary was reliably determined. Preliminary results, shown in Figure 3.3-8, indicate that the experimental conditions were again well away from this boundary, consistent with the lack of ELMs and indicating that further increases in the pedestal are possible. The solid line shows stability contours for infinite-n ballooning MHD modes calculated by BALOO [Connor 1979], which are used as an indication of the KBM threshold. They indicate that the pedestal is also stable to KBMs, consistent with the width scaling in Figure 3.3-2. This MHD stability analysis has been carried out as part of the thesis work of an MIT graduate student, in collaboration with Phil Synder of General Atomics.

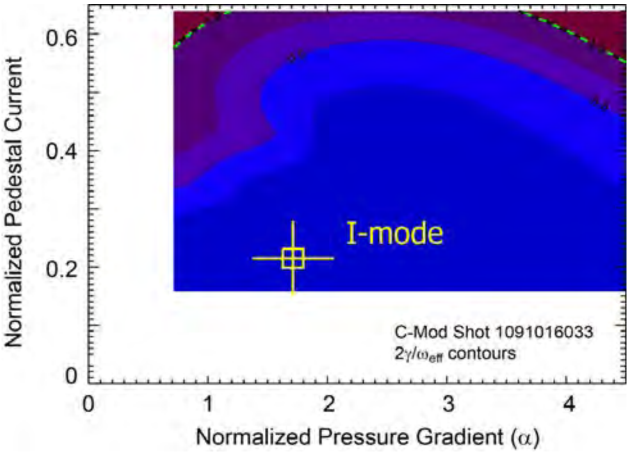

*Figure 3.3-7: I-mode operating point (cross-hairs), and approximate boundary for peeling-ballooning stability (dashed curve)***,** *for the moderate performance discharge whose profiles are shown in Figure 3.3-6.*

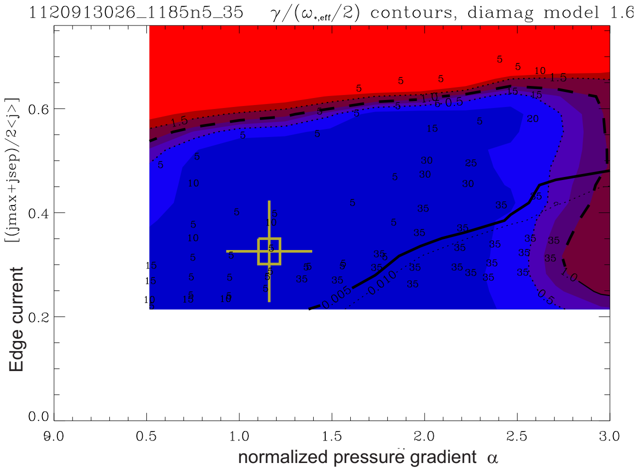

*Figure 3.3-8: I-mode operating point (cross-hairs), and approximate boundary for peeling-ballooning stability (dashed curve)***,** *for a higher performance I-mode discharge with I_p 1 MA, B_T 4.8 T, 3 MW ICRH, which reached central T_e 6 keV.*

Given the macrostability of the I-mode pedestal, and lack of ELMs, other mechanisms, as yet uncertain, appear to be regulating the transport and maintaining steady conditions. Microstability analysis has begun in FY13 to identify the potential sources of observed fluctuations, which are discussed in the following section. Linear gyrokinetic calculations using GS2 and GYRO (J. Canik [ORNL], W. Guttenfelder [PPPL]) have been performed for both the H-mode and I-mode cases, beginning just inside the steep gradient region (e.g. at ψ_N~0.94) and steadily progressing outward (e.g. toward ψ_N =0.98). Very good agreement in both real and imaginary parts of growth rates has been obtained in the code-to-code comparisons, shown in Figure 3.3-9, with agreement becoming somewhat poorer as collisions are implemented in the calculations. Promising signatures exist in the code results which might have a link to the WCM that is experimentally observed in I-mode.

Specifically, in the range of k_θ that is associated with the WCM fluctuation, linear unstable modes are found with real frequencies of tens of kHz, and propagating in the electron diamagnetic direction. Future plans for this analysis, using the high performance I-mode data sets with improved edge Thomson and CXRS data shown above are to: (a) push calculations farther into the steep gradient region, (b) establish sensitivity of results to highly variable experimental quantities such as the gradient scale length of the temperature pedestal, and (c) examine the ratio of quasi-linear heat and particle fluxes and compare with H-mode.

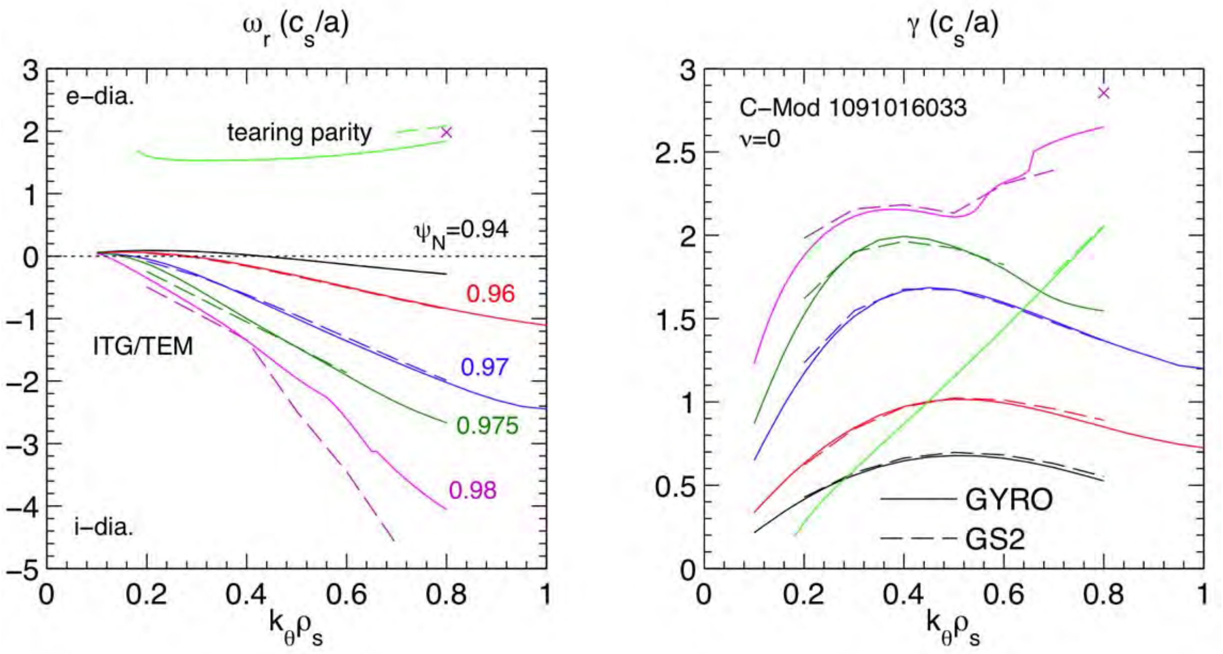

Figure 3.3-9: Initial linear gyrokinetic simulations of the pedestal in a C-Mod I-mode discharge, for various normalized radii. Collisionless simulations with GS2 (dashed curves) and GYRO (solid) agree very well.

4.0 Turbulent fluctuations and their role in transport

4.1: Pedestal broadband turbulence and its role in energy transport

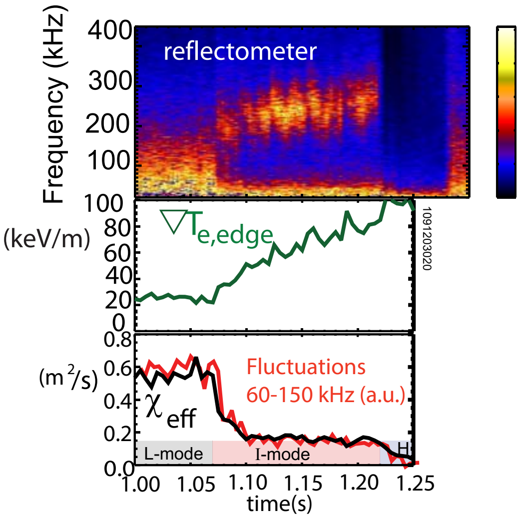

Figure 3.4-1: Reflectometer fluctuations at n_c= 9.6x$10^{19}$$m^{-3}$ ($r_c/a \cong 0.95$) and edge thermal transport in L, I and H-mode for a q_{95}=3.1 C-Mod discharge 109120320 (1.3 MA, 5.8 T, upper single null). The decrease in fluctuations integrated over the 60-150 kHz frequency band (red trace) correlates with the computed χ_{eff}, decreasing from L-mode to I-mode, and further in an ELM-free H-mode.

Considerable progress has been made in characterizing the edge and SOL turbulence, transport and profiles, and the relationships between them. A key signature of the L-I transition, accompanying the formation of T_e and T_i pedestals, is the reduction of edge broadband turbulence in intermediate frequencies, typically ~60-150 kHz. This contrasts with the usual increase in such turbulence with increased heating in L-mode. The reduction is seen most clearly in density, on reflectometry channels located in the outer 5-10% of the plasma, and is also visible in magnetic fluctuations. A good correlation in time has been observed between the level of density fluctuations and the reduced thermal conductivity χ_{eff} inferred from power balance analysis in the outer 5% of the plasma, as shown in Figure 3.4-1 [Hubbard 2011]. This suggests that turbulence in this frequency range is an important contributor to thermal transport. The reduction may be related to the development of an E_r well in I-mode, which as shown in Section 3.1 is clearly evident from CXRS diagnostics though weaker than in H-modes [McDermott 2009]. It has been observed, to varying degrees, in all I-mode phases on C-Mod.

4.2: Weakly coherent mode and its role in particle transport

Simultaneous with the formation of an edge temperature pedestal at the L-I transition, edge turbulence typically increases at frequencies > 150 kHz. This 'weakly coherent mode' (WCM) is evident at 240 kHz in the example of Figure 3.4-1. It is also detected in magnetic fluctuations measured on poloidal field pickup coils mounted outboard of the plasma on the low field side, and on Electron Cyclotron Emission (ECE) fluctuations [White 2011].

The WCM density fluctuations are also observed by Gas Puff Imaging (GPI) [Cziegler 2010]. The reflectometer, ECE and GPI measurements all show that the WCM is localized to the region of the strong edge temperature gradient. GPI measurements resolve the poloidal wavenumber, giving $k_\perp\rho_S$~0.1, $n_{toroidal}$~20 and show that the mode propagates in the electron diamagnetic direction in the plasma frame. An example is shown in Figure 3.4-2 [Hubbard 2011]. Detailed analysis of the ECE data shows that this signal is dominated by temperature fluctuations, with $\delta T_e/T_e$~2% [White 2011]. This compares with a typical density fluctuation level, from GPI, of about 10%. This could be consistent with the WCM causing more particle than energy transport, perhaps being the main mechanism responsible for the edge particle transport (relative to that in H-mode) during I-mode operation.

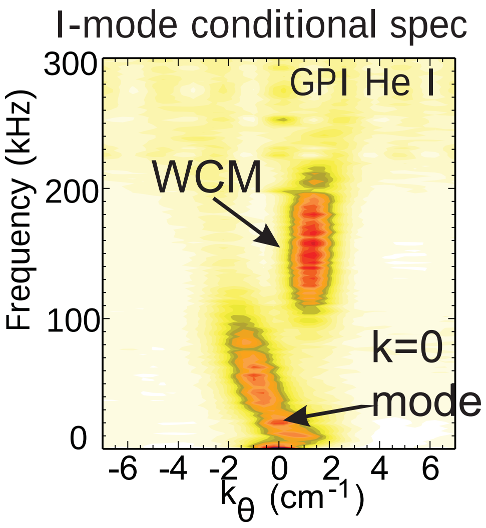

Figure 3.4-2: Conditional spectra of emissivity fluctuations measured by Gas Puff Imaging. The WCM feature is clearly visible, while a k=0 mode is difficult to see in the turbulence.

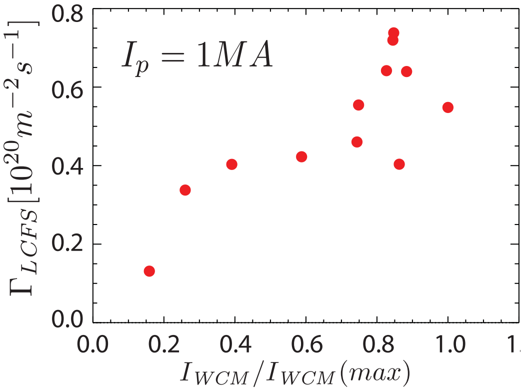

Figure 3.4-3: Particle flux as a function of the Weakly Coherent Mode (WCM) amplitude, for an I-mode experiment with I_p=1 MA and varied input power. From [Dominguez 2012].

As a test of this hypothesis, a series of experiments was performed to examine directly the relationship between density transport and the intensity of the WCM. The WCM amplitude was monitored using multiple frequencies of the reflectometry diagnostic and the deuterium particle source using an analysis of absolutely calibrated D_α imaging near the outboard midplane. Correlations were found between the radial particle flux Γ and the WCM amplitude, with an example shown in Figure 3.4-3 [Dominguez 2012]. This supports the conjecture that there is a causal relationship between the WCM and particle transport, analogous to that established by a similar technique between the QC mode and particle transport in EDA H-modes [Terry 2005].

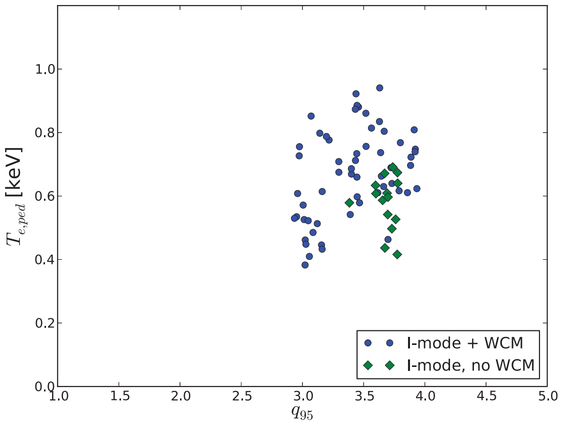

Figure 3.4-4: C-Mod I-modes with (blue) and without (green) weakly coherent mode. The discharges without WCM are at q_{95}>3.5 and moderate T_{ped}

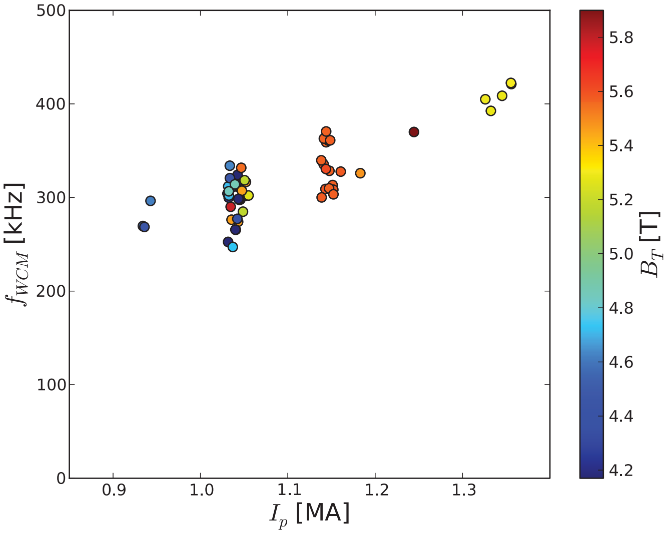

Figure 3.4-5: Center frequency of WCM, increasing with plasma current.

The WCM is strongest and most coherent in high temperature and performance I-modes, particularly at low q_{95}. It is thus very compatible with low collisionality. In some I-modes, particularly those with q_{95} >3.5 and/or input power which is marginal with respect to the L-I threshold, it is not distinguishable with available diagnostics, even though there is clear formation of a modest temperature pedestal. A number of examples of this were observed in the 2012 run campaign; in some cases phases with a WCM, and generally higher pedestals, follow phases with no WCM. The phases without WCM have some similarities to the I-modes observed in initial experiments on DIII-D, discussed in Chapter 4 of this Joint Research Target report.

If the edge is cooled, by reduction in net power, the WCM amplitude and frequency reduce and a transition to either L-mode or H-mode can result. An initial assessment of the pedestal database confirms that low q_{95} and high T_{ped} favor the WCM (Figure 3.4-4). The frequency of the mode varies with current or q_{95} (Figure 3.4-5), perhaps related to trends in pedestal rotation. While the physical mechanism of the mode is not yet clear, these observations suggest it may be driven by the strong edge temperature gradient characteristic of I-mode, or dependent on ν*. One candidate which has been proposed is the Heavy Particle Mode [Coppi 2012]. Identifying the mechanism of the mode is a key goal of the collaborative effort on gyrokinetic simulation discussed in Section 3.2, as well as these ongoing experimental studies.

4.3: Observations of GAM in I-mode

An exciting new observation in C-Mod I-modes is that of a fluctuating zonal flow in the edge region. This was detected using the same Gas Puff Imaging diagnostic previously used to measure the mode spectrum of the WCM. Velocimetry based on a time-delay-estimation (TDE) method has been recently implemented for use on the fast 2D array. This reveals a clear peak in poloidal velocity v_θ, fluctuations at typically 20 kHz, only during I-modes. An example, from the recent publication of Istvan Cziegler (UCSD Center for Momentum Transport and Flow Organization) [Cziegler 2013], is shown in Figure 3.4-6. Analysis of a number of discharges shows that its frequency scales with cs/(2pR), consistent with expectations and observations elsewhere of a Geodesic Acoustic Mode or GAM (Figure 3.4-7). This, along with analysis of its phase and coherence, identify it as a GAM.

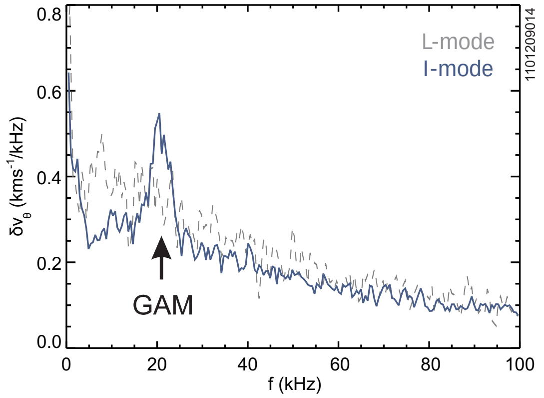

Figure 3.4-6: Poloidally averaged Fourier spectra of TDE poloidal velocities in an I-mode (solid blue) and the preceding L-mode (dashed grey). The sample size for correlation measurements is n_{cor} = 20. Spectra are time averaged from a spectrogram with df =0.5 kHz. [Cziegler 2013].

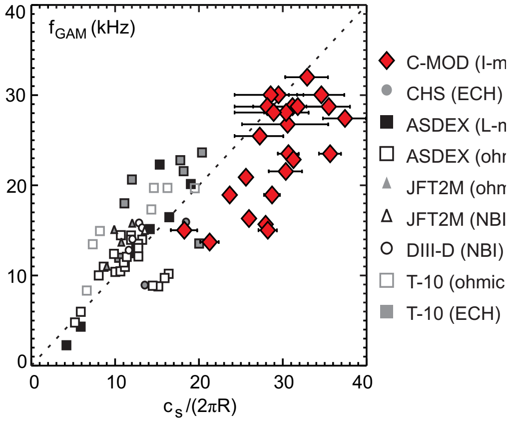

Figure 3.4-7: GAM frequencies against the theoretical c_s=R from a large number of experiments [Fujisawa 2007], with the recent results from Alcator C-Mod overlaid as the red squares. The dashed line represents ω= c_s/R [Cziegler 2013].

The observation is significant since GAMs have not previously been seen in any L-Mode or H-mode pedestals on C-Mod. In contrast, the GAM is seen in all I-mode discharges for which GPI data are available and which have been examined to date. It is not simply a transient phenomenon, but persists throughout the entire duration of the I-mode. An example is shown in Figure 3.4-8. Analysis indicates that a shift in the relative drive and damping terms for energy transfer to the GAM and the mean shear flow may be important in the I-H mode transition. This work, and similar analysis of L-H transitions, is being pursued by researchers at the Center for Momentum Transport and Flow Organization.

The GAM coexists with the previously observed WCM, which has much higher frequency, and appears to interact with it. Both modes exist in the same region, where the I-mode temperature pedestal is strong. Nonlinear spectral analysis indicates that energy is transferred between the WCM and the GAM; the fluctuating flow may well be responsible for the broad frequency of the Weakly Coherent Mode, which has been puzzling given its narrow poloidal wavenumber.

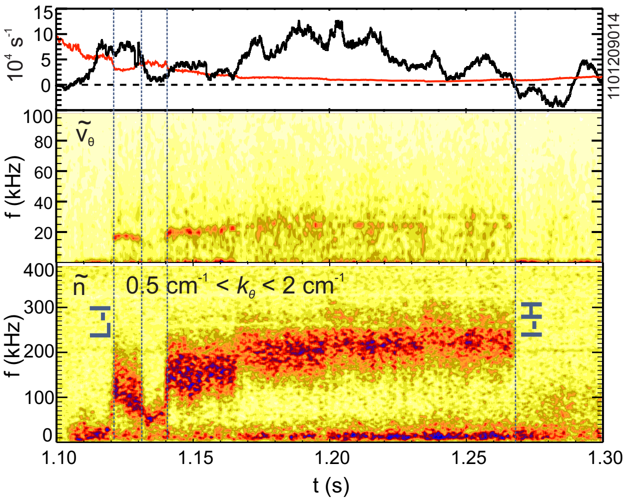

Figure 3.4-8: Evolution of the GAM (middle panel) and higher frequency Weakly Coherent Mode (lower panel), during an I-mode on Alcator C-Mod. In the top panel, the solid black line represents the estimated, time-resolved, non-linear GAM drive, and the red curve corresponds to $4\nu ii/7q$*, related to the collisional damping rate; The I-H transition occurs when the drive drops below the damping. From [Cziegler 2013].*

4.4: Changes in core turbulence at L-I transition

The reduction in broadband turbulence in the pedestal regions is, as was described in Section 4.1, one of the fundamental features of L-I transitions, and correlated to the decrease in edge thermal transport. A new and interesting observation is that core turbulence also drops significantly, and promptly, at the transition. An example is shown in Figure 3.4-9. The top contour plot shows a fluctuation spectrogram from a reflectometer channel at ρ=0.55, well inboard of the pedestal. These show a clear decrease at the L-I transition, across a broad range from 20 KHz to about 400 kHz. Because density does not change, in contrast to H-mode transitions, the reflection location stays nearly constant. No weakly coherent mode is seen in the core; as noted it is localized to the pedestal region.

More details of the time evolution and radial location of the turbulence changes are shown in Figure 3.4-10. The decrease at ρ =0.55 begins at the time that $T_{e,95}$ steps up at 0.87 s, the first dashed line. As frequently occurs, this step coincides with a sawtooth heat pulse. The slower decay of this pulse indicates a decrease in edge thermal transport, and the beginning of the L-I transition. The fluctuations at this pedestal location decrease at the same time, and to a similar degree, as those in the core. In contrast, the fluctuations at the extreme edge (ρ=0.99) do not decrease until t=0.891 s, the second dashed line. The Weakly Coherent Mode (not shown), does not appear until this later time. These observations suggest that the trigger for the transition may be at or inboard of the pedestal, with the WCM onset triggered by the formation of the temperature pedestal.

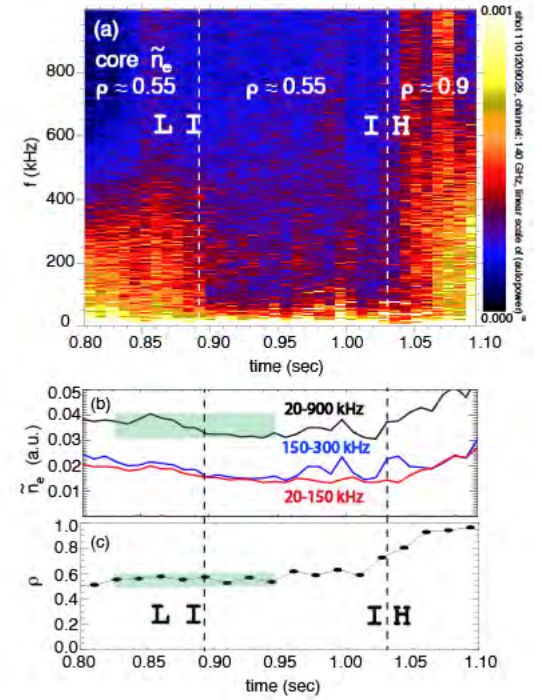

Figure 3.4-9: (a) Spectrogram of core density fluctuations across L-I transition and I-H transition. (b) Evolution of core density fluctuation level in different frequency ranges across the L-I transition. (c) Reflectometer radial measurement location remains fixed in time across the L-I transition. Green shaded region indicates time range of steady density across L-I transition.

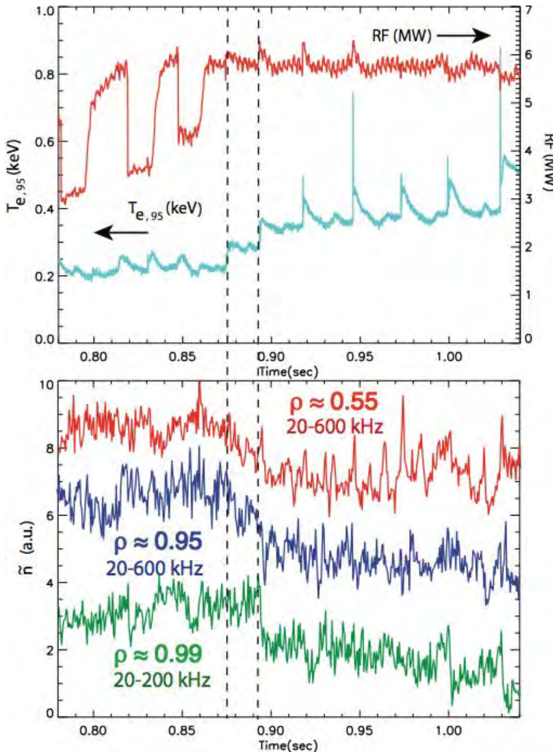

Figure 3.4-10: Temporal evolution of core and edge density fluctuation levels across the L-I transition, showing that core turbulence is reduced prior to characteristic changes in edge (ρ = 0.99) fluctuations in I-mode, and concomitant with the T_e increase, and fluctuation decrease, at ρ=0.95. The onset of the WCM (t = 0.891 sec) follows the reduction in core and pedestal turbulence.

The decrease in core density turbulence is seen in a larger set of I-mode discharges, and over a wide radial range, as shown in Figure 3.4-11. The decrease is up to 30%, and extends at least to ρ=0.45. A reduction in temperature fluctuations, measured with correlation ECE [Sung 2013] , is also observed, as shown in Figure 3.4-12. These show a significant reduction into at least ρ=0.74, the furthest this diagnostic can currently view.

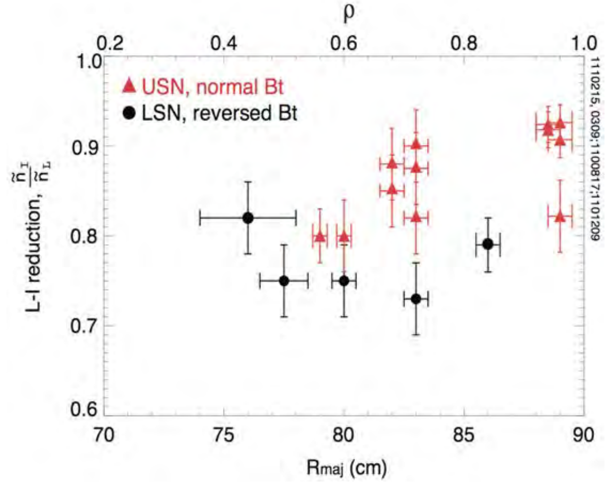

Figure 3.4-11: Relative change in density fluctuation amplitude, n-tilde, in I-mode compared to L-mode, n-tilde$_I$/n-tilde$_L$, is plotted versus radius. Since density is constant across the transition the reduction, measured with reflectometry, indicates that the relative fluctuation level n-tilde/n is reduced in I-mode.

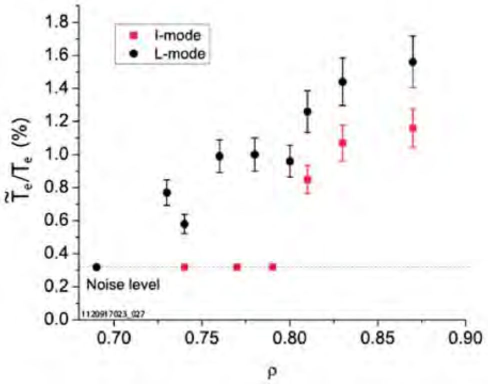

Figure 3.4-12: Reduction of long wavelength ($k_\theta\,\rho_s$ < 0.3) broadband electron temperature fluctuation amplitude (0 < f< 400 kHz), in I-mode (red) compared to L-mode (black), is plotted versus radius.

The reduction in turbulence is consistent with the increase in electron and ion temperatures across the core profile in I-modes. An example of changes in core profiles is shown in Figure 3.4-13. Analysis of transport changes in terms of growth rates and ExB shearing rates is in progress. The growth rate is calculated using GYRO [Candy 2003], and in both L-mode and I-mode the fastest growing mode is identified as an Ion Temperature Gradient mode (ITG).

A paper describing these exciting new results on core turbulence and transport changes in I-mode will soon be submitted for publication by Anne White, Choongki Sung and colleagues [White 2013].

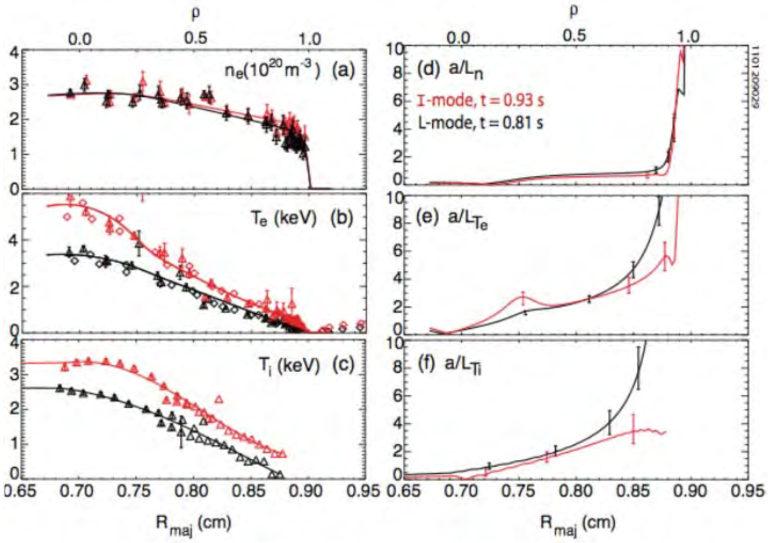

Figure 3.4-13: Changes in core density, electron temperature and ion temperature profiles across the L-I transition. I-mode profiles are in red, L-mode in black.

5.0 Remaining issues and opportunities for further work.

Much progress has been made during FY13 in the analysis and understanding of the I-mode regime on Alcator C-Mod. The regime remains highly attractive for fusion reactor scenarios, due to its combination of high energy confinement and low particle confinement. It has been demonstrated to operate at the ITER q_{95} with high performance, and shows high confinement at ITER-relevant low collisionality and external torque. There are no known physics barriers to extrapolate the I-mode regime to burning plasmas. However, further work is required to confidently extrapolate the regime to ITER, and to fully understand the physics of the regime. Many opportunities to advance this promising research remain. Some will require new experiments on Alcator C-Mod, others could be accomplished by further analysis of existing data, following up on the results recently obtained. Comparisons with I-mode experiments on other tokamaks, including those on DIII-D (see Chapter 4) and with ASDEX Upgrade and potentially several other international devices as part of ITPA joint activities will also be valuable.

In the area of expansion of operating space, the key issues are to reliably increase the input power without an I-H transition, to increase the plasma density towards higher Greenwald fraction, and to demonstrate high normalized pressure β as well as high absolute pressure. The initial experiments with fueling into an I-mode revealed a promising path for further optimization. Experiments at reduced B_T (2.6-3.5 T) would be helpful to assess whether there is a physics limit to pedestal β, since at 5 T or higher the maximum pressure and power have been limited by the available heating. Further investigation of shaping and divertor configuration would also be valuable to understand the surprising differences between operating spaces for upper and lower null plasmas illustrated in Figure 3.2-3.

Further experiments are also needed for a full characterization and analysis of the turbulence and transport which are fundamental to the I-mode regime. The observations of GAMs with GPI, which were not extracted from the data until after the last campaign, strongly motivate measurements over a wider range of parameters to understand the role of these fluctuating flows. More measurements of mean flows and E_r will also be valuable. Because both GPI and CXRS require special gas puffing these measurements are not available from the majority of prior experiments. Further information on the Weakly Coherent Mode, and potentially the GAMs, could be obtained with specialized scanning probe diagnostics, such as a magnetic probe head to measure fluctuations in B and the newly developed Mirror Probe. Important questions remain about the exact radial location and extent of these fluctuations with respect to the E_r well. Finally, use of the active 'Shoelace antenna' which was demonstrated during the FY12 campaign to interact with quasicoherent modes in EDA H-mode plasmas, and which has been upgraded during the recent maintenance period, provides an exciting opportunity to actively control pedestal particle transport and perhaps extend the I-mode regime. In the area of core turbulence and transport, the CECE diagnostic has been upgraded to probe T_e fluctuations further into the plasma. Measurements of both temperature and density fluctuations are currently limited to a small number of discharges and could be greatly extended.

Many opportunities also remain for analysis and interpretation of existing data. Techniques for analysis and interpretation of CXRS with the gas puff technique, including deconvolution of instrumental effects, have only recently been optimized. We can now apply these to a range of I-modes and investigate with more confidence the details of flows, T_i and E_r, scalings with plasma parameters, and the surprising differences in potential and/or ion temperature observed between high and low field side measurements. Stability analysis of the I-mode pedestal should be extended to other cases, including the less typical examples which did have some ELMs, to understand the limiting modes. Much remains to be done in the microstability analysis of I-mode, which has the potential to reveal the physical mechanisms of the Weakly Coherent Mode. We also hope to collaborate with theorists, including groups at UC San Diego, Univ. Wisconsin and elsewhere. The ultimate goal of this research is to understand the physics which leads to the surprising, but highly beneficial, separation of thermal and particle transport. Only with this understanding can we confidently extrapolate the I-mode regime to other experiments, including ITER and future reactors.

References

[Candy 2003] Candy J. and Waltz R.E., *J Comput. Phys.* **186**, 545 (2003).

[Carlstrom 1998] T.N. Carlstrom, K. H. Burrell and R. J. Groebner, Plasma Phys. Control. Fusion **40** 669 (1998).

[Churchill 2013a] R.M. Churchill *et al*, Rev. Sci. Instrum. **84** (2013) 0935005.

[Churchill 2013b] R.M. Churchill, B. Lipschultz, C. Theiler, and the Alcator C-Mod team, *In-Out Impurity Density Asymmetry in the Pedestal Region of Alcator C-Mod*, submitted for publication.

[Coppi 2012] B. Coppi and T. Zhou, Physics of Plasmas **19**, (2012) 012302.

[Connor 1979] J.W. Connor and R.J. Hastie, Proc. Royal Soc. London (1979).

[Cziegler 2010] I. Cziegler, *et al*, Physics of Plasmas, **17**(2010) 056120.

[Cziegler 2013] I. Cziegler, P. H. Diamond, N. Fedorczak, P. Manz, G. R. Tynan, M. Xu, A. E. Hubbard, B. Lipschultz, J. M. Sierchio, J. L. Terry, and C. Theiler, Physics of Plasmas **20** 055904 (2013).

[Dominguez 2012] A. Dominguez, Ph.D. Thesis, Physics Department, Massachusetts Institute of Technology (2012).

[Dudson 2009] B.D Dudson, *et al*. Comput. Phys. Commun. **180** (2009) 1467.

[Fujisawa 2007] A. Fujisawa, *et al*., Nucl. Fusion **47**, S718 (2007).

[Greenwald 1997] M. Greenwald, R.L. Boivin, F. Bombarda, P.T. Bonoli, C.L. Fiore, D. Garnier, J.A. Goetz, S.N. Golovato, M.A. Graf, R.S. Granetz *et al*, Nuclear Fusion **37** (6), 793 (1997).

[Greenwald 1999] M. Greenwald, R. Boivin, P. Bonoli, R. Budny, C. Fiore, J. Goetz , R. Granetz, A. Hubbard, I. Hutchinson, J. Irby *et al*, Physics of Plasmas **6**(5) 1943-9 (1999).

[Groebner 1998] R. J. Groebner and T.N. Carlstrom, Plasma Phys. Control. Fusion **40** 673 (1998).

[Groebner 2013] R.J. Groebner, C.S. Chan, J.W. Hughes, R. Maingi, P.B. Snyder *et al*, Nucl. Fusion **53** (2013) 093024.

[Howard 2011] N.T. Howard, *et al*, Review of Scientific Instruments, **82** (2011) 033512.

[Hubbard 2007] A. E. Hubbard. J. W. Hughes, I. O. Bespamyatnov, T. Biewer, I. Cziegler, B. LaBombard, Y. Lin, R. McDermott, J. E. Rice, W. L. Rowan, J. A. Snipes, J. L. Terry, S. M. Wolfe, S. Wukitch and the Alcator C-Mod Group, Phys. Plasmas **14** (5) 056109 (2007).

[Hubbard 2011] A.E. Hubbard, *et al*, Phys. Plasmas **18** (2011) 056115.

[Hubbard 2012] A E Hubbard, D G Whyte, R M Churchill, A Dominguez, J W Hughes, Y Ma, E S Marmar, Y Lin, M L Reinke and A E White, Nucl. Fusion **52** (2012) 114009.

[Hughes 2013] J.W. Hughes, P.B. Snyder, J.R. Walk, *et al*, Nuclear Fusion **53** 043016 (2013).

[ITER 1999] ITER Physics Expert Groups on Confinement and Transport and Confinement Modelling and Database, *et al*, Nucl. Fusion **39** (1999) 2175.

[Martin 2008] Y. Martin, T. Takizuka and ITPA CDBM H-mode Threshold Database Working Group *J. Physics: Conf Series*. **123** 012033 (2008).
[McDermott 2009] R. McDermott *et al* Phys. Plasmas **16** 056103 (2009).
[Mossessian 2003] D.A. Mossessian *et al*, Phys. Plasmas **10** (2003) 1720.
[Rice 2011] J.E. Rice, J.W. Hughes, P.H. Diamond, *et al*, Phys. Rev. Lett. **106**, 215001 (2011).
[Ryter 1998] F. Ryter, W. Suttrop, B. Brusehaber, M. Kaufmann, V. Mertens, H. Murmann, A. G. Peeters, J. Stober, J. Schweinzer, H. Zohm and ASDEX Upgrade Team, Plasma Phys. Control. Fusion **40**, 725-729 (1998).
[Sung 2013] C. Sung, A. E. White, N. T. Howard, *et al*, Nucl. Fusion **53** (2013) 083010.
[Snyder 2009] P.B Snyder, R.J. Groebner, A.W. Leonard, T.H. Osborne and H.R. Wilson *Phys. Plasmas* **16** 056118 (2009).
[Synder 2012] P.B. Snyder, *et al*. Nucl. Fusion **51** (2011) 103016.
[Terry 2005] J. L Terry, *et al*, Nuclear Fusion **45** (2005)1321.
[Walk 2012] J. R. Walk, P. B. Snyder, J. W. Hughes, J. L. Terry, A. E. Hubbard and P. E. Phillips, Nucl. Fusion. **52** (2012) 063011.
[White 2011] A. E. White, P. Phillips, D. G. Whyte, A. E. Hubbard, C. Sung, J. W. Hughes, A. Dominguez, J. Terry and I. Cziegler, Nucl. Fusion **51** 113005 (2011).
[White 2013] A. E. White, *et al*, *Reduction of Core Turbulence in I-mode Plasmas in Alcator C-Mod* to be submitted to Nuclear Fusion.
[Wilson 2002] H.R.Wilson, *et al*. Phys. Plasmas **9** (2002) 1277.
[Whyte 2010] D. G. Whyte, *et al*, Nuclear Fusion **50** 105005 (2010).

Chapter 4
DIII-D Contributions to the FY2013 Joint Research Target on ELM Control

M.E. Fenstermacher[1], D.J. Battaglia[2], K.H. Burrell[3], J.M. Canik[4], T.E. Evans[3],
A.M. Garofalo[3], S.P. Gerhardt[2], B.A. Grierson[2], A.E. Hubbard[5], R. Maingi[2],
D.M. Orlov[6], T.H. Osborne[3], M.W. Shafer[4], W.M. Solomon[2], and D.G. Whyte[5]

[1]*Lawrence Livermore National Laboratory, Livermore, California*
[2]*Princeton Plasma Physics Laboratory, Princeton, New Jersey*
[3]*General Atomics, P.O. Box 85608, San Diego, California 92186-5608*
[4]*Massachusetts Institute of Technology, Cambridge, Massachusetts*
[5]*University of California San Diego, La Jolla, California*

1.0 Overview

1.1 Summary of Report

The DIII-D requirements for the final quarterly milestone of the 2013 Joint Facilities Research Target (JRT13) have been met by the activities described below. The requirements of previous quarterly milestones have been met as documented in the following reports: 1) First quarterly milestone, report GA-C27505, 2) Second quarterly milestone, report GA-C27557, and third quarterly milestone, report GA-C27663. For the fourth quarterly milestone, the 2013 experiments required to address the goals of JRT13 have been executed and analysis has been performed. DIII-D contributions toward the development of high-performance stationary regimes devoid of large edge localized modes (ELMs) are summarized below in terms of both new understanding of the physical mechanisms that control edge pedestal transport, and achievement of extensions to the operating space of various stationary H-mode regimes without large uncontrolled Type-I ELMs.

The physics mechanisms that control edge pedestal transport, in particular particle transport, were explored with new diagnostic techniques in QH-mode, resonant magnetic perturbation (RMP) ELM controlled, and I-mode plasmas. Measurements of the impurity confinement time of fluorine injected into companion QH-mode and ELMing plasmas has demonstrated that the edge harmonic oscillation associated with QH-mode operation produces superior impurity flushing to ELMs, and moreover, the impurity confinement time does not increase as the toroidal rotation is reduced at constant density, despite significant improvements in the energy confinement. From very recent experiments, plasmas with strong n=1 RMP fields and net-zero input torque showed clear indications of static resonant n=1 islands in both MECH data and from Thomson T_e and electron cyclotron emission (ECE). Each of these latter diagnostics showed T_e-flattening near rational surfaces which could be related to particle transport increases through ExB convection effects. In a candidate I-mode plasma, for which a small increment in heating power leads to an edge transition, the edge temperature increases by a larger fraction than the increase in input power and simultaneously there is no change in the global or boundary density indicating that particle transport is not improved. Analysis of all of these recent observations is in progress.

The operating regimes of QH-mode, RMP ELM controlled and I-mode plasmas have been expanded by experiments done as part of this JRT. In QH-mode plasmas, simultaneous achievement of high beta, high confinement and low q_{95} needed for ITER Q=10 performance was demonstrated for 18 energy confinement times, with modest levels of neutral beam torque. Also the operating space of QH-mode plasmas was expanded to higher fractions of the Greenwald density (up to 80% in highly shaped configurations) as needed for high density operation in ITER. RMP ELM suppression was obtained in new experiment with a range of I-coil sets (12, 11, and 10 I-coils) aned extrapolation of these results shows that the ITER ELM coil system may be able to tolerate a loss of up to five of its 27 coils, while leaving a sufficient margin of current in the remaining coils to still meet the DIII-D ELM suppression criterion. Additional experiments with 9, 8, 7, and 5 I-coils were also done during the writing of this report. Finally, a large space was explored, including scans of plasma current, safety factor q_{95}, lower triangularity, and elongation, to study the response of observed I-mode regimes to these global plasma parameters, to map the H-mode threshold in this atypical magnetic topology with ion ∇B drift out of the divertor, and to determine the "operating window" of the regime.

1.2 Introduction

Operation of future tokamak devices with H-mode confinement and the associated strong edge pedestal pressure gradients, including ITER and power reactors, must include systems to control ELM instabilities in order to achieve acceptably low levels of plasma facing component (PFC) erosion. In ITER the erosion of divertor target PFCs caused by uncontrolled Type-I ELMs is predicted to limit the lifetime of these components to several hundred full power discharges. The erosion due to ELMs in a power reactor will by more than an order of magnitude greater than in ITER. Techniques to reliably reduce or eliminate PFC erosion from ELMs are critical to the viability of these future devices.

The 2013 Joint Facilities Research Target (JRT) focuses the combined resources of the NSTX, C-Mod and DIII-D programs on understanding the physics mechanisms for and extending the operating space of multiple techniques of stationary tokamak operation without large uncontrolled Type-I ELMs. The text of the 2013 JRT and the associated quarterly milestones are below

Annual Target

> Conduct experiments and analysis on major fusion facilities to evaluate stationary enhanced confinement regimes without large ELMs and to improve understanding of the underlying physical mechanisms that allow acceptable edge particle transport while maintaining a strong thermal transport barrier. Mechanisms to be investigated can include intrinsic continuous edge plasma modes and externally applied 3D fields. Candidate regimes and techniques have been pioneered by each of the three major US facilities (C-Mod, D3D and NSTX). Coordinated experiments, measurements, and analysis will be carried out to assess and understand the operational space for the regimes. Exploiting the complementary parameters and tools of the devices, joint teams will aim to more closely approach key dimensionless parameters of ITER, and to identify correlations between edge fluctuations and transport. The role of rotation will be investigated. The research will strengthen the basis for extrapolation of stationary regimes which combine high

> energy confinement with good particle and impurity control, to ITER and other future fusion facilities for which avoidance of large ELMs is a critical issue.
>
> **Quarter Milestones**
>
> **1st Quarter Milestone**. Begin analysis of previously collected data with a goal of defining new experiments. Develop an initial plan for collaborative experiments and analysis in the 2nd half of the fiscal year.
>
> **2nd Quarter Milestone**. Utilize data analysis to define a final plan for experiments in the 2nd half of FY-13 on at least a single facility, including diagnostic and operations requirements.
>
> **3rd Quarter Milesto**ne. Begin planned experiments on at least a single facility. Evaluate results, including comparisons to previous data, and adjust analysis and experimental plans as necessary.
>
> **4th Quarter Milestone**. Complete the required experiments and analysis. Prepare a joint report summarizing the contributions toward the development of high-performance stationary regimes devoid of large ELMs, and identifying important paths for future exploration.

There is a duality to the objectives of JRT2013: it includes both investigation of the underlying physics mechanisms that control edge pedestal transport (in particular particle transport) during ELM control techniques, and exploration of the possible extension of the operating regimes of various techniques to a broader range of tokamak operating parameters, which also tests the governing physics mechanisms.

The DIII-D program has contributed to the completion of JRT 2013 through both the execution and analysis of multiple experiments focused on several of the leading ELM control techniques. Multiple experiments have been executed using QH-mode plasmas, I-mode operating regimes, VH-mode plasmas, and resonant magnetic perturbation (RMP) ELM control techniques. Experiments have been focused on both aspects of JRT2013 vis: some have targeted the detailed mechanisms controlling edge particle transport during ELM control and others have concentrated on expanding the operating regimes for various techniques. A summary of the experiments executed within the scope of JRT2103 is given in Table IV.1.2-1

Table IV.1.2-1 DIII-D Experiments in 2013 Contributing to JRT13 Goals. Research Areas: B&PP: Boundary and Pedestal Physics, D&C: Dynamics and Control; JRT13 Goals: TPM: Transport Physics Mechanisms, PE: Performance Extension

Regime	Title	Research Area	JRT13 Goal
I-mode/ T-III ELMs	Density transport in small and no ELM regimes: Compare Type III ELMy H-mode, I-phase, and "I-mode candidate" in DIII-D	B&PP	PE
I-mode/ T-III ELMs	Density transport in small and no ELM regimes: Compare Type III ELMy H-mode, I-phase, and "I-mode candidate" in DIII-D	B&PP	TPM
RMP	Measure dependence of magnetic island ExB convective transport as a function of toroidal rotation	B&PP	TPM — Not completed
RMP	Study n = 3 RMP transport asymmetries with applied RMP phase FLIPS to identify and document conditions that minimize pedestal pressure reduction	B&PP	TPM
RMP	RMP ELM suppression with less than 12 I-coils for ITER	B&PP	PE
VH-mode/ RMP	Extend VH-mode duration using 3D fields from the I-coil and C-coil and document the pedestal properties	B&PP	PE
QH-mode	Determine edge harmonic oscillation (EHO)-induced particle transport rates at ITER-relevant conditions	D&C	TPM
QH-mode	QH-mode creation and sustainment with ITER-relevant co-I_p NBI torque	D&C	PE
QH-mode	Sustain low torque QH-mode at high normalized Fusion performance for alternate to ITER baseline	D&C	PE
QH-mode	Density and collisionality dependence of EHO	D&C	TPM & PE

The organization of this report is aligned with the requirements of JRT2013, vis. Section 2 describes experiments and analysis focused on effects of various techniques on edge transport, Section 3 concentrates on experiments and analysis that test the physics limits of operating regimes for various techniques, and Section 4 summarizes paths for future exploration indicated by the work done this year.

2.0 Experiments and Analysis Focused on Particle Transport Physics Mechanisms

2.1 Effect of the EHO on Edge Particle Transport in QH-mode Plasmas

2.1.1 Goals and Background

The primary goal of this experiment was to determine the rate at which a non-intrinsic, non-recycling impurity is transported out of a QH-mode plasma for a range of experimental conditions, and to contrast this rate with that in ELMing H-modes. QH-mode conditions are theoretically predicted to be maintained by the edge harmonic oscillation (EHO), and this experiment focused on quantifying the particle transport rates in the presence of an EHO, including the possible effect of neoclassical ion transport in the edge of QH-mode plasmas (see the JRT appendix). This is an important issue for ITER in which all ELM control techniques must show that core accumulation of tungsten sputtered in the divertor region can be prevented.

The key experimental technique used in the experiment to directly measure the edge impurity particle confinement was the injection of multiple short pulses of carbon tetraflouride (CF_4) gas and the monitoring of the decay of the fluorine in the edge pedestal with the charge exchange recombination (CER) system tuned to a fluorine line. The experimental conditions were optimized to include a set of EHO mode numbers from n=1, 2, 3 and broadband fluctuations. Further, the dependence on plasma density, toroidal rotation and applied 3D magnetic perturbations were used to assess the particle transport. Shot-by-shot scans of parameters were done, with other global variables fixed when possible. ELMing versions of these QH-mode conditions were also produced throughout the experiment, and data from these periods are being analyzed for comparison with the high priority QH-mode measurements. In all cases more comprehensive measurements were acquired for detailed modeling of the particle transport [E_r and motional Stark effect (MSE) for equilibrium, BES, UF-CHERS for turbulent fluctuations], besides the gross observable of the particle confinement time τ_p from the simple decay of the fluorine charge-exchange emission intensity.

2.1.2 Results Contributing to JRT13 Goals

Measurements of the impurity confinement time of non-intrinsic, non-recycling fluorine injected into companion QH-mode and ELMing plasmas has demonstrated that the edge harmonic oscillation associated with QH-mode operation produces superior impurity flushing to ELMs, and moreover, the impurity confinement time does not increase as the toroidal rotation is reduced at constant density, despite significant improvements in the energy confinement. Fluorine particle confinement time as a function of plasma line-averaged density (Fig. IV.2.1-1) shows that in the QH-mode phases the impurity particle confinement is lower than in the ELMing phase, suggesting better impurity flushing from the plasma by the EHO than by ELMs. Flourine particle

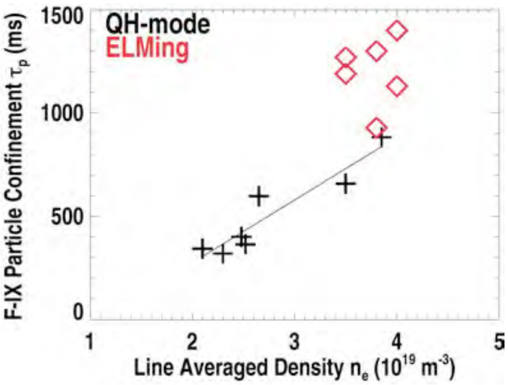

Fig. IV.2.1-1. Fluorine particle confinement time vs line-averaged density for ELMing H-mode and QH-mode operation.

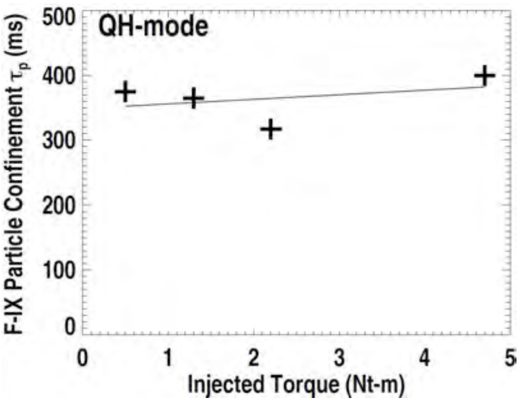

Fig. IV.2.1-2. Fluorine particle confinement time vs injected neutral beam torque for QH-mode operation at constant density.

confinement as a function of injected NB torque during QH-mode operation at fixed density (Fig. IV.2.1-2) shows little dependence on the input torque. Edge ((Ψ_N=0.8) toroidal rotation varies a factor of 5 (10–50 km/s) and central rotation varies more than a factor of 50 (2–120 km/s) from the low to high end of this torque scan. These results are particularly important because there is concern that ELM-suppressed regimes may lead to impurity accumulation without the flushing typically associated with ELMing conditions. This experiment shows that the impurity flushing in QH-mode is higher than in ELMing H-mode.

2.2 Determining the RMP Fields Internal to the Plasma and Their Effect on Edge Particle Transport

2.2.1 Goals and Background

The purpose of this experiment was to examine the plasma response to 3D non-axisymmetric magnetic perturbations as part of efforts to build a comprehensive model of the self-consistent fields internal to the plasma and the effect of those fields on edge particle transport, under application of external resonant magnetic perturbation (RMP) fields. The experiment examined the changes in topology, transport (particle and energy) and turbulence using n=1 magnetic perturbations in inner-wall limited (IWL) plasmas. Although not optimized for RMP ELM suppression, the applied fields were predicted to generate the largest magnetic island structures possible within DIII-D plasmas. In combination with IWL plasmas, these n=1 perturbations allowed for better diagnostic access to test plasma response models, similar to previous work in O. Schmitz *et al.*, Nucl. Fusion **52**, 043005 (2012). This experiment took advantage of advancements in diagnostic access, numerical modeling and experimental tools. The plan was to advance validation of vacuum and resistive MHD calculations of self-consistent internal fields by comparing data against synthetic diagnostic results from the code simulations, and to eventually fold that predictive capability for the internal fields into code simulations of the effect on particle transport based on several different theoretical mechanisms.

Application of RMPs is a robust ELM control technique on DIII-D [1]. However, the understanding of this process is incomplete, and it is crucial to develop predictive capability of this technique for ITER. A current working theory is that the RMP creates some mechanism that restricts the inward pedestal growth, preventing the pedestal from reaching a peeling-ballooning limit [2]. One proposed mechanism is that an island is formed at the top of the pedestal due to the RMP fields, and this is supported by recent resistive two-fluid linear MHD modeling [3]. This modeling suggests that screening of the externally applied RMP fields by the plasma is diminished where perpendicular electron flow is low, which is possible at the top of the pedestal. This is in contrast to vacuum modeling, which suggests high levels of stochasticity throughout the pedestal.

To enhance the ability to measure the contrast between the vacuum model predictions and the full plasma response prediction of the RMP fields in the plasma, the experiment was designed with IWL plasma shape and strong n=1 RMP fields applied by the C-coil. Lower n (as opposed to n=3) reduces the “pileup” of neighboring resonant surfaces. Similarly, limited plasmas reduce edge shear to reduce the pileup as well. This simplifies the modeling of the plasma response for a particular surface. This also allows better diagnostic access of outboard midplane measurements. Another key benefit is the reduction of the strong separatrix deformation from homoclinic tangles (which requires an X-point). A key technique featured in this experiment was the use of modulated electron cyclotron heating (MECH) power. ECH pulses have been used successfully in LHD and TEXTOR to study changes in the magnetic topology, i.e., nested flux surfaces, small isolated magnetic islands, mixed islands and stochastic layers and regions of strong stochasticity, due to intrinsic resonant magnetic fields and applied RMP fields [4–6]. The experiment also used differential phase-locked imaging with the tangential filtered X-point soft x-ray (SXR) camera, similar to previous successful techniques in n=3 RMP ELM suppression experiments. Images using a low energy filter ($T_e \geq \sim 40$ eV) show lobe structures consistent with vacuum calculations. Conversely, using a higher energy filter ($T_e \geq \sim 400$ eV), images show helical kink-like displacements localized in the steep gradient region consistent with calculations with the linear resistive two-fluid MHD code, M3D-C1 [3]. Similar to the differential phase-locked imaging, traveling n=1 waves were also used for better access by midplane visible cameras and ECEI.

2.2.2 Results Contributing to JRT13 Goals

This experiment was completed less than a week before the deadline for submission of this report, but based on control-room analysis, seemingly clear indications of static resonant n=1 islands were observed in Thomson T_e and electron cyclotron emission (ECE) at net-zero input torque. Each of these diagnostics show T_e-flattening near rational surfaces. By increasing the torque slightly, the island signatures went away – potentially giving a first indication of resonant screening of non-axisymmetric fields via rotation. Proper evaluation of relevant rotation quantities will be needed to determine the details of the apparent screening effects. Scientists from NIFS (Ida and Ohdachi) who collaborated on this experiment used modulation ECH to probe the same plasmas and corroborated the location of islands O- and X-points. The change in radial propagation speed of MECH pulses helped to indicate the difference between nested flux surfaces, islands and stochastic regions. Also, IWL H-modes were found at low power, which was unexpected. This was highly dependent on C-coil phase. Further analysis showed that the favorable C-coil phase in H-mode was consistent with the standard error field correction phase. Reciprocating probe measurements in the backend low-power phase showed degradation of floating potential gradient (possible increasing stochasticity) and plasma potential (possible increase of ion loss) as perturbation current is increased. Further analysis will be done as follow-up to the 2013 JRT.

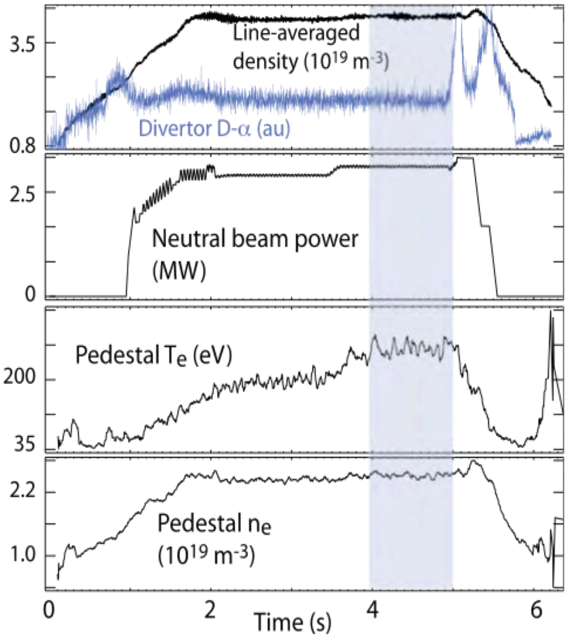

Fig. IV.2.3-1. Example shot (#153023) where a candidate I-mode appears (the shaded region). A substantial (>25%) increase in pedestal T_e occurs with constant core and pedestal density with a <10% increase in injected power. The recycling D_α light in the divertor indicates that no H-mode transition or ELM activity occurs.

2.3 Edge Particle Transport During I-mode Plasma Operation in DIII-D

2.3.1 Goals and Background

The goal of this experiment was to explore and characterize the particle and thermal transport features of ELM-free regimes for comparison to the other facilities. A magnetic configuration with the ion grad-B drift pointed away from the primary X-point was used, i.e. a topology with “unfavorable” power access to H-mode, but which has been used to explore I-mode in C-Mod. The experimental plan used steps of neutral beam input power within a shot to explore the parameter space of I-mode/small-ELM regimes and the transition to H-mode (Fig. IV.2.3-1). A large suite of boundary fluctuation diagnostics was simultaneously focused on these plasmas in order to obtain more complete information on the role of small-scale MHD in regulating particle and energy transport. The fluctuation diagnostics data will be critical in determining any bifurcations in pedestal/core fluctuation behavior that are expected to occur at an L-I-mode transition (based on observations from ASDEX-Upgrade and C-Mod).

2.3.2 Results Contributing to JRT13 Goals

A candidate I-mode phase is shown in Fig. IV.2.3-1 where a small increment in heating power leads to an edge transition, i.e. where the edge temperature increases by a larger fraction than the increase in input power. Simultaneously there is no change in the global or boundary density. It is just such a transition in energy transport, and the formation of a T_e pedestal, in the absence of improved particle confinement, which is the key feature of I-mode. The development of a boundary temperature/energy barrier is evident in Fig. IV.2.3-2 in the candidate I-mode phase. While no standard H-mode transition occurs, the D_α recycling light indicates complex behavior that evolves throughout the different phases, as do related density fluctuations in the pedestal from the BES diagnostic. These fluctuations are presently being analyzed and being compared to Type-III ELM regimes.

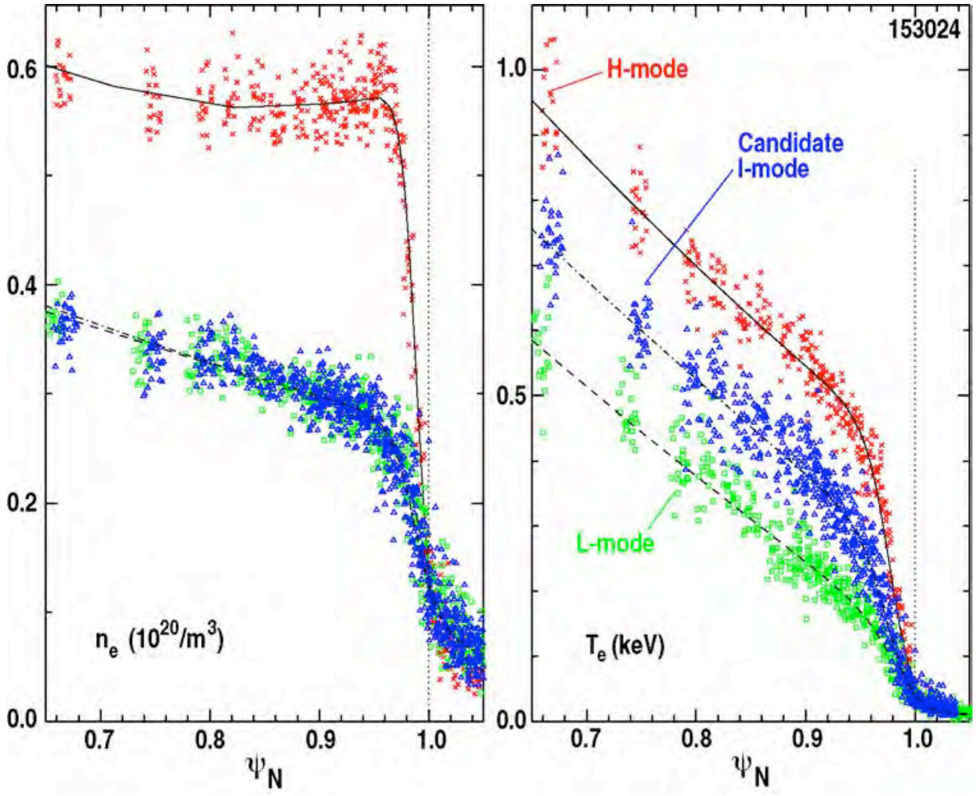

Fig IV.2.3-2. Example edge profile (#153050) comparing boundary T_e profiles between a standard L-mode with no pedestal and a candidate I-mode phase where an edge thermal barrier begins forming with only a small increment in beam heating.

2.4 Conclusions

The experiments and analysis focused on the physics controlling the edge particle transport pioneered new diagnostic techniques to make direct measurements of impurity particle confinement and the effects of externally applied fields on internal magnetic and plasma profiles. Measurements of fluorine transport from short puffs of CF_4 was and will be an important technique to directly measure impurity confinement in stationary regimes without large ELMs. MECH is a valuable technique to explore the internal magnetic structure within these plasmas. The data and analysis to date certainly suggest that the role of 3D magnetic fields could be a common feature of the particle transport control in QH-mode, RMP ELM control and I-mode plasmas. At this point further analysis is still required to determine the details of commonality in the physics mechanisms that control the edge particle transport in these regimes.

3.0 Experiments and Analysis Focused on Testing Physics Limits to Operating Regimes

3.1 Exploring the I-mode Operating Space in DIII-D

3.1.1 Goals and Background

The goal of this experiment was to explore the operating space near the parameters of a previous DIII-D discharge from last year that showed I-mode characteristics. The strategy was to alter parameters that are known to affect (or avoid) transition into a standard H-mode, namely density, X-point position, and plasma current. This scan occupied the first half-day.

The second part of the experimental plan was focused on using the best discharge of the first run and providing further exploration of the regime. Options included: 1) varying the input beam in order to examine the role of input torque, 2) exchanging the NBI heating with ECH to both examine the role of torque and direct electron heating, 3) varying the magnetic balance to examine the role of the H-mode power threshold and/or threshold for obtaining Type-III ELMs, 4) Exploring the accessibility/maintainability space of I-mode with respect to density, in particular the ability to raise the density once in I-mode through simple gas fuelling while simultaneously increasing the power including the boundary fluctuation response to density/power scans, and 5) closer examination of pedestal particle transport by local particle balance (edge filterscopes), which required an outer gap scan, and/or modification to puffing location. We also considered non-perturbing argon puffing to assess particle transport.

DIII-D experiments carried out in 2012 with ion grad-B drift pointed away from the primary X-point, showed that a temperature barrier was forming in the absence of a density barrier, a key feature of the I-mode regime. The most promising discharge (#149908) was part of a large scoping study exploring access to I-mode and thus small variations near the conditions of 149908 were not explored in detail. Analysis of edge density fluctuations indicated that small-scale instabilities were present including 2–4 kHz bursts in recycling, as well as higher frequency ~50 kHz precursor events. It was speculated that such edge modes were responsible for strong particle transport and inhibited the formation of density pedestal. These fluctuation features have some qualitative resemblance to those in low density Type-III ELMy H-modes. Discovering commonalities to small ELM and no-ELM regimes is a central theme to the 2013 JRT. This experiment was designed to expand our limited set of fluctuation data for this candidate I-mode regime in DIII-D and compare with measurements from Type-III ELMing H-mode.

3.1.2 Results Contributing to JRT13 Goals

A large space was explored in the DIII-D experiment to study the response of this no/small ELM regime to global plasma parameters, to map the H-mode threshold in this atypical magnetic topology, and to determine the "operating window" of the regime. A graphical summary of the parameter scan in plasma density versus input beam power is shown in Fig. IV.3.1-1.

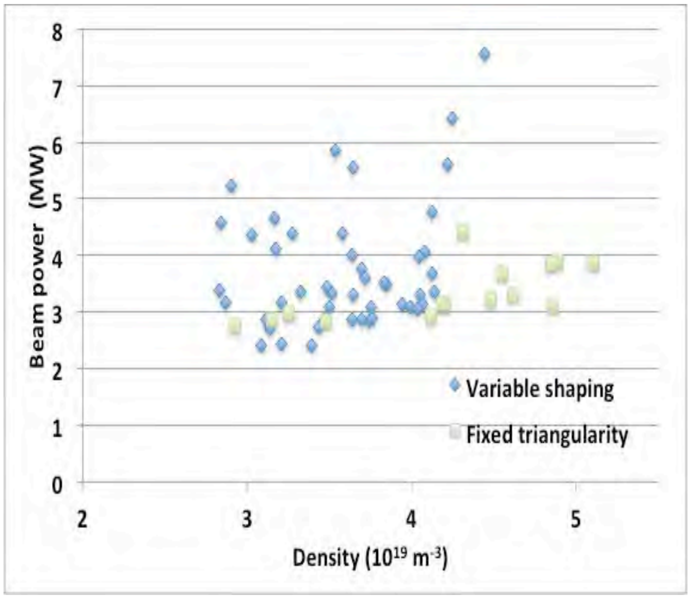

Fig. IV.3.1-1. Parameter space of core density vs input beam power covered in the experiment. All points are either in L-mode or candidate I-mode phases. No H-modes are shown. All plasmas have a lower single null shape. The "fixed triangularity" cases have a lower triangularity of 0.53.

The parameter scans also included: 1) plasma current: 1–1.5 MA, 2) safety factor q_{95}: 3.3–5.2, 3) lower triangularity: 0.37–0.72, and 4) elongation: 1.62–1.72. It is noted from Fig. IV.3.1-2 that the "unfavorable" topology leads to a substantial increase in the allowed input power before H-mode is accessed, which would typically occur on DIII-D at ~1.5 MW for the B_T=2 T used in the experiment. It is apparent that both shaping and density play roles in determining the H-mode threshold, a result qualitatively consistent with previous experience.

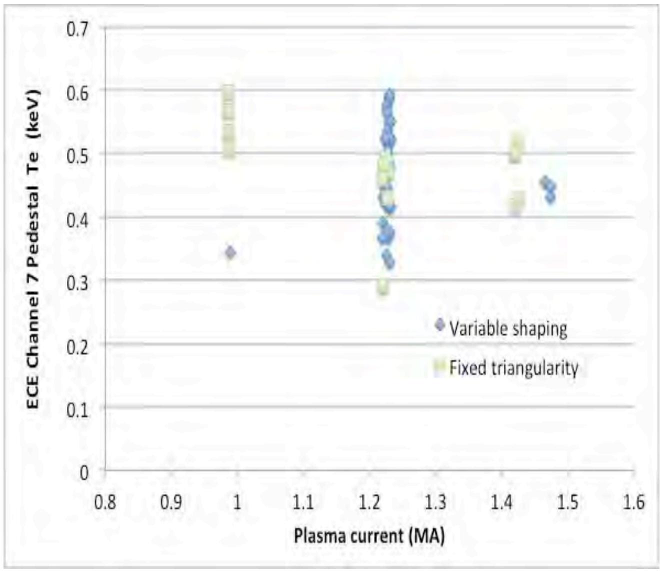

Fig. IV.3.1-2. Achieved edge/pedestal T_e (measured with ECE channel 7) vs plasma current. All plasmas lower single null before any H-mode transition. The green squares have a constant lower triangularity of 0.53.

While candidate I-mode slices were identified, the overall DIII-D energy confinement improvement was modest, with a maximum H_{98y2} ~ 0.75. Preliminary assessment shows that the expected evolution of the T_e pedestal is cut short by H-mode transitions, which are occurring at a relatively earlier stage in the pedestal formation than seen in C-Mod or ASDEX-Upgrade. The cause of the T_e pedestal termination appears to be sawteeth heat pulses. The importance of sawteeth is shown in Fig. IV.3.1-2 where the highest pedestal T_e is found at the lowest plasma current.

The sawteeth heat pulses are substantially smaller at lower current (higher safety factor), which allows the candidate I-mode phase to reach higher T_e before the H-mode. This effect is strong enough on DIII-D to counter the expected degradation in confinement/pedestal height at the lower plasma current, which is seen on C-Mod. This result suggests that sawtooth suppression/control may be more important than high plasma current to accessing higher performance I-mode phases in DIII-D.

From the discharge this year the scaling of the power threshold for the I- to H-mode transition shows similarities with previous scalings found for the threshold from Type-III to Type-I ELMs. Figure IV.3.1-3 shows the I-H threshold power (and that threshold power normalized to the ITER L-H power threshold scaling) as functions of density normalized to the square of the poloidal field. These data were taken for discharges at a fixed shape and toroidal field by scaning the plasma current. The shape of the I-H threshold power is similar to the previous scaling of TIII – TI ELMing regime transition power scaling of $P_{\mathrm{TIII\text{-}TI}} \sim I_P^{2.4}/n_e^2$ [7].

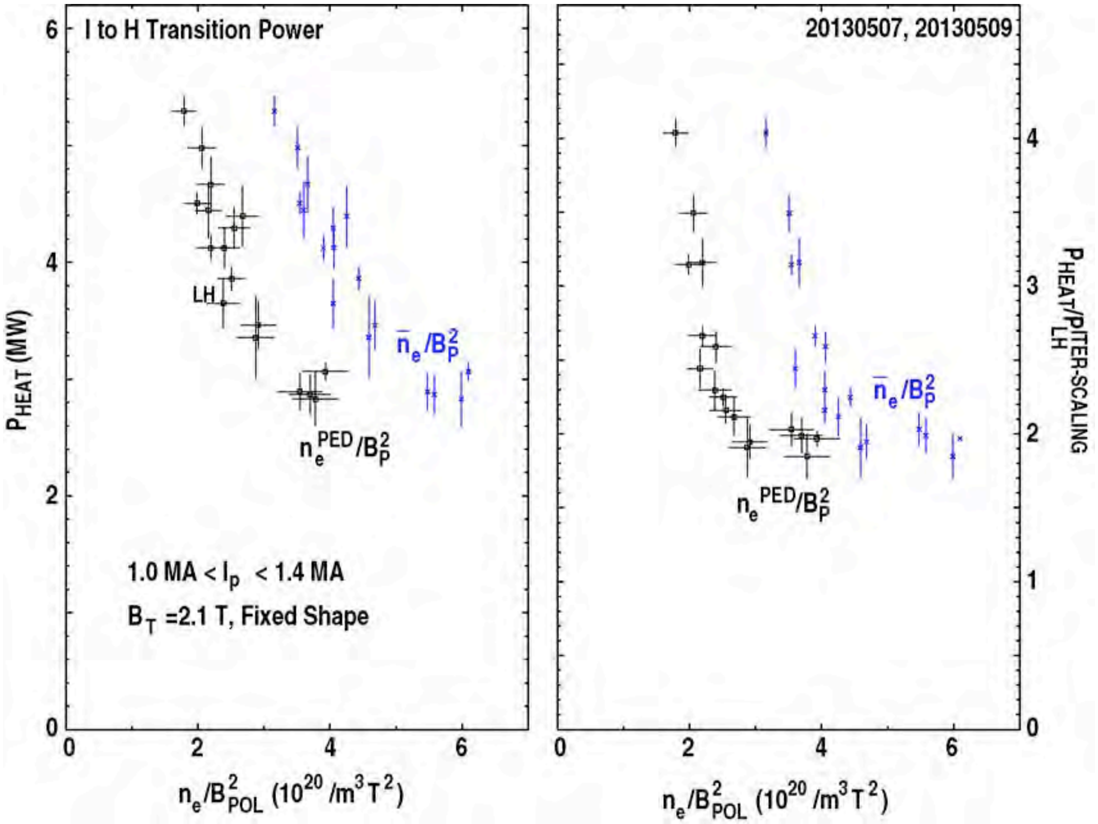

Fig. IV.3.1-3. I-H transition power threshold (MW and normalized to ITER L-H power threshold scaling) as functions of density normalized to (poloidal field)^2.

Comparison of pedestal characteristics important to stability analysis between I-mode and ELMing H-mode cases show the I-mode is significantly away from stability boundaries that produce ELMs. Figure IV.3.1-4 shows normalized pedestal electron temperature, normalized pedestal total pressure, and pedestal alpha parameter (pressure gradient) all as functions of density normalized to poloidal field. The I-mode cases are at lower temperature, lower pressure and lower pressure gradient than comparable H-mode cases. Figure IV.3.1-4 also shows that the I-mode pedestals are significantly wider than comparable ELMing H-mode pedestals, and wider than suggested by EPED scaling.

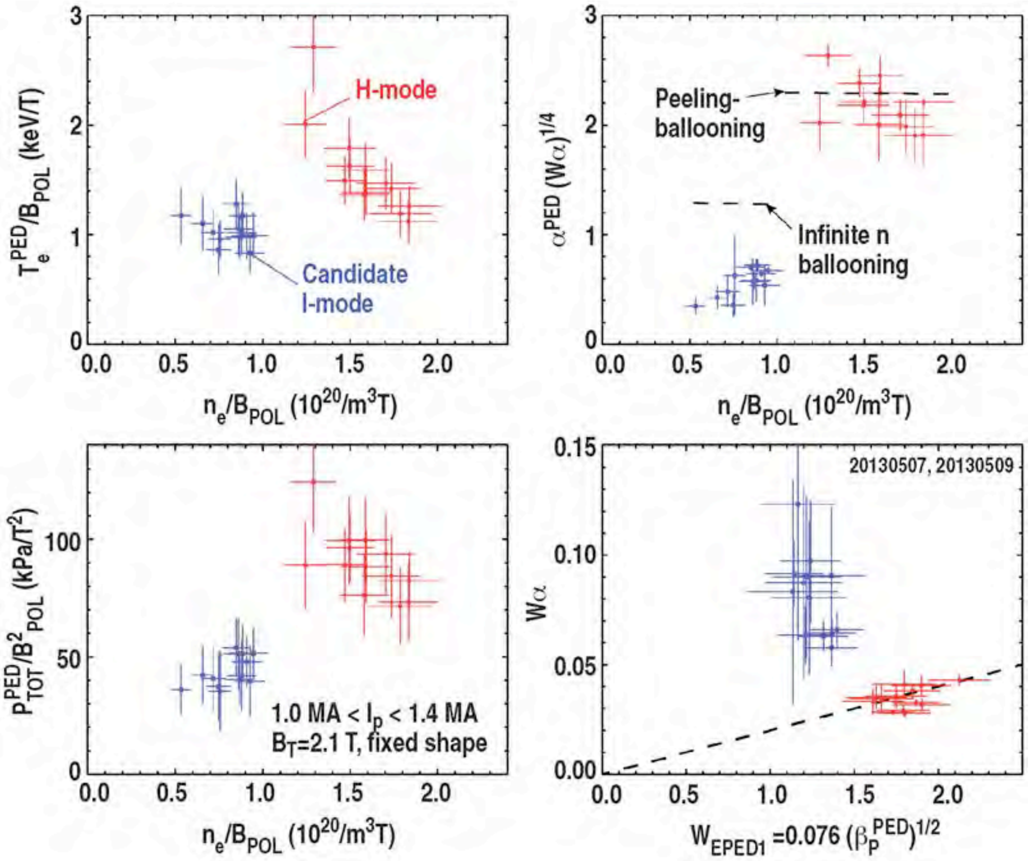

Fig. IV.3.1-4. Pedestal parameters important to stability analysis for DIII-D I-mode vs comparable ELMing H-mode cases.

3.2 Extending QH-mode Operation to High Fusion Performance

3.2.1 Goals and Background

The experiment to sustain low torque QH-mode at high normalized fusion performance, as an alternate to ITER baseline, focused on extending the operational space of the QH-mode regime to overlap with key constraints associated with ITER baseline operation, in particular the low values of q_{95} and co-I_p input torque simultaneous with good confinement (H_{89p}=2) and moderate normalized beta (β_N~2). The goal was to obtain a value of the normalized fusion performance parameter $G=\beta_N H_{89}/q_{95}^2 \sim 0.4$ sustained in QH-mode for duration >5τ_L with net NBI torque between 0 and 1 Nm.

QH-mode experiments in November 2012 achieved for the first time QH-mode operation at high fusion performance parameter G=0.4 with very low NBI torque. These experiments were carried out with forward I_p and reversed B_T, and used an upper biased DND plasma cross section, C-coil n=3 operation at 7 kA to produce the edge rotation shear required for QH-mode, RWM feedback operation using I-coils, and a recent boronization of the DIII-D vessel. The value of G=0.4 was achieved only briefly, before a locked mode terminated the high beta phase. Furthermore, the value of G=0.4 was achieved with NBI torque in the counter direction, although at very low level of about 0.5 Nm.

The new experiment, focused on the JRT goals, aimed more simply at reaching low q_{95} at the moderate $\boldsymbol{\beta}_N$ ~ 1.8–2.0 of the ITER baseline scenario. Without a specific reason for off-axis current drive from the tilted NB line, the proposed experiment operated in the more established counter-rotating QH-mode with reversed I_p and forward B_T.

3.2.2 Results Contributing to JRT13 Goals

Simultaneous achievement of high beta, high confinement and low q_{95} needed for ITER Q=10 performance was demonstrated for 18 energy confinement times, with modest levels of neutral beam torque. QH-mode at normalized fusion performance corresponding to Q=10 in the ITER baseline scenario (i.e. $\beta_N H_{89p}/q_{95}^2 \sim 0.4$) was easily obtained at q_{95}~3.2, but only with counter neutral beam injection (NBI) torque. High performance QH-mode operation was obtained in both USN and LSN plasmas shapes as shown in Figs. IV.3.2-1 and IV.3.2-2. Reducing the counter-I_p torque led to a locked mode in these initial experiments. The torque threshold for locked modes is lower at higher q_{95}, and at q_{95}~4.7 the NBI torque can be reduced to zero without locked modes. Improved error field correction using resistive wall mode (RWM) feedback should be a promising tool to overcome the locked mode limitation. Increasing the density was not attempted in the time available, but this would have a strong impact on the locked mode behavior.

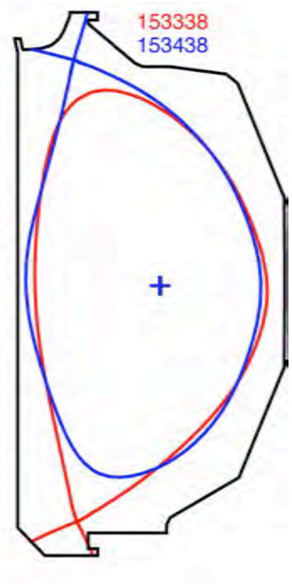

Fig. IV.3.2-1. USN (blue) vs LSN (red) shapes used for high performance QH-mode experiments.

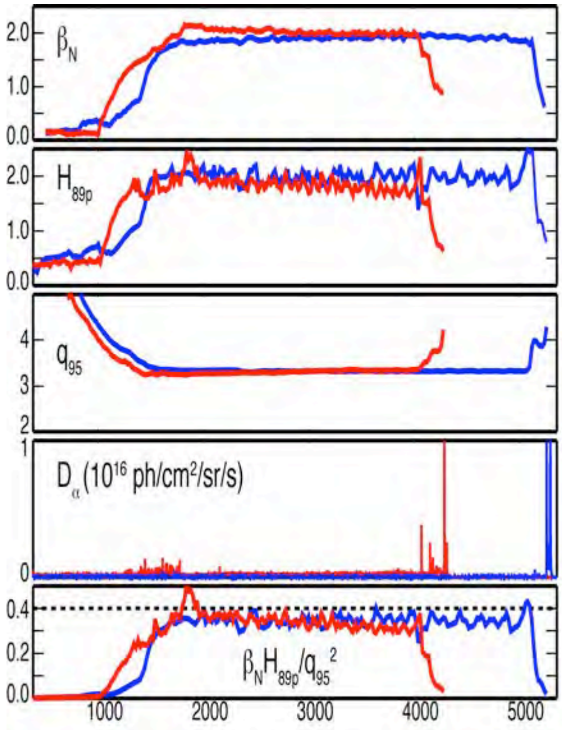

Fig. IV.3.2-2. Comparison of high fusion performance QH-mode plasmas in both USN (blue) and LSN (red) shape.

3.3 Exploring the Density and Collisionality Limits of QH-mode Operation

3.3.1 Goals and Background

There were two major goals for this experiment, vis.: 1) to investigate the physics of the QH-mode density limit, in particular to show that access to QH-mode is not correlated with Greenwald fraction, consistent with model predictions, and that collisionality (via its effect on bootstrap current) is the relevant density parameter, and 2) to document the EHO mode structure under the wide range of conditions and compare with both linear eigenmode calculations as well as calculations from the nonlinear MHD code JOREK. The experiment was also designed to test model predictions for how the plasma shape and rotation influence the density limit. In particular the experiment was designed to acquire data related to the rotation requirements for the EHO, which will be used in simulations to help demonstrate that the EHO is indeed a peeling mode saturated by edge rotational shear. These were important JRT13 related steps to improve the confidence that QH-mode can be accessed in ITER at high Greenwald fraction, as predicted.

Experiments have previously shown that increased shaping can increase the QH-mode density limit, and reduced rotation appears to reduce the particle transport driven by the EHO, also leading to higher density QH-modes. However, the highest density QH-modes on DIII-D are still at relatively low Greenwald fractions ($n/n_G \sim 0.6$) compared with ITER requirements. Hence, an often-cited concern is that QH-mode may not be ITER relevant. Stability to ELMs is thought to be maintained via increased particle transport driven by the EHO. There have been various efforts to investigate the EHO mode structure, but no systematic effort has been made to compare with predicted mode structures, so relevant data was collected in this experiment, particularly as part of a q_{95} scan which changed the mode structure. Previously, the shear in the rotation driven by the radial electric field, $\omega_E = E_r/RB_\theta$ was found to be an important parameter for QH-mode operation [8]. This work argued that the appropriate non-dimensional quantity involved normalizing to the Alfven frequency. This experiment explored different toroidal fields as part of the density/collisionality variations to test this rotation normalization also.

3.3.2 Results Contributing to JRT13 Goals

Consistent with the JRT13 goal to explore and expand the boundaries of operating spaces for stationary regimes without ELMs toward more ITER relevant conditions, these experiments expanded the operating space associated with QH-mode plasmas to higher fractions of the Greenwald density as needed for high density operation in ITER. The density requirements for QH-mode access were investigated and no correlation with Greenwald fraction was found. Indeed, with high shaping, Greenwald fractions exceeding 80% have now been achieved (Figs IV.3.3-1 and IV.3.3-2), and density can be controlled during the QH-mode phase with either pellets or gas puffing. High density QH-mode operation is qualitatively consistent with modeling using the ELITE code, indicating that strong shaping expands the kink/peeling stability boundary to higher pressure and current, allowing access to higher densities without destabilizing ELMs. Importantly, calculations with both the EPED and ELITE codes predict that the expected density on ITER is compatible with QH-mode operation in the ITER shape.

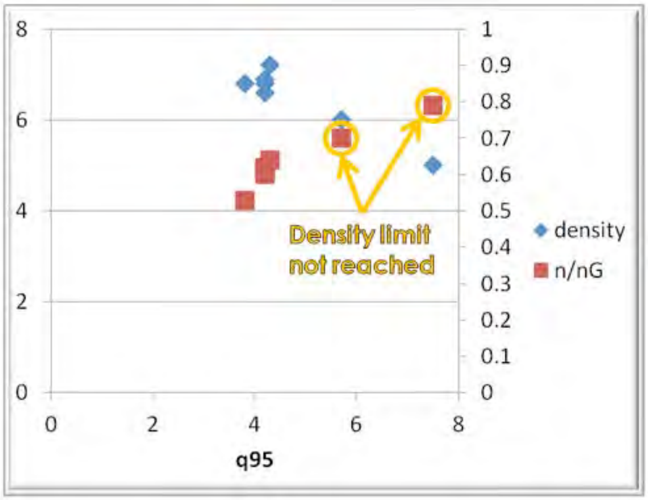

Fig. IV.3.3-1. Density and Greenwald density fraction achieved during QH-mode operation as functions of q_{95}. For the discharges above q_{95}=5 the actual limit was not reached and is likely higher than shown.

3.4 Developing QH-mode Creation and Sustainment Scenarios with Low Co-I_p Torque

3.4.1 Goals and Background

The goal of this experiment was to investigate techniques to create and sustain QH-mode with NBI torque levels relevant to next-step devices such as ITER. Work in the 2011 and 2012 campaigns demonstrated sustained QH-mode operation with ITER relevant NBI torque in the range of 0 to 1 Nm; however, the QH-mode was initiated in these shots using large, counter-I_p torques in the range of –3 to –5 Nm. The focus of the present experiment was creation of the QH-mode at low NBI torque.

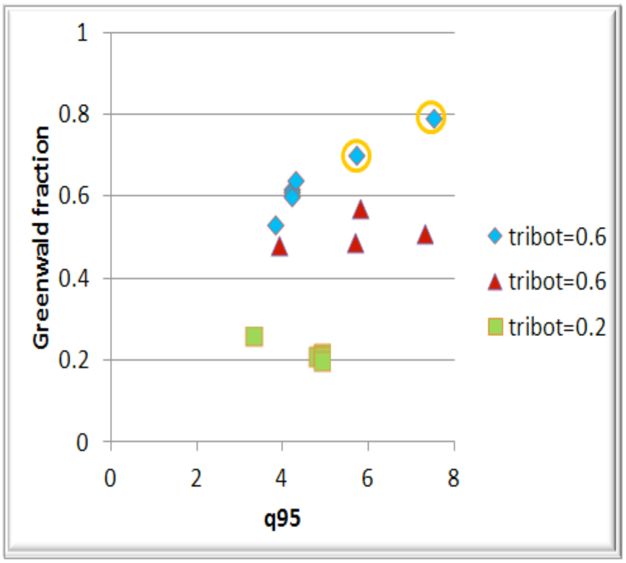

Fig. IV.3.3-2. Greenwald density fraction achieved during QH-mode operation as functions of q_{95} for three plasma triangularity values. Higher shaping allows higher density limit.

Experiments over the past three years have demonstrated that the NTV torque from non-axisymmetric magnetic fields with toroidal mode number n=3 can be used to sustain QH-mode plasmas even when the NBI torque is in the range of 0 to 1.3 Nm (in the co-I_p direction) [9–11]. Several different I- and C-coil configurations were used in this work. Taking the best features of the various configurations, the optimum non-axisymmetric coil configuration uses the C-coil to generate n=3 fields and the I-coil for n=1 error field correction and some odd parity n=3 contribution.

Some experiments on low torque startup for QH-mode were carried out in the 2012 campaign. Several lessons were learned from these shots. First, simply replacing the counter-I_p beam program with an equivalent power waveform made up of balanced beams did not work; significant problems were seen with locked modes. The usual QH-mode NBI starts at 300 ms during the current ramp up phase of the discharge. We were able to establish an Ohmic current ramp phase, which satisfies the need to have no NBI torque during this part of the shot. This lesson forms the basis for the present experiment, which used Ohmic current ramp up. Second, even starting with balanced beams in current flattop, the plasma rotates in the co-I_p direction, possibly due to the intrinsic torque. Even with the slightly counter-I_p NBI torque (-0.2 Nm) later in shots like 149083, locked modes occurred as the initially co-I_p rotation slowed towards zero. Shots in the 149083 series were run with neoclassical tearing viscosity (NTV) torque initiated well after the L to H transition. Accordingly, the lesson is that we should turn on the coils providing the NTV torque prior to the L to H transition if possible. Third, there was insufficient time in the 2012 run after developing the Ohmic startup to find the lower density limit. Since QH-mode operates better at lower densities, we need to see how low the Ohmic target density can go. The challenge in the present experiment was to find techniques that allowed us to move the plasma from one stationary operating mode with zero NBI torque to another. The Ohmic plasma operates with no NBI torque and exhibits a core rotation which is typically counter-I_p (around –10 km/s) and a pedestal rotation which is co-I_p (around +10 km/s). The QH-mode with added NTV torque can operate with zero net NBI torque and with rotation which is basically counter everywhere (typically –30 km/s) except perhaps at the magnetic axis and at the separatrix. As the beam power turns on, two processes occur which push the plasma rotation in opposite directions. The intrinsic rotation is equivalent to a co-I_p torque while the NTV torque from the n=3 fields is a counter-I_p torque. Our previous experiments show that in the final, QH-mode stationary state at $\beta_N = 1.8$, the NTV torque is significantly larger. The issue for the present experiment was to find a way for the NTV torque to exceed the intrinsic torque during the dynamic phase after the L to H transition.

3.4.2 Results Contributing to JRT13 Goals

Several aspects of a low-torque startup scenario for QH-mode access in ITER were developed, but a complete scenario will require higher edge ion temperatures than achieved in the experiment this year. A first successful aspect of the scenario shown by this experiment was that there was no obvious effect of the non-resonant n=3 fields on the L to H transition. However, based on work with NTV torque over the past three years, a small torque initially when β_N was low was expected to change to a counter-I_p torque as β_N rose. Instead the torque due to the n=3 fields was about 1 Nm in the co-I_p

direction at 300 ms after the beams came on. The explanation may be that the pedestal temperatures in these plasmas were quite low compared to the ones run previously (<1 keV initially versus 3–5 keV). The neoclassical offset velocity might be so close to zero that the NTV torque was co- I_p for the rotation speeds of this experiment. If this was the case, a scenario will need to be created with higher pedestal ion temperature while still maintaining low torque conditions. This experiment was also successful in providing clear lessons to guide future experiments, including showing that: 1) loss of the IU90 portion of I-coil leads to more severe mode locking problems when the I-coil is used to do n=1 error field correction plus producing some n=3 field with 60 degree phasing, 2) possibly because of the low edge ion temperature, magnetic torque on the plasma from the n=3 fields was in the co-I_p direction during this experiment rather than the desired counter-I_p torque, and thus Ohmic operation into the I_p flat top accordingly resulted in no ITER compatible source of counter-I_p torque, 3) future low torque experiments will need to return to early NBI during the I_p ramp to obtain higher pedestal T_i, including possible investigate of the use of feedback controlled ECH during the current ramp to control the q-profile evolution and avoid locked modes.

3.5 Extension of VH-mode High Performance Pedestals to Stationary Operation Using RMP Fields

3.5.1 Goals and Background

The primary goal of this experiment was to reproduce as closely as possible the best VH-mode performance observed in DIII-D and then to apply 3D perturbation fields in order to control the density rise and to extend the duration of the mode or to avoid the termination event entirely. Previous attempts in 2005 focused on applying n=3 I-coil fields during the onset of the VH-mode in the ELM-free H-mode phase. Those experiments found that relatively small I-coil currents resulted in good density control during the early VH-mode phases but triggered fast growing n=1 and n=2 modes that terminated the discharges. The purpose of this experiment was to extend the duration of VH-modes using 3D magnetic perturbation fields in double null plasmas.

Confinement regimes that are devoid of ELMs and have core parameters exceeding those in ELMing H-modes are referred to as VH- and EP H-modes in DIII-D [12–15] and NSTX [16, 17] respectively. These modes have enhanced levels of stored energy, expanded pedestal widths, higher edge bootstrap currents, larger total noninductive current fractions, broader poloidal flow shear regions, reduced thermal diffusivities just inside the top of the pedestal and suppressed density fluctuations near the top of the pedestal compared to typical H-mode plasmas. Unfortunately, these modes are transient and therefore have no practical utility for fusion reactor applications unless techniques can be developed to avoid the uncontrolled increase in the plasma β and subsequent MHD events leading to the termination phase. While VH-modes and EP H-modes have significant similarities, there are differences in the dynamics leading up to the triggering and termination of these regimes as discussed in Ref. [17]. In VH-modes the energy confinement can reach values that exceed typical L-mode and H-mode confinement by a factor of 3.5 and 1.8 respectively with low radiative fractions and core impurity concentrations. Peak axial triple products ($n_DT_i\tau_E$) of 4 **Å**x10^{23} m^{-3}•eV•s [14] have been obtained in these plasmas.

In DIII-D the best VH-modes are obtained with low recycling wall conditions such as those following a boronization and a high-temperature bake of the vessel walls. In one of the best VH-mode discharges obtained in DIII-D, β_N reached ~3.2 shortly after P_{inj} is increased from ~2.5 MW to ~8 MW. The line average density continued to increase while β_N saturated and started to degrade. The lower divertor D_α recycling emission showed several strong bursts during the rising density phase followed by a series of ELM-like events that appeared to be involved in the termination of the VH-mode. This dropped the discharge into an ELM-free phase with several sporadic ELMs followed by a final ELM-free or reduced β_N VH-mode.

In NSTX, the onset dynamics and evolution of the EP H-mode differ significantly from those in DIII-D VH-modes. Here, the beam power is ramped up to ~5.2 MW while the plasma current is being ramped up and then dropped to ~4 MW during the I_p plateau from t = 200 ms to the end of the discharge. Initially, the discharge is relatively ELM-free and the line average density as well as the global stored energy (W_{MHD}) and the thermal energy confinement time (τ_E) rise continuously until ~430 ms in the discharge when they roll over and trigger a large ELM-like event. Subsequently the EP H-mode is triggered following a second large ELM-like event at ~550 ms, which initially causes a loss in the stored energy and density to a lesser extent. During the EP H-mode there is a significant increase in the stored energy and confinement time while the density increases slowly relative to the other confinement parameters. The termination phase seems to result from a slow reduction of τ_E that ends with a strong D_α burst.

3.5.2 Results Contributing to JRT13 Goals

The goals of this experiment to produce high-quality VH-modes and improve their diagnosis, were successful, with several good examples of VH-modes produced (based on their high confinement and β_N; a second transition to VH-mode wasn't obvious, and detailed profile analysis needs to be done to confirm), and fluctuation measurements taken with FIR, BES, and DBS. Several attempts were made to control the VH-mode with n=3 fields, with the perturbation initiated during the L-mode phase, during the ELM-free phase before VH, and during the VH-mode itself. None of these showed an extended duration of the VH-mode, however, and instead it appeared that the 3D fields hastened the onset of ELMs a bit during VH-mode. Further, density pump-out was not observed during the ELM-free phase, possibly due to the relatively high collisionality and q_{95} of these plasmas.

Data from this experiment is being used to: 1) Evaluate the effects of 3D fields on the pedestal plasma profiles and stability during VH-modes including effects on kinetic profiles (T_e and T_i), ω_E, rotation profiles and edge fluctuations, 2) Compare the characteristics of VH-modes and termination events in DIII-D with those of enhanced pedestal (EP) H-modes in NSTX, and 3) Provide data for 3D two-fluid, extended MHD and full-f kinetic transport codes as well as for 3D stellerator-symmetic equilibrium codes. The measurements are being supplemented by an analysis of the stability properties of the edge plasma. This is partially motivated by the recent progress in understanding ELM suppression via RMP application, and if successful will guide later experiments on NSTX-U and DIII-D aiming to control and extend the duration of the EP H-mode and VH-mode.

3.6 Exploring Requirements for RMP ELM Suppression on DIII-D with Less Than 12 I-coils

3.6.1 Goals and Background

The purpose of this experiment was to obtain Type-I ELM suppression in low density low collisionality ITER-similar shape H-mode plasmas with reduced (<12) set of I-coils. The key questions to be addressed included: 1) Obtain ELM suppression with reduced number of I-coils and determine the I-coil current amplitude needed for ELM suppression, 2) Determine the minimum number of I-coils needed for ELM suppression to provide guidance to ITER for ELM control coil malfunctions, 3) Determine the effect of error field correction on ELM suppression with reduced number of I-coils, and, 4) Demonstrate recovery of ELM suppression after coil malfunctions. These are very critical questions for ITER ELM Control Coils design.

Our previous simulations [18] showed that an application of n=3 or n=4 toroidal perturbation in the ITER ELM coils will be able to produce a stochastic layer in the pedestal region of similar or greater width than in DIII-D. Vacuum island overlap width (VIOW) parameter [19] in these simulations exceeded 16.5% of radial width in normalized poloidal flux coordinates. According to our previous findings [20], this width of the pedestal stochastic region is typically correlated with the suppression of large Type I ELM in DIII-D. It was also adapted by ITER as a design criterion for ITER ELM coils

Recently, we have performed extensive numerical simulations to assess the performance of the ITER ELM coils in case of individual coil malfunctions. The vacuum simulation predict that ITER ELM coils as currently designed will be able to exceed the DIII-D ELM suppression criterion even with malfunctions of eight midplane ELM coils if coil currents are adjusted in the other coils [19]. This experiment was designed to test these model predictions by applying RMP ELM suppression fields to the same DIII-D plasma using 12, 11, 10, 9 etc. of the available I-coils on DIII-D.

3.6.2 Results Contributing to JRT13 Goals

The new results from this experiment suggest that the coil currents required for ELM suppression were no greater with the reduced coil sets than is typically required for the full set. An example of ELM suppression with 11 I-coils (black) and with 10 I-coils (red) is shown in Fig. IV.3.6-1. In these discharges ELMs are suppressed in the case with 10 I-coils earlier in the phase with coil current of 3 kA than in the case with 11 I-coils. This counter-intuitive result could provide an important validation of recent modeling [18,19] of the physical mechanisms involved. This modeling shows that the spectral sidebands introduced by deactivating individual coils can often increase the magnetic stochasticity within the plasma, thereby increasing transport and facilitating ELM suppression. Deactivating individual coils results not only in the reduction of the dominant n=3 component of the perturbation field, but also in a significant increase in the amplitudes of n=1 and n=2 sidebands. These sidebands may also be amplified by the plasma response. Application to ITER finds that the ITER ELM coils may be able to tolerate a loss of up to five of its 27 coils, while leaving a sufficient margin of current in the remaining coils to still meet the DIII-D ELM suppression criterion. Further, the new experiments show that the presence of the spectral sidebands does not adversely affect the plasma rotation or confinement. As these experiments and additional ones using 9, 8, 7, and 5 I-coils were completed only a few days before the end of the JRT13 period, analysis with both vacuum and two-fluid modeling is still underway to interpret and understand these data. Results will be presented in an APS post-deadline invited talk and in several planned publications.

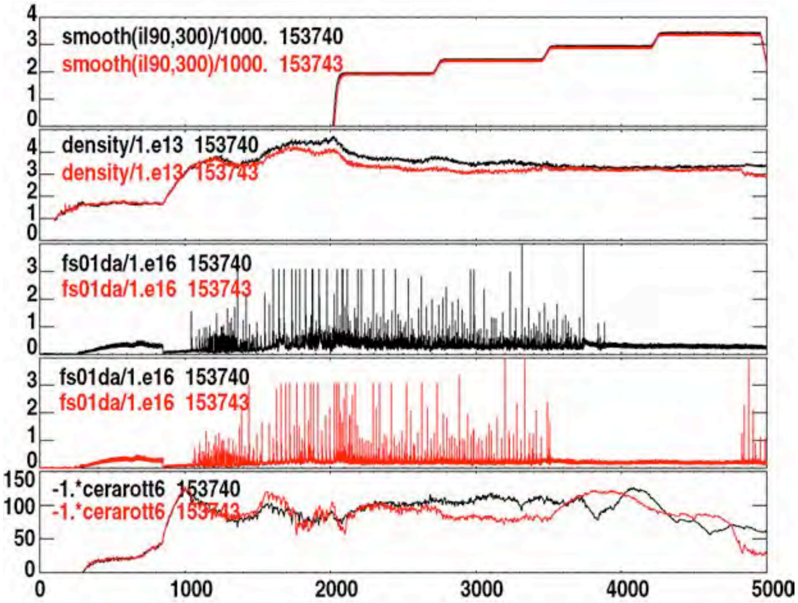

Fig. IV.3.6-1. Time history of I-coil current, density (line average and pedestal), inner divertor D_α emission and pedestal rotation for RMP ELM suppression discharges with 11 and 10 I-coils.

3.7 Conclusions

The experiments and analysis focused on testing the physics limits to operating regimes for several stationary H-mode regimes without ELMs succeeded in finding control parameters that allowed expansion of the operating spaces. For QH-mode a high degree of shaping allowed higher density operation and sustained high fusion performance was obtained with a moderate input torque. For RMP ELM suppression optimization of the I-coil current allowed suppression with reduced number of I-coils. In I-mode operation lower plasma current allowed operation to higher pedestal temperature due to reduced sawteeth amplitude. The common feature of these results may be the effect of the actuator on preventing the expansion of the pedestal pressure (either width of height) to the ELM instability boundary. But clearly difference remain in the detailed physics that accomplishes this pedestal control: in QH-mode it is done by an internally generated mode the EHO, in the RMP case the control comes by way of externally applied 3D fields, and for the I-mode it appears to be necessary to control the power flow through the pedestal to stay in I-mode and avoid the H-mode transition.

4.0 Paths for Future Exploration

4.1 Experiments and Analysis Focused on Particle Transport Physics Mechanisms

4.1.1 Future Experiments

Progress has been made during the JRT13 work toward understanding the physics mechanisms controlling edge particle transport in stationary regimes without ELMs, but complete understanding of the fundamental issue of how ELMs are prevented in these regimes (e.g. by the EHO, or the external application of 3D fields, or by other internal plasma modes) will likely require additional experiments. Results from the JRT13 work indicate that two new techniques used in the DIII-D experiment this year, vis.: 1) short puffs of CF4 with CER tuned to fluorine lines and, 2) the monitoring of the plasma response to modulated ECH beams, show promise for providing data to validate models of the physics mechanisms driving edge particle transport in stationary H-mode regimes without Type-I ELMs. These two techniques, combined with comprehensive fluctuations and turbulence diagnostics, could be applied in future experiments at all three facilities to investigate the edge particle transport mechanisms in I-mode, QH-mode, RMP ELM control, EP H-mode and other ELM control regimes.

4.1.2 Analysis

Given that many of the experiments addressing the JRT13 goal of increasing understanding of the physics mechanisms driving edge particle transport were executed less than a few months before the end of the JRT13 period, considerable analysis is still ongoing. Significant modeling of the impurity transport in the QH-mode experiments with the CF4 puffs needs to be done. The data from injection of modulated ECH into a plasma with strong RMP fields is being analyzed with techniques pioneered by our colleagues at LHD in Japan. Finally investigations into the connections between variations in edge turbulence and fluctuations measurements, and changes in the edge transport (e.g. through the pedestal density) are underway especially for the I-mode operation, but also for all the stationary regimes without ELMs, and will continue well after the JRT13 period.

4.2 Experiments and Analysis Focused on Testing Physics Limits to Operating Regimes

4.2.1 Future Experiments

Results from the DIII-D experiments during JRT13 that were focused on extending the operating regimes of various stationary regimes without ELMs showed that future experiments need to target specific aspects of the regimes. These are summarized below organized by operating mode.

To further extend the QH-mode operational space to low torque startup, a scenario must be developed that maintains high edge pedestal ion temperature during the early plasma current ramp-up phase so that the NTV torque will be strongly counter-I_p and provide sufficient edge rotation shear to access QH-mode with low torque input. Ideas to achieve this include application of NB heating very early in the discharge and possible use of ECH under feedback control during the current ramp to affect the current profile evolution and avoid early locked modes. To further extend QH-mode to high fusion performance at low input torque (β_N*H_{89}/q_{95}^2=0.4 at 0 – 1 Nm input torque), techniques for improved error field correction must be developed to overcome the tendency of these scenarios toward locked modes as q_{95} is reduced for maximization of the fusion performance metric G=β_N*H_{89}/q_{95}^2. Resistive wall mode (RWM) feedback techniques are a good candidate for this improved error field correction. Also higher density may help to increase G by allowing low q_{95} operation without locked modes, providing the confinement factor H_{89} does not decrease as much as the gains in going to low q_{95}. The experiments this year did show that it should be possible to obtain QH-mode at ITER relevant densities and Greenwald fractions, but further experiments which attempt to maintain QH-mode operation at these very high density conditions for many energy confinement times are still needed.

To extend the I-mode operating space in DIII-D requires that sawteeth energy pulsed through the edge pedestal be reduced or eliminated. I-mode operation is close enough to ELMing H-mode in DIII-D that sawteeth heat pulses passing through candidate I-mode temperature pedestals frequently trigger a transition into the H-mode. There was evidence for a correlation between smaller sawteeth heat pulses in candidate discharges at lower plasma current and higher T_e pedestals in I-mode-like conditions having no evidence of a density pedestal. Various techniques are effective for reducing the size of sawteeth including central ion cyclotron resonance frequency (ICRF) power and off-axis current drive or counter NB injection to keep the central safety factor above 1.0. In DIII-D the actuators for off-axis current drive include off-axis neutral beam current drive (NBCD) using the tilted beamlines, and electron cyclotron current drive (ECCD) tuned to off-axis deposition.

Future experiments to extend the performance of RMP ELM suppression to fewer I-coils will need to concentrate on understanding the effects of n=1 and n=2 sidebands in the applied mode spectrum when additional I-coils are turned off. The working hypothesis of ELM suppression with some I-coils missing is that n=1 and n=2 sidebands help to fill in gaps in the spectrum of perturbation fields in the plasma and thereby prevent the growth of the width of the pedestal to the ELM instability boundary. Clearly this mechanism must breakdown as the number of coils continues to be reduced and the resonant n=3 components of the spectrum become smaller. The clear path to optimization of the combined n=1, n=2 and n=3 spectrum will not be able to be developed until the physics mechanisms controlling the edge particle transport and the growth of the pedestal width during RMP application are understood.

4.2.2 Ongoing Analysis

The primary tool of ongoing analysis for the experiments extending the operating regimes is pedestal stability calculations with the ELITE and EPED code packages. For the DIII-D I-mode candidates, the density/Greenwald fraction limit QH-modes and the RMP ELM suppression cases with less than 12 I-coils, the analysis will start with kinetic EFITS which are used by ELITE to determine how close the pedestal operating point is to the ballooning, peeling-ballooning or kink-peeling stability boundaries. Analysis with EPED will then determine how close the pedestal pressure width and height are from the intersection of the peeling-ballooning and kinetic ballooning stability boundaries. Similar analysis is ongoing for C-Mod I-mode cases and plasmas in EP H-mode in NSTX, to compare with the DIII-D results. These tests of the proximity of the pedestal operating points to various instability boundaries will give information on the direction to push the pedestal in order to increase its performance without triggering ELMs.

Acknowledgment

This work was supported by the US Department of Energy under DE-AC52-07NA27344, DE-AC02-09CH11466, DE-FG02-04ER54698, DE-AC05-00OR22725, DE-FG02-04ER54762, and DE-FG02-05EAR54809.

References

[1] T.E. Evans *et al*., Nature of Physics **2**, 419 (2006).
[2] P.B. Snyder *et al*., Phys. Plasmas **19**, 056115 (2012).
[3] N.M. Ferraro, Phys. Plasmas **19**, 056105 (2012).
[4] K. Ida, *et al*., Phys. Rev. Lett. **100** 045003 (2008).

[5] K. Ida *et al.*, New J. Phys. **15** 013061 (2013).
[6] O. Schmitz, Personal Communication (2012).
[7] T.H. Osborne, et al., *Scaling of ELM and H-mode pedestal characteristics in ITER shape discharges in the DIII-D tokamak*, Proceedings of the 24th EPS Conference on Controlled Fusion and Plasma Physics, June 9–13, 1997, Berchtesgaden, Germany, General Atomics report GA-A22638, July 1997.
[8] A.M. Garofalo, Nucl. Fusion **51**, 083018 (2011).
[9] K.H. Burrell *et al.*, Phys. Plasmas **19**, 056117 (2012).
[10] A.M. Garofalo *et al.*, "High Beta, High Confinement, Stationary ELM-free Operation at Low Plasma Rotation," Proceedings of 39th European Physical Society Conference On Plasma Physics, Stockholm, Sweden, (2012), http://ocs.ciemat.es/epsicpp2012pap/pdf/O2.102.pdf.
[11] K.H. Burrell *et al.*, “Quiescent H-mode Operation Using Torque from Non-axisymmetic, Non-resonant Magnetic Fields,” Nucl. Fusion **53** (to be published)
[12] G.L. Jackson *et al.*, Phys. Rev. Lett. **67**, 30981 (1991).
[13] S.I. Lippmann, *et al.*, J. Nucl. Mater. **196-198**, 498 (1992).
[14] T.H. Osborne *et al.*, Nucl. Fusion **35**, 23 (1995).
[15] T.E. Evans, *et al.*, J. Nucl. Mater. **220-222**, 235 (1995).
[16] R. Maingi *et al.*, J. Nucl. Mater. **390–391**, 440 (2009).
[17] R. Maingi et al., Phys. Rev. Lett. **105**, 135004 (2010).
[18] D.M. Orlov, *et al.*, Fusion Eng. Design **87**, 1536 (2012.
[19] T.E. Evans, *et al.*, Nucl. Fusion **53**, 093029 (2013).
[20] M.E. Fenstermacher, *et al.*, Phys. Plasmas **15**, 056122 (2008)

Chapter 5
NSTX-U Contributions to the FY2013 Joint Research Target

S.P. Gerhardt[1], R Maingi[1], D. Battaglia[1], R.E. Bell[1], J.M. Canik[2], N. Crocker[3], A. Diallo[1], R. Goldston[1], S. Kubota[3], B.P. LeBlanc[1], S. Parker[4], Y. Ren[1], F. Scotti[1], D.R. Smith[5], P. Snyder[6], K. Tritz[7], W. Wan[4]

[1]Princeton Plasma Physics Laboratory, Plainsboro, NJ, USA
[2]Oak Ridge National Laboratory, Oak Ridge, TN, USA
[3]Department of Physics and Astronomy, University of California, Los Angeles, USA
[4]Department of Physics, University of Colorado, Boulder, USA
[5]Department of Engineering Physics, University of Wisconsin-Madison, USA
[6]General Atomics, San Diego, CA, USA
[7]Department of Physics and Astronomy, Johns Hopkins University, Baltimore, MD, USA

1.0 Overview

1.1: The need for stationary confinement regimes without large ELMs

The H-mode confinement regime is characterized by a strong thermal and particle transport barrier at the plasma edge, known as the H-mode pedestal. The excellent thermal confinement is beneficial for fusion systems, but the excellent particle transport can result in unacceptable impurity accumulation. This transport barrier is often interrupted in periodic MHD events knows as Edge Localized Modes (ELMs). ELMs have the beneficial result of flushing impurities from the plasma core, enabling stationary conditions. However, the impulsive thermal loading due to natural ELMs will severely limit the divertor lifetime in next step devices such as ITER.

In order to address this apparent conflict for ITER, a number of approaches are under consideration [1]. One approach is to trigger ELMs much more rapidly than their natural rate, which should reduce the magnitude of the impulsive heat flux. The primary ELM pacing techniques for ITER are likely to be pellet pacing [1,2-6] or triggering via “vertical jogs” [1,7-12]. These methods have been shown to reduce the impulsive heat fluxes while providing the required impurity transport. Alternatively, the application of resonant magnetic perturbations (RMP) has been shown to suppress ELMs in DIII-D [1,13-15]; the physics of RMP is still under active investigation, but may be related to some mechanism that limits the radial expansion of the H-mode pedestal [16].

In addition to these regimes of active ELM control, there is considerable interest in plasma regimes where intrinsic fluctuations replace ELMs for particle control, with minimal impulsive heat flux. Examples of these regimes include the Quiescent H-mode (QH-mode), discovered and optimized in DIII-D [17-21] and since duplicated in JET [22], JT-60 [23,24] and ASDEX-Upgrade [22,25] or the I-mode, first observed in ASDEX-Upgrade [26] and systematically explored and exploited in Alcator C-Mod [27-31]. In the case QH-mode, the intrinsic fluctuations are known as the Edge Harmonic Oscillations (EHO), and are believed to be saturated peeling instabilities. In the I-mode, the intrinsic fluctuations are referred to as the Weakly Coherent Mode (WCM). These regimes, with levels of thermal confinement comparable or exceeding that in H-mode, acceptable particle transport facilitating stationary conditions, and no large ELMs, are a primary subject of the 2013 FES Joint Research Target.

1.2: The 2013 FES Joint Research Target

Given the critical issues described in the previous section, the 2013 FES Joint Research Target (JRT) has been formulated. The goals of this research are described in the annual target and the 4th quarter milestone descriptions:

Annual Target:

Conduct experiments and analysis on major fusion facilities, to evaluate stationary enhanced confinement regimes without large Edge Localized Modes (ELMs), and to improve understanding of the underlying physical mechanisms that allow acceptable *edge particle transport while maintaining a strong thermal transport barrier. Mechanisms to be investigated can include intrinsic continuous edge plasma modes and externally applied 3D fields. Candidate regimes and techniques have been pioneered by each of the three major US facilities (C-Mod, D3D and NSTX). Coordinated experiments, measurements, and analysis will be carried out to assess and understand the operational space for the regimes. Exploiting the complementary parameters and tools of the devices, joint teams will aim to more closely approach key dimensionless parameters of ITER, and to identify correlations between edge fluctuations and transport. The role of rotation will be investigated. The research will strengthen the basis for extrapolation of stationary regimes which combine high energy confinement with good particle and impurity control, to ITER and other future fusion facilities for which avoidance of large ELMs is a critical issue.*

4th Quarter Milestone:

Complete the required experiments and analysis. Prepare a joint report summarizing the contributions toward the development high-performance stationary regimes devoid of large ELMs, and identifying important paths for future exploration.

This document fulfills the NSTX-U portion of the 4th quarter milestone, and represents the NSTX-U contribution to the 2013 JRT.

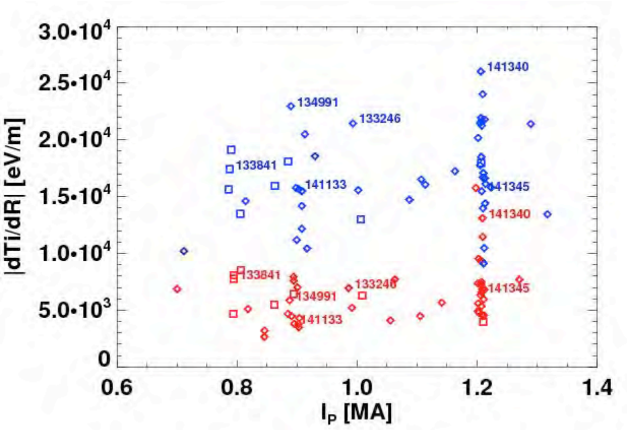

Fig. 5.1: Inverse ion temperature scale length for EP H-mode (blue) and H-mode (red) examples in NSTX.

1.3: NSTX-U contributions to the 2013 Joint Research Target

NSTX did not have regimes that strictly satisfy these goals of the JRT; the density typically ramps in essentially all NSTX discharges. Hence, the NSTX-U contribution addresses sub-components of the JRT goals:

- Section 2.0 addresses the Enhanced Pedestal H-mode (EP H-mode) [32-33]. This regime shows a separation between particle and thermal transport, similar to other regimes of interest for the JRT, and may be a candidate for high-performance operation in NSTX-U and next-step STs. Pedestal dynamics, transport, and fluctuations in this regime are discussed, as are issues associated with controlling access to the EP H-mode configuration.
- Section 3.0 discusses ELM-free regimes produced via lithium PFC conditioning [34]. This section describes both the impurity dynamics [35] and the fluctuation scaling [36] in these regimes.

- Section 4.0 describes the observations of edge harmonic oscillations in NSTX [37,38] These oscillations are similar to those observed during QH-mode operation in DIII-D, though they do not contribute to particle transport in any meaningful way, apparently due to their low amplitude. The structure of these modes in NSTX is discussed, using data from reflectometers and beam emission spectroscopy. Methods to potentially drive these oscillations to large amplitude in NSTX-U are discussed.

2.0 Enhanced Pedestal H-mode Research

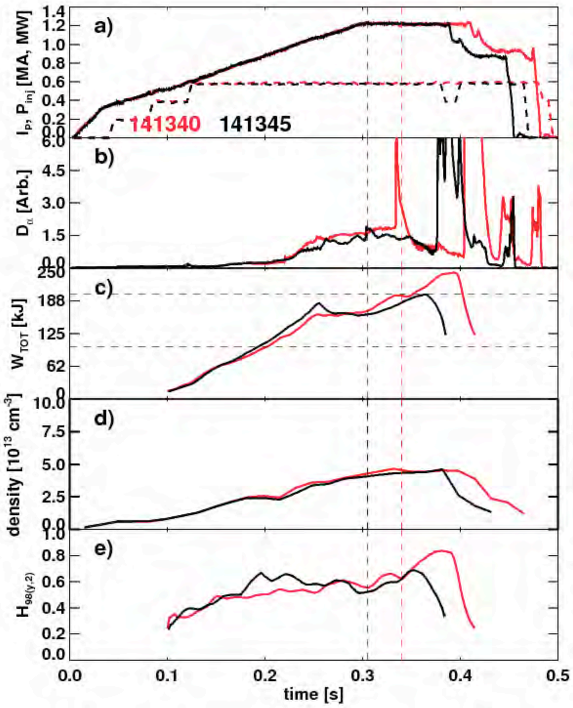

Fig. 5.2: Time evolution of short-lived EP H-mode example discharges. Shown are a) the plasma current and beam power, b) the divertor D_α emission, c) the stored energy, d) the line averaged density, and e) the confinement multiplier $H_{98(y,2)}$.

As noted in section 1, the Enhance Pedestal H-mode [32,33] is a potentially attractive confinement regime for next step-ST plasmas. It is defined by the following characteristics:

- There is a discreet transition to this confinement regime, with this transition always following the L->H transition. This transition is often, but not always, triggered by an ELM.

- There is a region in the plasma edge with very sharp ion temperature gradients. This is illustrated in Fig. 5.1, where the normalized ion temperature gradient is shown as a function of plasma current for the H-mode and EP H-mode phases for a large database of discharges. The gradients in the EP H-mode phases are typically a factor of 3 larger than those in the H-mode phase.

- There is a localized region of large rotation shear in the plasma edge, in the vicinity of the steep ion temperature gradient. There is often, but not always, a local minima in the rotation.

2.1: General EP H-mode Characteristics

2.1.1: Early EP H-mode Transition Examples

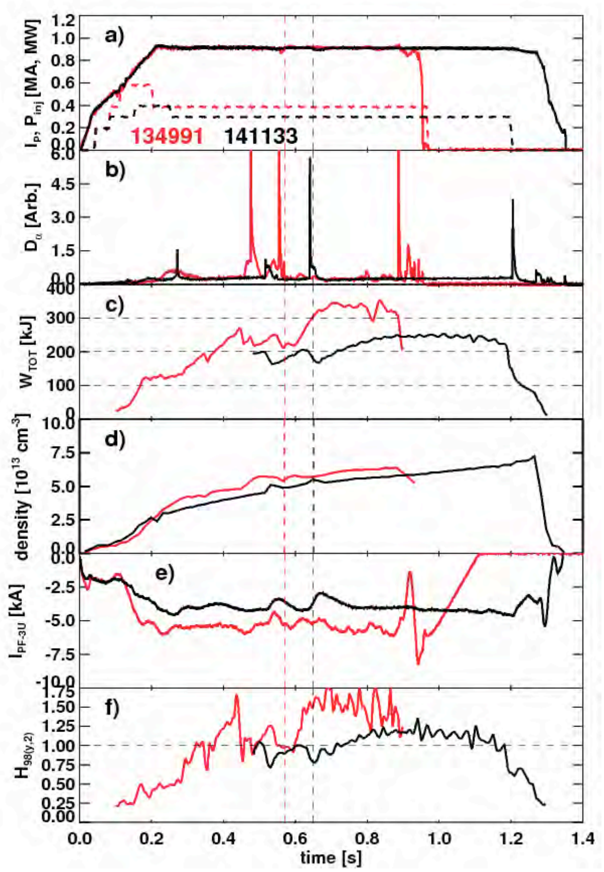

Fig. 5.3: Time evolution of long-pulse EP H-mode example discharges. Shown are a) the plasma current, b) the divertor D_a emission, c) the stored energy, d) the line-average density, e) the current in the radial field coil, and f) the $H_{98(y,2)}$ confinement multiplier.

The first EP H-mode examples in NSTX [32] were typically rather short lived, with durations of less than 100 ms. In these cases, the transition to EP H-mode typically occurred either during the current ramp or early in the flat-top phase. Recent examples of the time evolution of these cases can be found in Fig. 5.2, for a pair of I_P=1.2 MA discharges; these discharges were made during the 2010 run campaign in order to study EP H-mode plasmas. In both cases, the H-mode transition occurs at t=0.215 s, as indicated by the sharp change in slope of the density evolution. In 141340, the EP H-mode transition occurs following a large ELM, as has often been observed. However, in 141345, no large ELM is observed, demonstrating that these regimes can be initiated without an ELM. There is a strong ramp in the stored energy, indicating the improved confinement. The confinement multiplier $H_{98(y,2)}$ also shows a ramp at this time, though the discharge disrupts before the confinement can reach a high level. There is a small ramp in the line-average density during this phase. These short pulse examples indicate the potential benefits of the regime, motivating the search for other examples.

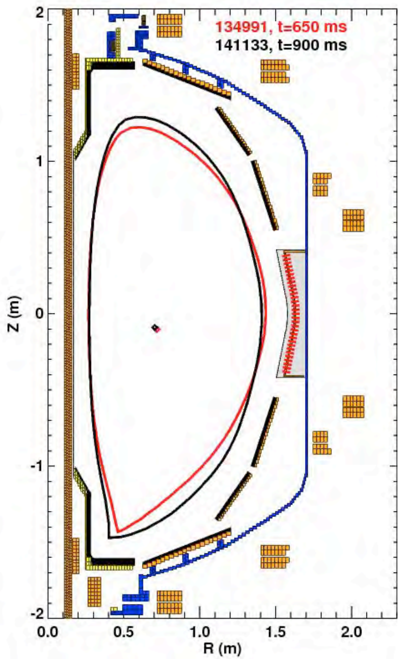

Fig. 5.4: Typical separatrix shapes for the long-pulse EP H-mode examples.

2.1.2: Long-Pulse EP H-Mode Examples

More recently, long-pulse EP H-mode examples have been observed. The Fig. 5.3 shows examples of these cases including discharge 134991 in red discussed in Ref. [33] and the newly observed discharge 134333. As indicated in frame a), both are I_P=900 kA discharges, heated by either 3 or 4 MW of neutral beam injection. The vertical lines indicate the time of transition to EP H-mode, which follows an ELM is both cases. There are large increments in stored energy following the transition, and both examples show a plateau in the stored energy for many confinement times. Indeed, while 134991 eventually suffers a disruption, potentially associated with the q=1 surface entering the plasma, discharge 141133 maintains a high confinement state for the duration of the heating power application. The discharge 134991 achieves very high $H_{98(y,2)}$ factors of ~1.5, while 141133 has the still impressive $H_{98(y,2)}$ factor of 1.2. Unfortunately, the density does increase during the EP H-mode phase of these discharges.

The boundary shapes for these two examples are shown in Fig. 5.4. Discharge 134991 is a moderate triangularity discharge δ_l=0.63 , while discharge 141133 has a high value of triangularity δ_l=0.8. More importantly, the EP H-mode phase of 141133 is extremely quiescent compared to other H-mode discharges. This is visible in the stored energy trace, or in the PF-3U coil current in Fig. 5.3. This coil controls both the elongation and vertical position of the plasma via feedback loops. The steady nature of that coil current indicates the lack of transients in the discharge, a characteristic highly desirable for next step configurations.

2.1.3: Typical Profile Shapes and Evolution

As part of the 2013 JRT analysis, a small code was written to identify discharges with very steep gradients in the ion temperature, with the expectation that this would identify additional EP H-mode examples. This was indeed the case, with the number of identified EP H-mode discharge increasing by many factors. More interestingly, this exercise revealed that there is a large range of T_i profile shapes that may be considered within the bounds of the enhanced pedestal H-mode. Examples of these profile shapes are illustrated in Fig. 5.5. Note that these discharges occurred on different experimental run days, and only discharge 141340 was executed with the intention of studying EP H-modes.

In this figure, the top row shows the electron and on temperatures, along with both tanh fits to T_i and a line tangent to the point of the maximum T_i gradient. The tanh fit is defined via the function:

$$Y(X) = Y_{offset} + \frac{\left(Y_{pedestal} - Y_{offset}\right)\left(1 + 0.5\alpha_{slope} z\right)}{1 + e^{-2z}},$$

with $z=2(X_{symmetry}-X)/\Delta_{width}$ [39]. Here, Y can represent T_e, T_i, n_e or any other profile quantity, while X can represent either outboard midplane major radius or some flux surface label such as normalized poloidal flux. Y_{offset}, $Y_{pedestal}$, α_{slope}, $X_{symmetry}$, and Δ_{width} are fit parameters determined by a non-linear fitting routine.

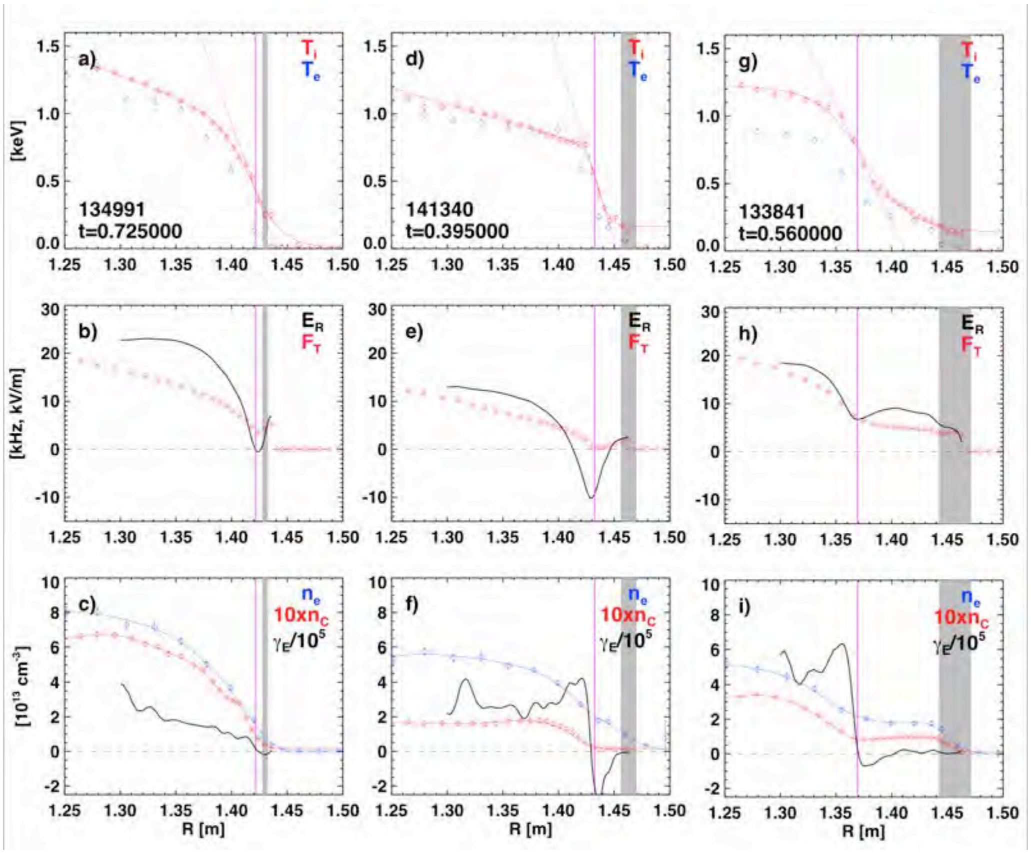

Fig. 5.5: Examples of profile shapes during EP H-mode in NSTX. The top frame of each column shows the ion and electron temperature profiles. The points show the data, while the lines show tanh fits, the magenta line marks the location of maximum ion temperature gradient and the tangent line to the profile at that point. The middle frames show the toroidal rotation and radial electric field profiles (computed neglecting the poloidal rotation), while the bottom frames show the electron and carbon density, as well as the ExB shearing rate. The grey shaded regions indicate the approximate regions of the separatrix.

The second row shows the toroidal rotation profile, as well as the E_R profile evaluated from the measured carbon parameters as $E_R = \frac{1}{6eN_C}\frac{dP_C}{dR} + V_T B_P$. The poloidal rotation, which is generally small in NSTX [40], is neglected in this calculation; this assumption must be validated in future research evaluating the poloidal rotation in this region. The radial electric field so calculated is then used to calculate the ExB shearing rate in the bottom frames, as [41] $\gamma_E = \frac{r}{q}\frac{d}{dr}\frac{E_R}{RB_P}$. The bottom row also shows the electron and scaled carbon density profiles, along with spline fits to those profiles. The separatrix location is shown as the gray shaded region, determined by the values give by equilibrium reconstruction, the T_e=40 eV location, and the T_e=80 eV location.

The left-most column of Fig. 5.5 shows the edge profiles for the long-pulse EP H-mode discharge 134991, whose time evolution is illustrated in Fig. 5.3. In this case, the region of steep T_i gradient is very close to the plasma edge. There is a clear minima in the rotation profile, with a deep E_R well developing. The profiles for the other long-pulse discharge in Fig. 5.3 (141133) are of similar shape, and will be illustrated below.

The middle column of Fig. 5.5 shows the profiles for a case typical of the short-lived EP H-modes that transition before or just after the start of the I_P flat-top; see Fig. 5.2 for the time evolution of 0D quantities in this case. In this example, the region with the steepest T_i gradient is shifted in a few cm, with a clear region of lower T_i gradient farther outside. However, the clear rotation profile minima and E_R well are still present.

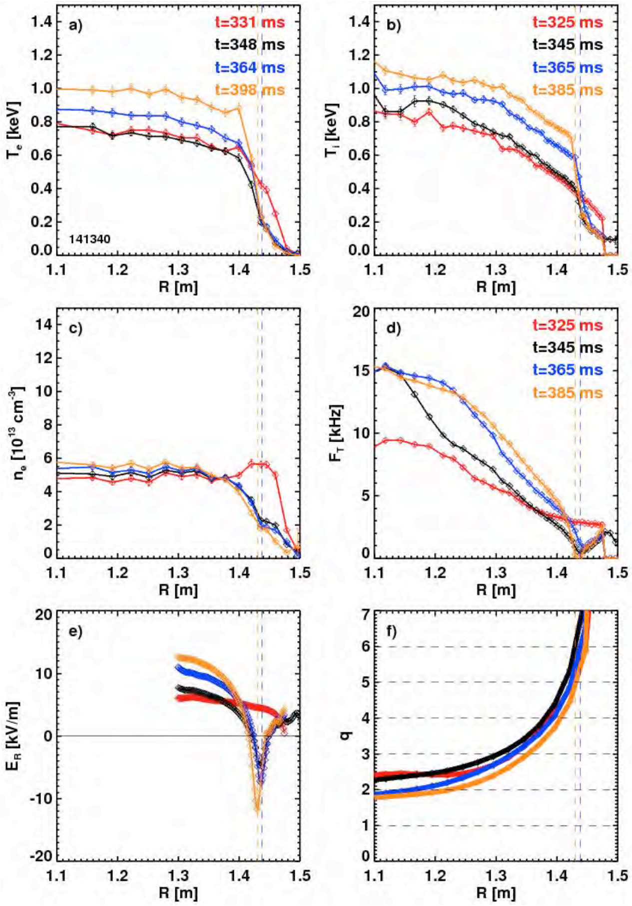

Fix. 5.6: Time evolution of the profiles from EP H-mode discharge 141340, snap-shots from which are shown in the center column of Fig. 5.5. Shown are profiles of the a) the electron temperature, b) the ion temperature, c) the electron density, d) the toroidal rotation, e) the radial electric field, and f) the safety factor.

Finally, the right most column shows a case where the steep T_i gradient is shifted inward ~10 cm from the plasma edge. There is an associated inward shift of the region of sharp rotation gradient indicating that the relationship between the steep ion temperature gradient and rotation is maintained. In this case, both T_e and n_e show a double-barrier structure, and the configuration could be called a wide radius internal transport barrier (ITB) or an EP H-mode. For this reason, cases such as in the right column of Fig. 5.5 will be noted with a square in the scatter plots below, whereas cases such as in the left and center column will be denoted with a diamond.

The profile evolution for the example in the center column of Fig. 5.5 is shown in Fig. 5.6; this is the high-current example transitioning to EP H-mode early in the discharge. The CHERS data (F_T, T_i, E_R) and MPTS data (T_e, n_e) are on slightly different time bases, so nearly synchronous samples are indicated with the same color. At t=330ms, the configuration is in H-mode, with broad density, temperature and rotation profiles. The edge T_i pedestal is not resolved by the CHERS diagnostic, and so the E_R features at the edge are not fully resolved.

After t=330 ms, the EP H-mode transition occurs following a large ELM, with a number of associated changes in the profiles. The electron density and temperature at the plasma edge are reduced, and the rotation immediately develops a local minima. The ion temperature at the very edge is also transiently reduced, though the core ion temperature is largely unchanged; this results in a region of sharp T_i gradient at the location where the two regions connect. These rotation and pedestal dynamics result in the formation of a deep well in the E_R profile.

From that point onward, the minima in the rotation remains, marked by vertical dashed lines in the figure for the later time slices. The width of the ion temperature pedestal increases at roughly fixed gradient scale length until the EP H-mode phase ends with a disruption. Note the double hump structure in the density, barely visible in the bottom, center frame of Fig. 5.5, but clearly visible in Fig. 5.6c).

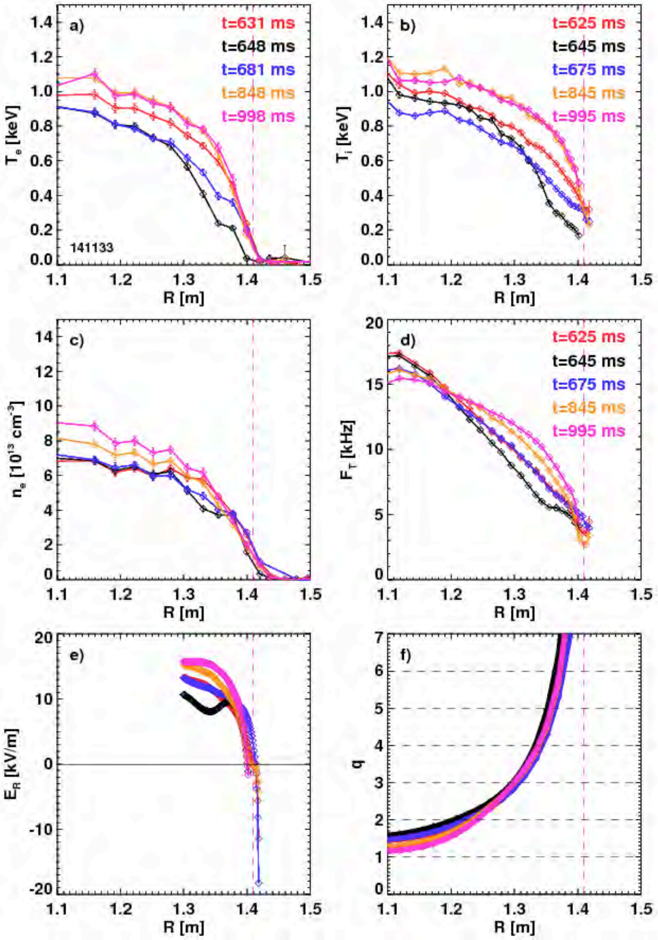

Fig. 5.7: Profile evolution for the long pulse EP H-mode discharge 141133. The frames are the same as in Fig. 5.6.

It has been speculated that the minima in the rotation profile is associated with a single rational surface [Maingi 2010]. However, as illustrated in Fig.5.6f), isolating which surface would play this role has proven difficult. This figure shows the q profile at the time of interest, with the vertical lines indicating where a rational surface might be anticipated. The minima in the rotation appears to not be located at the q=2, 3, or 4 surfaces. It may be located at one of the q>4 surfaces, though isolating which one is essentially not possible due to the large magnetic shear.

Fig. 5.7 shows the profile evolution for the recently discovered long-pulse EP H-mode discharge 141133. This case does not have as steep an ion temperature gradient at the discharge in Fig. 5.6. However, as shown in Fig. 5.1, the edge T_i gradient is still well above the levels of typical H-mode plasmas.

As observed in the previous example, the ELM that triggers the EP H-mode transition results in a drop in the edge ion temperature, while leaving the core value unchanged (compare black and red curves). The ion temperature then recovers, ultimately developing a very steep profile at the plasma edge. The rotation profile shows hints of a local minima at the edge for some time slices. However, the CHERS diagnostic is unable to reliably make measurements towards the bottom of the pedestal, and so it is difficult to assess if this feature is constant in time.

Finally, Fig. 5.8 shows the profile evolution for a discharge with the region of steepest ion temperature gradient shifted inwards. This is a discharge with triggered ELMs [42-44]; there are a number of small ELMs in the vicinity of the transition to the EP H-mode line state, although it is difficult to identify which, if any, play a role in triggering the transition. In any case, the transition is again initiated by a drop in the edge ion temperature, resulting in a region of steep T_i gradient. The width of the region then grows at roughly fixed gradient.

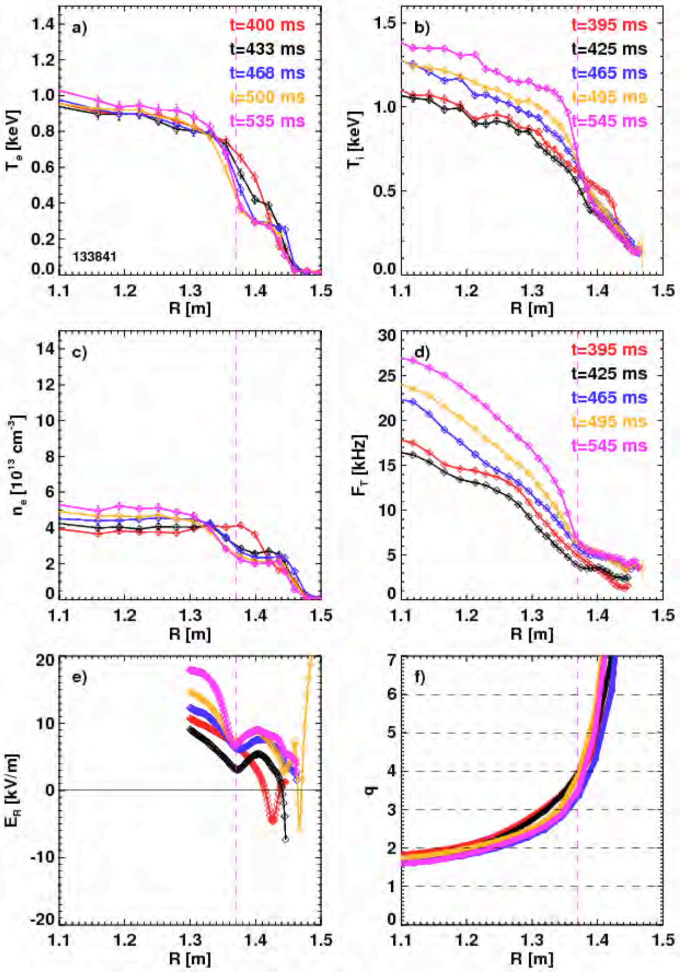

Fig. 5.8: Profile evolution for the EP H-mode example 133841, where the region of steep T_i gradient is shifted inward. The frames are the same as in Fig. 5.6, though the scales differ.

The unique dynamics of this configuration also manifest themselves in the other profiles. The electron density and temperature begins to develop a double-barrier shape immediately following the transition, and this shape is maintained throughout the EP H-mode like phase. The toroidal rotation profile in the H-mode phase is fairly broad, and shows a rapid drop at the EP H-mode transition. The rotation gradient then builds rapidly, staying aligned with the region of steep T_i gradient. Note that the H-mode profiles have a strong E_R well, but the EP H-mode like profiles show significant E_R shear developing well inside the plasma.

Figures 5.5-5.8 also make important points with regard to 1) potential 3D variations and 2) rotation profile shapes.

With regard to potential 3D perturbations to the equilibria, it is noted at that there is often a substantial radial distance (2-5cm) between the regions of steep T_e and T_i gradients; this can be easily observed from comparing frames a) and b) of Fig. 5.6 and 5.7, using the vertical lines as guides. Given that the T_e and T_i profiles are measured with diagnostics whose toroidal separation is 180°, this might imply that there are significant 3D distortions to the plasma. This separation is typically not observed in H-mode plasmas, indicating that it is not related to diagnostic spatial calibration issues. Further suspicion may arise from comparisons of the q-profile, derived from intrinsically axisymmetric solutions to the Grad-Shafranov equation, with the toroidally localized CHERS measurements: the locations of minima appear to be in very high shear regions, and not in the vicinity of the low-n resonant surfaces initially considered important for this damping. However, there are a number of observations that point away from a 3D solution:

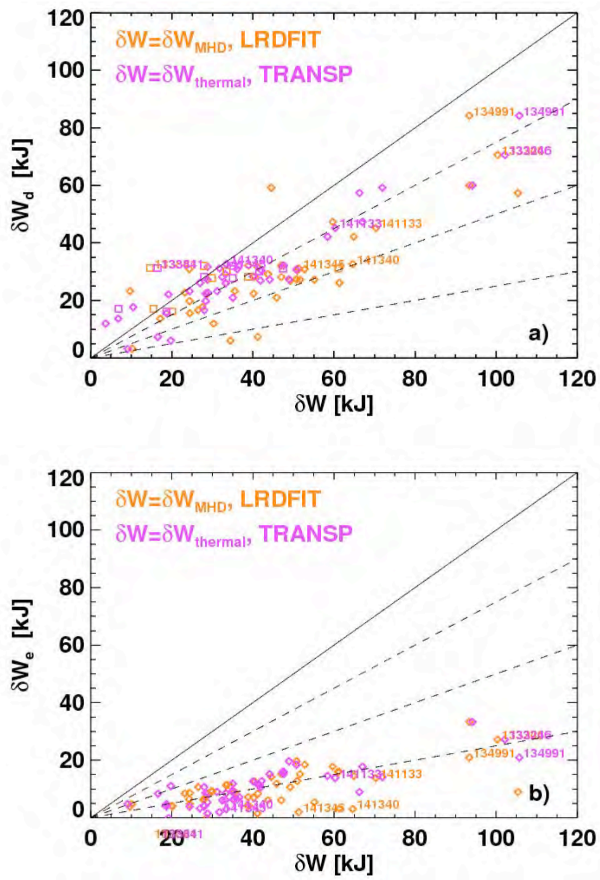

Fig 5.9: Increments of the deuterium (top) and electron (bottom) stored energy, as a function of the total stored energy increment δW. The orange points are based on calculating δW from equilibrium reconstruction, while the magenta points are based on extracting δW from TRANSP runs. Shot numbers are indicated for certain discharges discussed in this report.

- The χ^2 measure of goodness of fit from axisymmetric equilibrium codes such as EFIT or LRDFIT is not higher in EP H-mode than standard H-mode.
- The apparent shift between the T_e and T_i pedestals is present for cases where the local velocity minimum goes to zero, or is finite at a few kHz
- The relative position of the T_e and T_i pedestals is the same for both polarities of the OH current and for various phases of the n=3 applied field. The error field due to the OHxTF interaction was the dominant n=1 error field in NSTX [45], and changed sign as the OH current changed sign. Hence, one might expect the toroidal phase of the apparent 3D distortion to shift with the shift of the applied field. Alternatively, if the 3D disruptions manifest themselves at higher toroidal mode number, then they might change phase with the n=3 field phase.

Hence, the present study will use purely axisymmetric analysis techniques, while acknowledging that this may obscure some important 3D effects.

With regard to rotation profiles, it should be noted that the profiles in Fig. 5.5b) or Fig. 5.7d) are among the most broad in observed in NSTX, a feature which is quite stabilizing to low-n global MHD. This may help explain why discharge 134991 sustains β_N>6, albeit with some degree of global activity, while discharge 141133 is nearly quiescent at β_N~5. On the other hand, the profiles in Fig 5.8 would be less desirable from the global stability perspective, as they are too peaked. The favorable profiles, which tend to manifest themselves in the later-transition long-pulse EP H-mode examples, provide clear motivation for pursuing the EP H-mode regime for next-step ST development. However, the examples also show that it is necessary to learn how to optimize and control the EP H-mode profile shapes, in order to fully exploit the configuration.

2.1.4: Stored Energy Increments During EP H-mode

A large database of EP H-mode discharges has been compiled; the results of this database are included in the figures in Sect. 1 of this report. That database assembles quantities measured just before the H-mode to EP H-mode transition, and then at a time when the EP H-mode has fully developed. The database uses quantities from both TRANSP [46] and the equilibrium codes EFIT [47-49] and LRDFIT [50]. The database also includes pedestal parameters extracted from the tanh fits to the edge profiles, using the functional form described in Section 2.1.3. Both the NSTX Thomson Scattering [51] and toroidal CHERS diagnostics [52] are oriented horizontally at the vessel midplane, allowing measurements of quantities with respect to the outboard major radius without any additional mapping step. Hence, the tanh fits utilized here are typically constructed as a function of major radius.

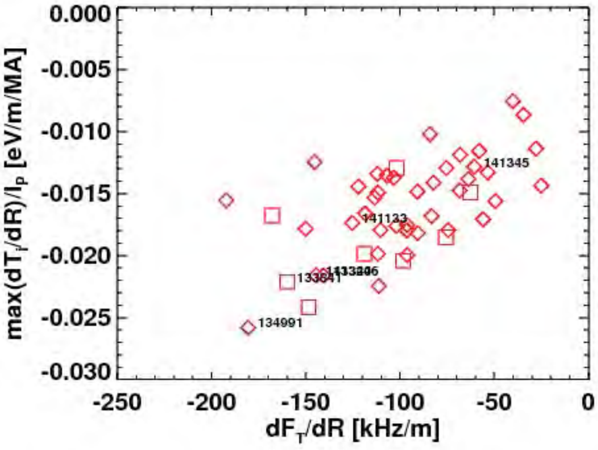

Fig. 5.10: The maximum ion temperature gradient, normalized to the plasma current. Diamonds are for EP H-mode configurations as in Fig. 5.5a) and b), and squares are for configurations as Fig. 5.5c)

The figures above show that there is a substantial increase in the stored energy following the EP H-mode transition. An important question to assess is which kinetic species was responsible for this energy increment. Fig. 5.9 shows the electron and deuterium energy increments as a function of the total energy increment. The electron and deuterium energy increments are determined from integrating the thermal pressure of those species using TRANSP. The total energy increment is determined from either MHD equilibrium reconstruction (orange) or from the total thermal energy increment computed by TRANSP. This figure shows clearly that the primary increment of energy occurs in the ion channel, with ~75% of the energy increase appearing in the deuterium. Approximately 25% of the energy increase is typically found in the electrons, with negligible increases in the impurity and fast ion energy. Note that these ratios are typical of both cases with the T_i steep-gradient region shifted inward from the separatrix (squares), and cases where it is located nearer or at the edge (diamonds).

2.1.5: Relationship between Rotation and Ion Temperature Gradients

Previous analysis of a small set of EP H-mode cases indicated that the ion temperature pedestal height scaled roughly with toroidal rotation shear at that same location. As part of the present research, this relationship was examined for a larger number of examples. The results of this study are shown in Fig. 5.10.

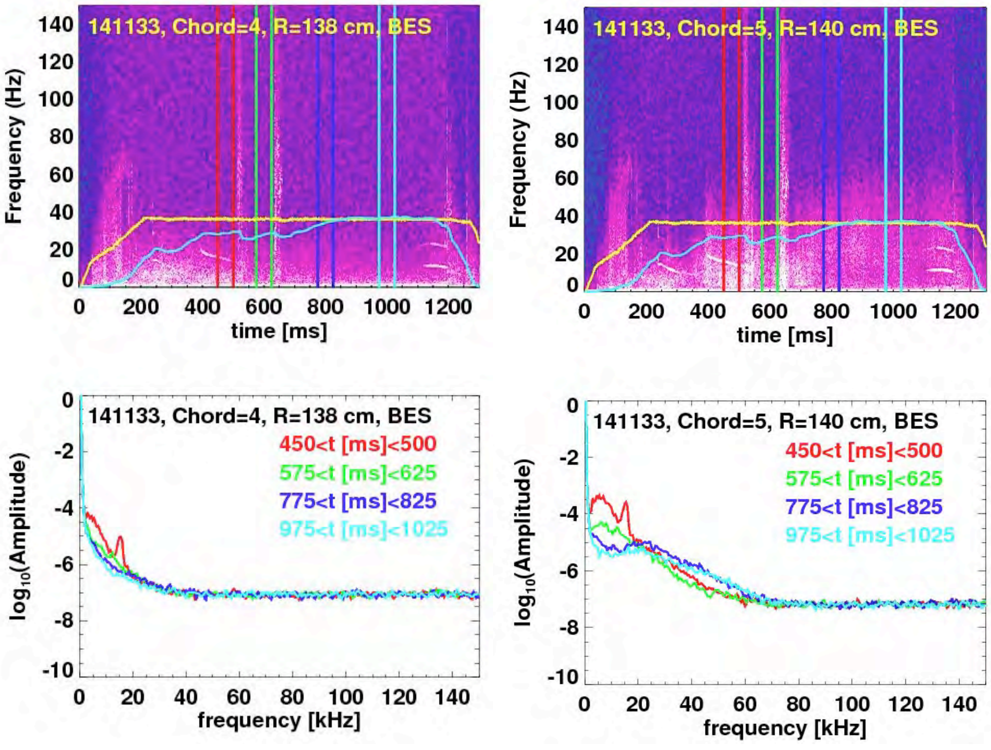

Fig. 5.11: BES fluctuation spectrum data for long-pulse EP H-mode discharge 141133. The upper frame shows the spectrogram, along with the plasma current in yellow and the normalized β in cyan. The lower frames show the average spectrum computed during the time between the vertical lines in the upper frame. The measurement locations of R=1.38 and 1.4 m are in the steep gradient region (see Fig. 5.7).

While the previous analysis used the pedestal height as a figure of merit, that proved problematic for the present case due to the inclusion of discharges such as in the right column of Fig. 5.5. These cases have a substantial “vertical” offset to the T_i profile due to the region with smaller gradient outside of the steep gradient region. Hence, for this analysis, the maximum value of dT_i/dR is used to parameterize the strength of the EP H-mode. Furthermore, it was found that the trends in the data were more clear if the gradient were scaled by the equilibrium plasma current. The x-axis in this plot shows the rotation gradient in the region inside of the local rotation minima. It is clear that, within the not insignificant scatter, the confinement as captured by this measure of the ion temperature gradient does indeed scale with the local rotation shear, for cases with the T_i gradient both near and farther from the separatrix.

2.2 Observation of Edge Fluctuations in EP H-Mode

A dedicated effort has gone into examining the edge turbulence during the EP H-mode phase of these discharges. Fluctuations under consideration have included magnetic fluctuations as assessed by edge Mirnov coils and density fluctuations as assessed by both the FIReTIP interferometer and the Beam Emission Spectroscopy (BES) system [53,54].

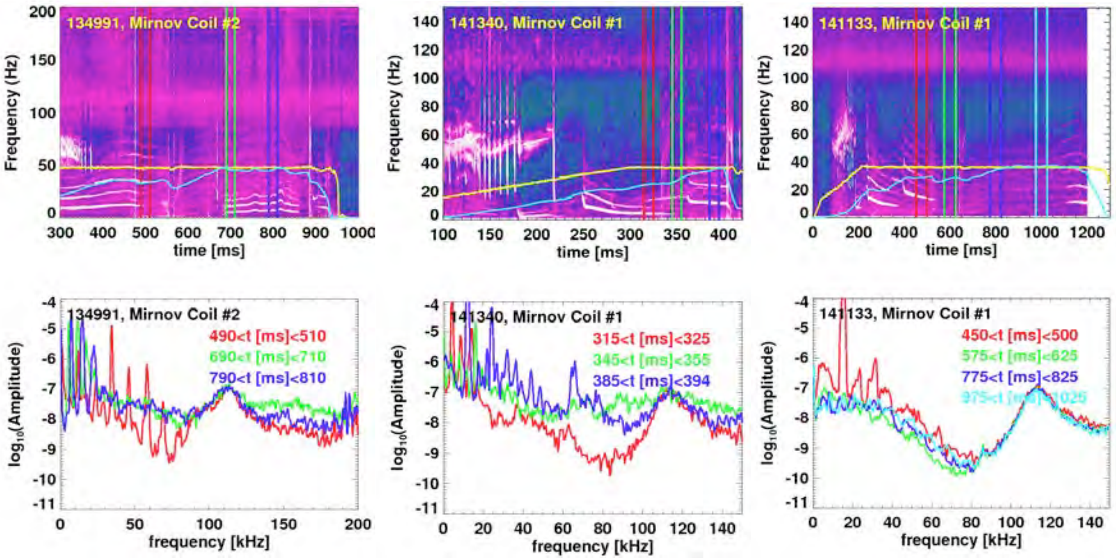

Fig. 5.12: Spectrograms of edge magnetic fluctuations in three EP H-mode examples. The EP H-mode phases are indicated in green and blue on the left, green and blue in the center, and blue and cyan on the right.

Example fluctuation data from the BES diagnostic is shown in Fig 5.11, for the long pulse EP H-mode case 141133. The top frame shows a spectrogram of the data, while the frame shows four spectra; the times used in computing the four spectra are bound by the vertical lines in the upper frame. The radii of the measurements, R= 1.38 &

1.40 m, are directly in the pedestal region of interest, as can be seen in Fig. 5.7. The first two time slices (red and green curves) correspond to the H-mode phase of these discharges. These are generally featureless, except for a 15 kHz mode in the earlier frame (these modes are common in the early phases of NSTX discharges [55]). The two later times are during the initial and later EP H-mode phase of this discharge. Interestingly, there is no observable reduction in the measured turbulence during this phase. Indeed, if anything, there may be a small increase in the fluctuation amplitude during the EP H-mode phase (though this may also be due to the larger density during this later phase). This result is generally typical of the BES measurements during EP H-mode, where clear reductions in turbulent amplitude have been difficult to identify. Similar results were found when examining the line-averaged density fluctuation amplitudes from the FIReTIP diagnostic.

While the results of the BES and FIReTIP fluctuation analysis were disappointing, there may be signatures of the relevant physics in the edge magnetics signals, as analyzed in Fig. 5.12. The left and center columns correspond the discharges illustrated in Fig. 5.5. In both these two cases, there are clear increases in the level of magnetic fluctuations between 50 and 100 kHz during the EP H-mode phase, compared to the preceding H-mode phase. For 134991 (left column, long-pulse, high-β example), there are a series of low-frequency modes, which have been identified as n=2-4 modes from phase analysis. These fluctuations are not by any means ubiquitous to EP H-mode plasmas, and the more significant effect may be the broadband fluctuation increase. Discharge 141340 (center column, early EP H-mode transition example from Fig. 5.6) shows the standard low-f mode activity that occurs as the current profile evolved in NSTX [55]. However, the increased magnetic fluctuation amplitudes are also observable following the EP H-mode transition at t=0.33 s.

However, while these magnetic fluctuation observations are encouraging, is must be noted that these observations are not ubiquitous . For instance, discharge 141133 (left column, quiescent long-pulse EP H-mode example), does not show any particular increase in magnetic fluctuation amplitude. Hence, while these magnetic fluctuations may play some role in the EP H-mode physics, other elements must be at play as well.

2.3 Calculations of turbulence and transport in EP H-mode Mode plasmas

2.3.1: Assessment of thermal transport with XGC-0

XGC0 [56] is a code that leverages high-performance computing to calculate the self-consistent full-f drift-kinetic solution for ion transport in the H-mode pedestal using a realistic diverted magnetic geometry and Monte Carlo neutral recycling model. The large computational resources required to solve the full-f solution is justified on the observation that kinetic ion effects (such as ion orbit loss and finite orbit effects) have significant impacts on the ion thermal, particle and momentum transport in the H-mode pedestal and scrape-off layer.

The code was recently updated to enable quantitative comparison to experimental measurements in order to quantify the role of axisymmetric neoclassical transport in various H-mode transport regimes. These updates include: (1) addition of impurity ions to the simulation since most ion diagnostics measure the properties of plasma impurities, (2) synthetic diagnostics for typical profile diagnostics on NSTX and DIII-D, such as charge-exchange spectroscopy and Thomson scattering, and (3) improved code diagnostics that track the contributions of different transport processes on the energy, particle and momentum balance.

The ability to quantitatively compare the simulation to experimental measurements has enabled XGC0 to be used as an interpretative transport model. Ad-hoc anomalous transport is added to the neoclassical transport level if it is needed to improve the agreement between the simulation and experimental measurements.

Interpretative XGC0 was used to investigate the neoclassical ion transport in an EP H-mode discharge with transport approaching saturation (discharge 141133, discussed in Fig 9.7, at 900ms).

The neoclassical thermal transport calculated by XGC0 is found to reasonably reproduce the levels seen in experiment throughout the simulated pedestal and SOL domain ($0.6 < \psi_N < 1.1$). However, the neoclassical momentum transport rate inside of $\psi_N < 0.9$ is under-predicted. The requirement of anomalous momentum transport may be an indication that non-ambipolar electron transport (such as fluctuation-induced Reynolds and Maxwell stress) is a significant source of momentum transport in NSTX.

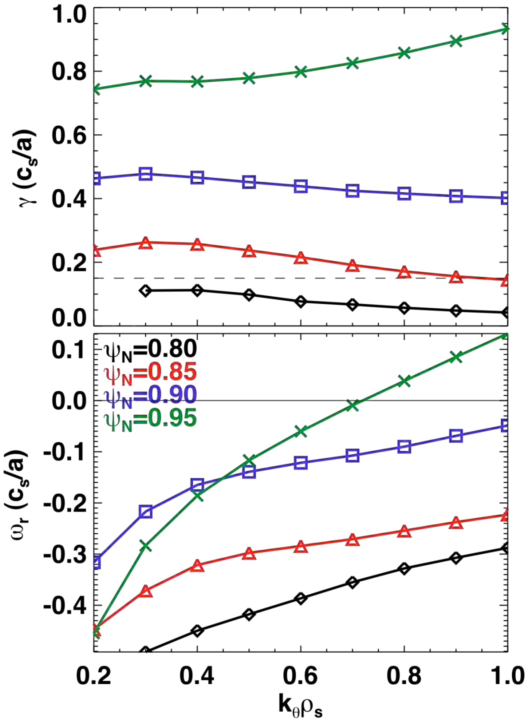

Fig. 5.13: Spectra of the growth rate (top) and real frequency for TEM-like modes in the EP H-mode pedestal. The different colors correspond to different radial locations.

The simulation also indicated that the neoclassical particle transport was sufficient to reproduce the experimentally measured density profiles with realistic neutral-beam and recycling particle sources. However, this result was achieved using an enhanced electron mass that was 1% of deuterium (as opposed to 0.028%), so the dependence of the simulated neoclassical particle transport on the mass of the electron needs further investigation.

The XGC0 simulation results suggest that EP H-mode achieves a level of ion thermal and particle transport that approaches the neoclassical limit throughout the pedestal and SOL. However, the ion neoclassical transport is influenced by the details of the turbulent electron transport through collisional coupling and anomalous momentum transport. Thus, the transition from H-mode to EP H-mode may represent a bifurcation in the electron transport that self-consistently modifies the ion neoclassical transport. This hypothesis will be investigated in the future by comparing the neoclassical ion transport in EP H-mode conditions to standard H-mode scenarios on NSTX using interpretative XGC0 analysis.

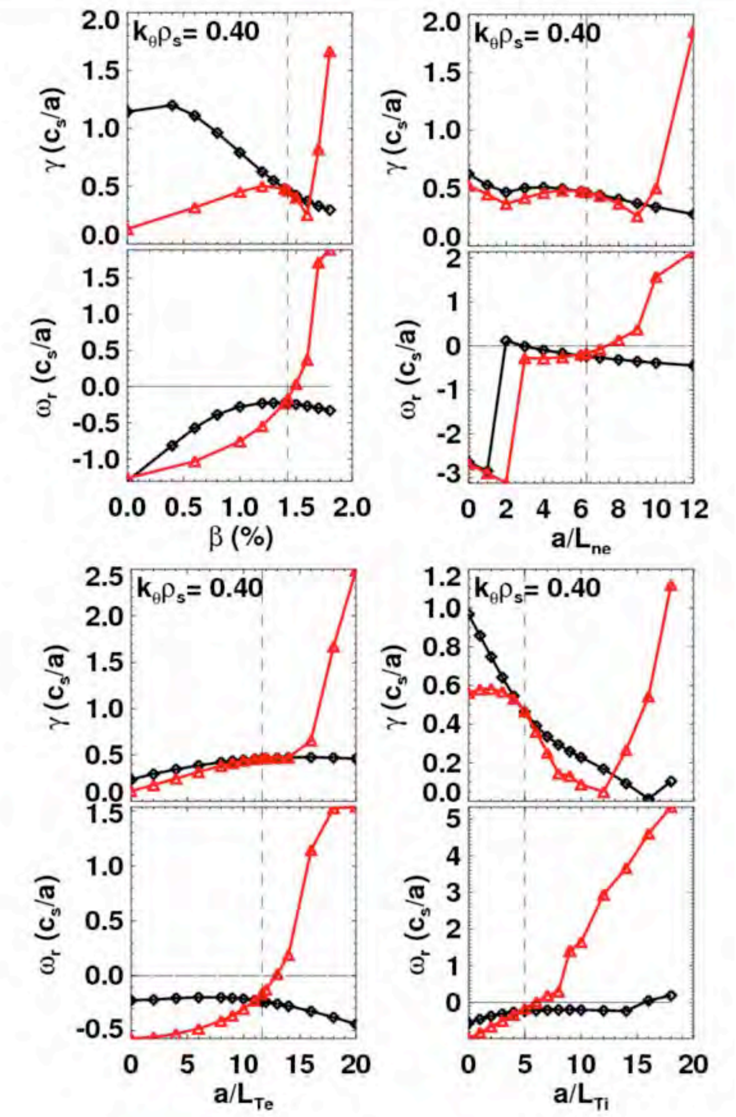

Fig. 5.14: Growth rate and real frequency of the dominant instabilities in the example EP H pedestal, as a function of upper left) β, upper right) the density gradient, lower left) the electron temperature gradient, and lower right) the ion temperature gradient

2.3.2: Assessment of microstability with GS2

The gyrokinetic stability of an EP H-mode discharge is being analyzed using the GS2 code [57]. Kinetically constrained MHD equilibria are used in these calculations, along with the fitted edge profiles used to generate these reconstructions. Three kinetic species are included—deuterium and carbon ions along with electrons—and the simulations are fully electromagnetic and include pitch-angle scattering collisions. Initial efforts focused on grid resolution checks at several edge radii to ensure the solutions are converged. Spectra of the growth rate and real frequency are shown in Figure 5.13 for four edge radii roughly spanning the EP H-mode pedestal. The real frequency along with eigenfunction structure (not shown) indicate that TEM-like modes are dominant throughout the pedestal, with the exception of a mode propagating in the ion diamagnetic direction at higher k_y at the outermost radii. The growth rates increase with radius, and over much of the pedestal are significantly larger than the ExB shear rate (indicated by the dashed horizontal line). At radii further in than shown here (ψ_N=0.7 and 0.75), modes in the wavenumber range considered are stable.

The scaling of the frequency with various parameters such as gradient scale lengths and β have been calculated for a radius of ψ_N=0.90 (roughly at the mid-pedestal). These scans have been performed two ways: 1) by varying gradient scale lengths only, while leaving the magnetic geometry fixed, and 2) by using a local MHD equilibrium model to change the pressure gradient within the magnetic geometry and keep it consistent with the (varying) parameters during scans. This is an important difference, since increasing the pressure gradient in the MHD equilibrium tends to be strongly stabilizing, and can partially or even fully offset the destabilizing effect of increasing (for example) the temperature gradient. In Fig. 5.14, results using the first method (single parameters varied individually) are shown as the red curves, while those using the second method (geometry recalculated using a pressure gradient consistent with the other parameters at each point in a scan) are shown in black.

As the figure shows, if the geometry is held fixed, increasing any one of β, the density gradient, or the electron and ion temperature gradients by less than a factor of two causes a kinetic ballooning mode to become destabilized (as evidenced by a sharp increase in the growth rate and a strongly positive real frequency). However, with a consistent MHD equilibrium calculated at each point, KBM onset is never observed. This is consistent with the plasma being in the second-stable regime, which has been verified through calculations of ideal ballooning stability. At the nominal parameters (vertical dashed line), increasing the electron temperature gradient has the strongest destabilizing effect. The density gradient is weakly stabilizing, with microtearing modes appearing at very low values of a/L_{ne} (evidenced by the transition to large magnitude negative real frequency). Increasing the ion temperature gradient is strongly stabilizing, regardless of how the geometry is treated (aside from the transition to KBM). This suggests that the increased ion temperature gradient measured in the EP H-mode does not lead to degraded microstability, and may be consistent with the dominance of neoclassical transport in the ion channel. Overall, the dependencies found here are reasonably consistent with the dominant mode being a TEM/KBM hybrid mode as found in pedestal calculations during standard and lithiated H-modes [58], with a smooth transition between negative and positive real frequency as the KBM threshold is approached (in the case where the geometry is held fixed). One difference, however, is the β dependence found here, where increasing β is stabilizing near the nominal value even in the case where the geometry is not changed.

2.3 Prospects for EP H-mode Utilization in NSTX-U and next step STs.

One criterion for extrapolating the EP H-mode for next-step devices is the demonstration of quasi-stationary conditions for many energy confinement times. This has been shown in Fig. 5.3. A second criterion is to establish a mechanism to trigger and control the transition to this regime.

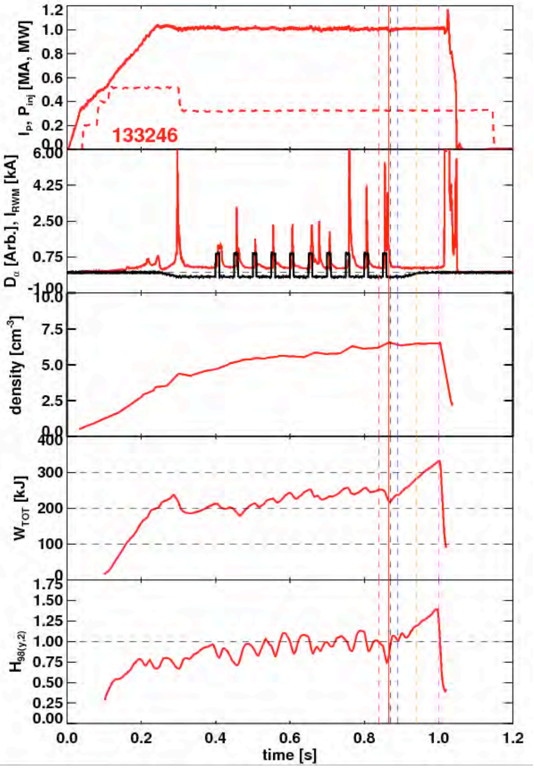

Fig. 5.15: Example of EP H-mode configuration initiated by a triggered ELM. Shown are the plasma current and injected power, D_α and RWM coil current, line-averaged density, stored energy, and $H_{98(y,2)}$ confinement multiplier. The dashed vertical lines indicated the times of the profiles in Fig. 5.16.

Given that a spontaneous ELM is often observed to trigger this regime, it seems reasonable to examine whether an externally triggered ELM can have a similar effect. As shown in Fig. 5.15, this is indeed the case. The top frame shows the plasma current (I_P=1 MA in flat-top) and beam power for this discharge. The second frame shows the current in a representative RWM coil in black and a D_α trace in red. It can be seen that there are small transients in the current, and that these trigger ELMs [42-44]. The RWM coil configuration in this case is configured to produce pulsed n=3 fields, which have shown to trigger ELMs over a range of conditions. In the present case, the transition to the EP H-mode configuration follows the final triggered ELM. The following frames show the line-averaged density, stored energy, and $H_{98(y,2)}$ confinement multiplier. In this case the density ramp is largely arrested, at least for the duration of this EP H-mode example, while the stored energy and confinement increase compared to the H-mode phase. Note that there are other examples of the externally triggered EP H-mode transitions, all of which come from the RWM ELM triggering experiments.

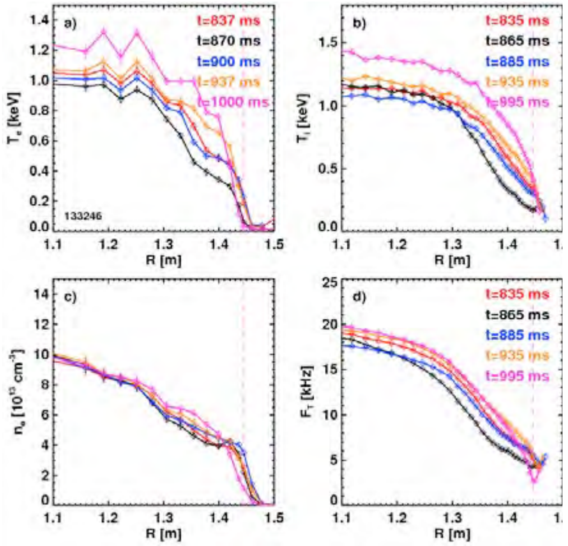

Fig. 5.16: Profile evolution following the ELM-triggered EP H-mode in Fig. 5.15

Fig. 5.16 shows the profiles before and during the EP H-mode phase of the discharge; the chosen colors match the vertical lines in Fig. 5.15, indicating the relative timing between the frames. The behavior for this externally triggered EP H-mode is similar to that in previous cases, with the ELM at t=0.865 s leading to a significant drop in both the edge ion temperature and rotation. The local minima in the rotation profile can be found for some time slices in the following EP H-mode phase. The region of steep T_i gradient is localized to the very edge of the CHERS measurement, and the rotation profile takes on broad structure. Hence, this triggered EP H-mode case shows all the features of the most attractive previously illustrated spontaneous transition examples.

Beyond initiating the EP H-mode configuration with triggered ELMs, it remains possible that specialized 3D fields at the plasma edge could trigger this configuration. It appears that the field configuration most likely to trigger these configurations will have fairly high-n, in order to minimize the core perturbation. It is conceivable that either resonant fields, which may lead to island opening, or non-resonant fields, which would brake the plasma rotation via the NTV effect, may be optimal for setting up the rotation profile required for the EP H-mode configuration. These options will be explored with the NCC coil in NSTX-U.

2.4 Future Research Directions for Enhanced Pedestal H-mode Research.

The research described above indicates key future directions for EP H-mode research. With regard to profile analysis, the poloidal flow should be included in the radial force balance analysis. This flow was not routinely measured in NSTX, and it may be that TRANSP/NCLASS calculations of the anticipated impurity flow will be necessary to compute the $V_\theta B_T$ term.

The XGC0 analysis will also warrant further work. Now that creditable calculations for this EP H-mode example have been completed, it will be valuable to compare them to standard H-mode case. This work is ongoing.

Experimentally, reliable access to the EP H-mode configuration is an important consideration. Once experiments are initiated on NSTX-U, triggering methods for the EP H-mode configuration will be revisited. These will include further efforts to sustain the naturally occurring EP H-mode configurations that often occur early in the discharge in high current cases, or to trigger EP H-mode configurations at lower q_{95}.

3.0 Physical Mechanisms Behind Transport in the ELM-Free H-mode Pedestal

Experiments in NSTX have shown that with the application of lithium conditioning to the PFC, ELMs are eliminated [34] and confinement improves [39,59]. While these are nominally positive changes, strong accumulation of impurities has been observed in these discharges [60], a characteristic that must be eliminated in order to achieve a stationary condition. In this section, recent research on the transport dynamics of these ELM-free H-modes is presented. The transport of lithium and carbon, including detailed comparisons to neoclassical theory, are presented in Section 3.1; note that some aspect of this study were reported in the FY-12 JRT report, but are repeated here due to their timeliness and relevance. New studies of pedestal microstability are presented in Section 3.2.

3.1: Assessing Impurity Transport in ELM-Free H-Mode

As has been documented in numerous publications and is noted in the introduction, lithium-conditioned discharges in NSTX have excellent confinement [59,60], few or no ELMs [34,61], well-controlled deuterium inventories [35], low levels of lithium contamination [62], and high levels of carbon accumulation [60]. This high level of carbon accumulation prevents these regimes from reaching stationary conditions, providing a significant barrier to extrapolating them to next-step STs.

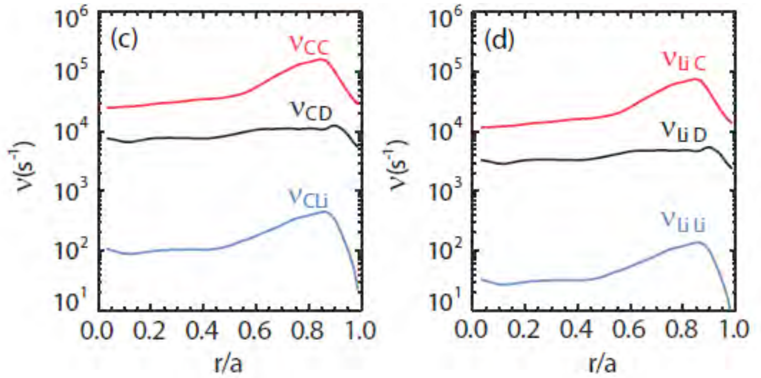

Fig. 5.17: Test particle collision frequencies for carbon (left) and lithium (right).

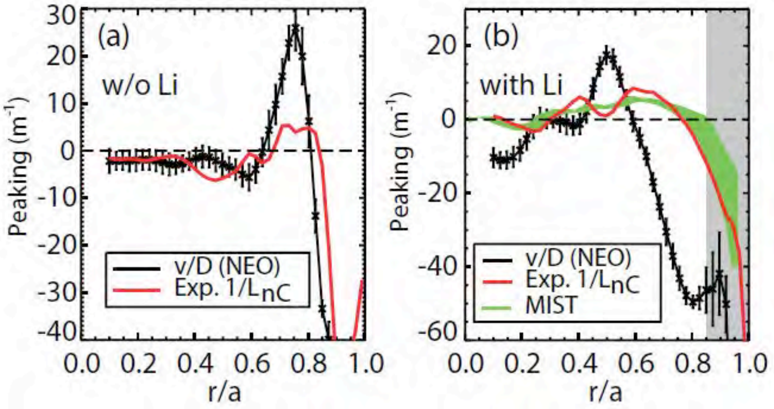

Fig. 5.18: Comparison of the experimental and neoclassically predicted peaking factors for carbon for a case without lithium PFC conditioning (left) and with lithium PFC conditioning (right)

Recent research has provided significant insight into the dynamics of lithium and carbon transport in these regimes [35,63.]. This research uses carbon and lithium profiles [67] from the CHERS diagnostics, and electron density and temperature data from Thomson scattering. The neoclassical transport of carbon and lithium is assessed with the NEO [64] and NCLASS [65] codes, which compute both a diffusivity D and a convective velocity υ. The MIST code was used, in either interpretative or fully predictive mode, to solve the impurity transport equations. Key results from that research are summarized here.

To develop some initial intuition about the dominant neoclassical impurity transport mechanisms, the various relevant collision frequencies were studied. As indicated in the left frame of Fig. 5.17, carbon collisions with background deuterium ions dominate the carbon transport (like-particle collisions do not generate particle transport). Indeed, a factor of 100 increase in the measured lithium concentrations would be required to meaningfully change the calculated carbon transport coefficients. Hence, modifications to the neoclassical carbon transport due to lithium PFC conditioning must be due to changes in the background deuterium parameters. The lithium neoclassical transport, on the other hand, is dominated by collisions with carbon impurities.

A first part of this study addressed carbon transport in discharges with and without lithium conditioning; the case without lithium PFC conditioning had medium sized type-I ELMs. The results from this study are summarized in Fig. 5.18, where profiles of the peaking factors are plotted. The experimental peaking factor of the profile quantity f(r) is denoted by $1/L_f = \frac{d}{dr}\ln(f)$, based on measured profiles. The predicted neoclassical peaking is, for a source free region, given by the ratio υ/D, where these quantities are both computed with NEO in the present example. Here, υ is the inward convective (pinch) velocity, while D is the diffusion coefficient.

For the case without lithium conditioning on the left, the predicted peaking agrees well with neoclassical predictions in the core (r/a<0.6) and in the edge (r/a>0.8). A significant discrepancy exists in the vicinity or 0.6<r/a<0.8, with the neoclassically predicted peaking being quite high. This local maxima is not found in the experimental results. This difference is likely due to the flushing of impurities in this radial region due to ELMs, an effect not captured in the present modeling.

For the lithium conditioned case, qualitative agreement is found between the neoclassical modeling and experimental result, including an outward convection region for 0.2<r/a<0.6 and an strong inward edge pinch. However, discrepancies exist in the core, and more importantly the pedestal top region of r/a~0.6-0.8. The different signs in this region suggest either an anomalous convective contribution or a deficiency in the neoclassical model. This is confirmed by the semi-predictive MIST runs illustrated in green in the right-hand frame. Here, the diffusivity was set at the neoclassical value, but the profile of the convective term was adjusted to give agreement with the measured values. One explanation for this anomalous behavior may be ion scale microturbulence. This would be in line with the observation of ion thermal transport in excess

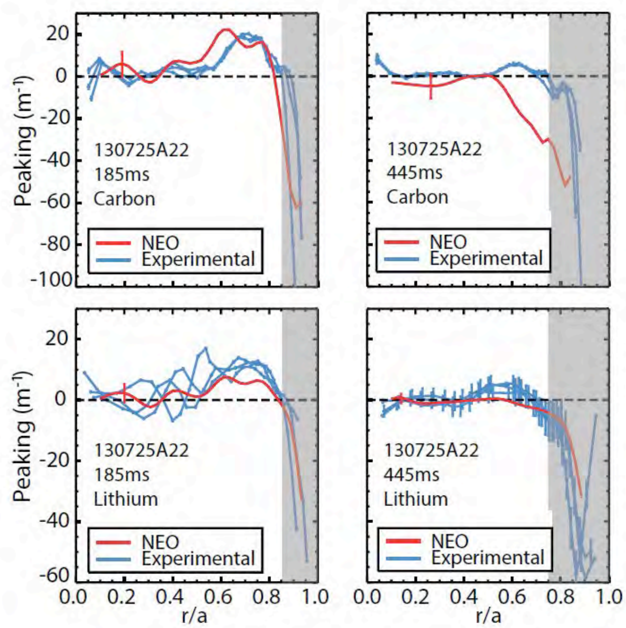

Fig 5.19: Peaking factors for carbon (top) and lithium (bottom) for time early (left) and late (right) in the discharge.

of the neoclassical level in recent low-collisionality lithium conditioned discharges. Alternative explanations include a breakdown in neoclassical theory for large values of ρ_{pol}/L, or uncertainties in the deuterium density profile resulting in errors in the derived impurity transport coefficients.

Fully predictive MIST simulations of these discharges with neoclassical transport coefficients indicated that the profile changes with lithium conditioning do not alone account for the increase in carbon concentration; the lack of ELMs clearly plays a significant role. However, the change in neoclassical transport coefficient leads to a deeper penetration of impurities to the core, where they would be less sensitive to flushing by ELMs. This may explain the observation that even when ELMs were triggered by 3D fields in otherwise ELM-free lithium-conditioned discharges, the core impurity accumulation remained a problem [42-44].

These studies also assessed whether lithium transport showed anomalies similar to that for carbon. Neoclassical calculations with NCLASS and NEO shows that the lithium diffusivity is ~10 times larger than that of carbon, with convective velocities within a factor of 2 of the carbon values across the full profile. These calculations, along with the experimental profiles, allow a comparison of peaking factors in Fig. 5.19. The left side of that figure shows that early in the discharge, the experimental and theoretical peaking factors are in good agreement. At later times, a significant deviation in peaking for carbon is observed. This is similar to that discussed in reference to Fig. 5.18, illustrating the generality of that result. However, the measured lithium peaking follows the neoclassical calculation quite well.

Finally, this research examined the question of whether neoclassical physics alone could explain the significant difference in core concentrations between lithium and carbon $\left(N_{Li}/N_C < 0.01\right)$. The experimental carbon profiles show a decrease of ~100 from r/a=0.8 to r/a=1.0, while lithium density profiles show a smaller decay of a factor of 10. Hence, in appears that differences in the radial transport can only explain up to a factor of 10 in the n_{Li}/n_C ratio, and that differences in the sources profiles and SOL parallel transport likely play a significant roll as well. Considering neoclassical transport only, the density at r/a=0.8, normalized to that at the edge, can be given by $\exp \int_{r/a=1.0}^{r/a=0.8} \left(\upsilon/D\right)_{neo} dr$. By this line of argument, the normalized carbon densities at r/a=0.8 are projected to be between 10 and 1000 times higher than the lithium densities. Hence, neoclassical transport can explain the differences in the impurity concentrations, though the effect is reduced by the apparent non-classical behavior of carbon and differences in the edge sources.

Interested readers should examine Refs [35,63] for more information on these topics, including measurements and modeling of impurity generation and SOL transport.

3.2: Assessing Turbulence in NSTX Lithiated ELM-Free H-modes

The NSTX Beam Emission Spectroscopy (BES) diagnostic [53,54] was designed to study low-k pedestal and core turbulence in a variety of operating modes. In recent analysis, the parametric scaling of both poloidal correlation lengths [66] and turbulent amplitudes [36] with plasma parameters have been studied, and comparisons to gyrokinetic stability calculations have been made [36]. This section summarizes the very recent results on the pedestal turbulent amplitude analysis and stability calculations [36], in order to better understand the transport processes in the high-performance ELM-free pedestal plasma.

The analysis here is taken from>200 ms long windows during ELM-free, MHD quiescent periods of discharges with 700 <I_P [kA]<900 and B_T=0.45 T. All of these discharges had lithium conditioning of the plasma facing components. A total of 129 such data windows are used in the present analysis. The BES signals have been filtered to isolate the 8-50 kHz features. They are used to measure the normalized plasma density fluctuations as

$$\frac{\tilde{n}}{\langle n\rangle_{DC}} = C\frac{\tilde{I}_{D\alpha}}{\langle I_{D\alpha}\rangle_{DC}},$$

where $I_{D\alpha}$ is the measured BES intensity and C=C(E_{NB}, n_e,T_e,Z_{eff}) is given by 2.24. Kinetic profile parameters such as ∇n_e or T_i are inferred from Thomson scattering and CHERS, while equilibrium parameters such as β_P or $\hat{s}$ (magnetic shear) are derived from EFIT reconstructions.

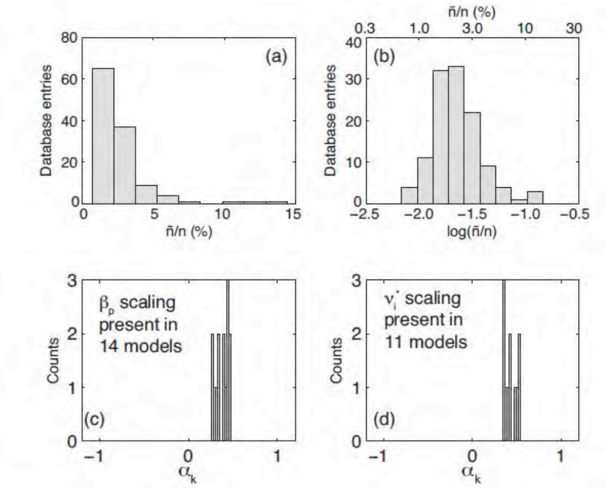

Fig 5.20: distribution of a) δn/n and b) log(δn/n). Also shows are the scalings that emerge from model aggregation for the β_P and v_i dependence of log(δn/n).*

The analysis of this data is done using stepwise multivariate linear regression (SMLR) and model aggregation. Taking y_i as denoting a turbulence characteristic and $x_{k,i}$ as a plasma parameter, the SMLR algorithm finds models in the form

$$\frac{\hat{y}_i - \bar{y}}{\sigma_y} = \sum_k \alpha_k \frac{x_{k,i} - \bar{x}_k}{\sigma_k}.$$

Here, σ are standard deviations, $\hat{y}_i$ are model parameters for turbulence quantities, and the dimensionless α_k parameters are linear scaling coefficients between y_i and $x_{k,i}$ (i indexes database entries and k indexes plasma parameters). The SMLR algorithm minimizes the model's squared sum of errors, by adding or removing parameters x_k such that the inferred significance of each α_k value exceeds 95% [67]. Because many statistically valid models exist in the high-dimensional x_k space, a model aggregation technique is used. This provides i) more parametric scalings than a single model, and ii) a distribution of scaling coefficients that cover a variety of model constraints. More details on the SMLR process as applied to NSTX data can be found in Refs. [66] and [36].

Some inputs and outputs from this process are shown in Fig. 5.20. The top row shows the distribution of $\tilde{n}/n$ and $\log(\tilde{n}/n)$ for the present database. The highly skewed distribution of $\tilde{n}/n$ proved problematic for the SMLR analysis, while fits to $\log(\tilde{n}/n)$ worked well and are used for the analysis below. The bottom two rows show the range of scaling coefficients for β_P and ν_i* from model aggregation. The positive coefficients imply that $\log(\tilde{n}/n)$ does indeed increase with these two parameters.

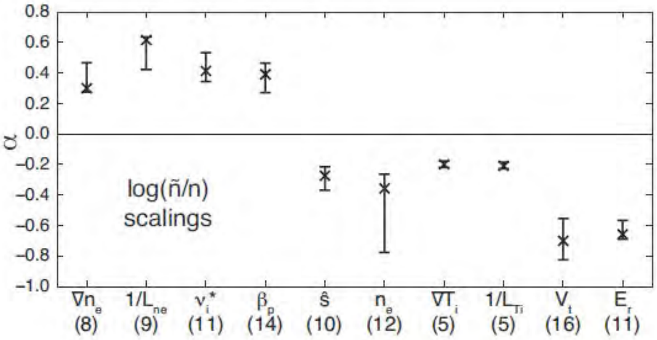

Fig 5.21: 10th to 90th percentile ranges for scalings derived from model aggregation for log(δn/n). α>0 denotes a positive scaling, and the number below each label indicated the number of models that contain the scaling.

A larger set of scaling parameters is shown in Fig. 5.21. Positive scaling of $\log(\tilde{n}/n)$ is observed for ∇n_e, $1/L_{ne}$, ν_i* and β_P. On the other hand, negative scalings were observed with $\hat{s}$, n_e, ∇T_i, $1/L_{Ti}$, V_t, and E_r. The positive scalings with ∇n_e and $1/L_{ne}$ indicate an instability driven by the density gradient, such as the Trapped Electron Mode (TEM) or Kinetic Ballooning Mode (KBM) instability. However, the positive scalings for the density gradient and negative scalings with the ion temperature gradients are notably inconsistent with ion temperature gradient (ITG) driven turbulence; this conclusion is similar to that drawn from the analysis of poloidal correlation lengths using BES [Smith 2012]. Positive scalings with collisionality are consistent with microtearing instabilities, but not drift-wave like turbulence such as ITG or TEM.

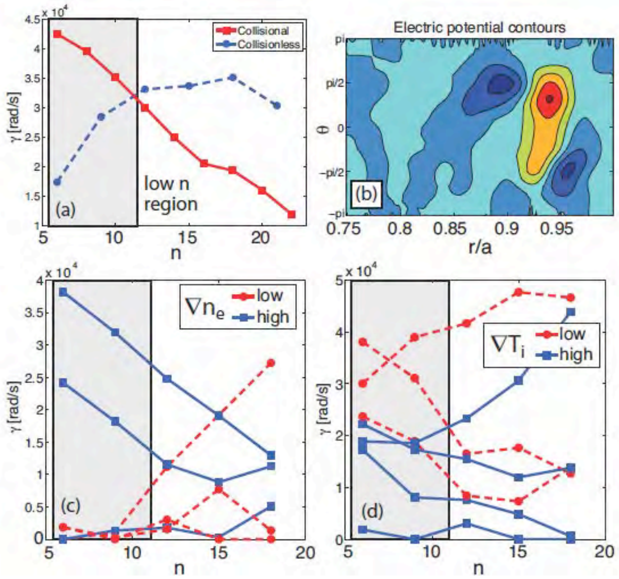

Fig. 5.22: a) simulated growth rates for collisional and collisionless cases as a function of n, b) field aligned electric potential contours. Growth rates then are shown for c) several high and low ∇n_e scenarios, and d) several high and low ∇T_i scenarios. The relevant low-n region is shown on the left in grey in frames a), c) and d).

These experimental results have been compared to results of linear stability calculations with the GEM code [68,69]. These calculations are electromagnetic, collisional, and global in the pedestal, using realistic profiles in the region of interest (0.75<r/a<0.99). They compute the linear stability of modes with 6<n<18 (the n=6-10 modes correspond to $k_\theta \rho_i$~0.2, as typically observed in NSTX).

The results of these calculations are shown in Fig. 5.22. The collisionless and collisional calculations in frame a) show the collisional destabilization of low-n modes, or alternatively, that collisions shift the unstable mode to lower n; this is consistent with the observed positive scaling of $\log(\tilde{n}/n)$ with ν_i* in Figs. 5.20 and 5.21. Fig. 5.22b) shows the field aligned electric field contours, showing a mixed-parity structure (neither pure ballooning nor tearing parity) of the modes. Fig. 5.22c) shows growth rates from several high and low ∇n_e scenarios. These generally show higher low-n growth rates with high ∇n_e consistent with the positive ∇n_e scaling for $\log(\tilde{n}/n)$ in Fig. 5.21. Similarly, frame d) shows that the low-n growth rates are generally higher for low ∇T_i, consistent with the consistent with the negative ∇T_i scaling for $\log(\tilde{n}/n)$ in Fig. 5.21. The consistency between the GEM calculated growth rate trends and the observed ∇n_e, ∇T_i, and ν_i* scalings are quite encouraging, though conclusive identification of turbulent modes active in the pedestal and robust validation of pedestal models requires further analysis.

Interested readers should examine Refs [36,66] for more information on these measurements and calculations, including discussion of the statistical conditioning of the database and of BOUT++ simulations.

4.0 Edge Harmonic Oscillation Observations

As described in detail in the DIII-D section of this report, the attractive QH-mode regime is facilitated by an "Edge Harmonic Oscillation", or EHO. This mode appears to replace ELMs in providing the required particle transport, allowing an ELM free regime with stationary density and impurity content. While QH-mode was first observed in lower density regimes with counter injection, recent research has increased both the density window and co-injection torque for QH operation.

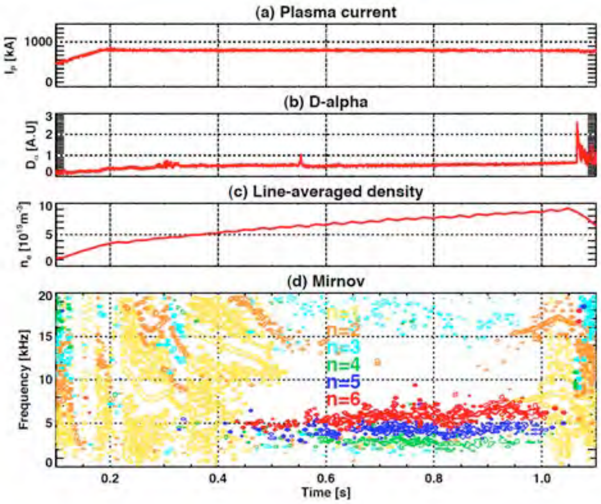

Fig. 5.23: Evolution of a discharge (138239) with observed low-n EHOs.

Motivated by these observations, an effort was made determine if such EHOs may exist in NSTX plasmas. This effort was successful in isolating EHOs, in both small-ELM regimes [70] and ELM-free, high-performance regimes with lithium conditioning [37,38] This report focuses on the latter regime. Unfortunately, the EHOs in NSTX were comparatively weak, and did not result in any observable contribution to the edge particle transport; the electron and carbon densities ramped in these discharges. Hence, the study here will focus on aspects of the mode dynamics, and then on potential methods to drive the modes to larger amplitude in NSTX-U.

4.1: Observation of EHOs in NSTX Lithiated Discharges

4.1.1: Mode dynamics and structure

The general features of a discharge with EHOs are illustrated in Fig. 5.23 [37,38]. The upper frames show the plasma current, D_α emission from the lower divertor, and line average density. No ELMs are observed in this discharge, and, as noted above, the density increases throughout the discharge. The lower frame shows the spectrogram from wall-mounted Mirnov coils. The phase between 0.6 and 1.0 seconds is free of large amplitude n=1 and n=2 modes, which generally have a large impact on the plasma rotation and are often disruptive. However, a series of n=4-6 modes are clearly visible. These are the modes that are labeled as “EHOs” in the present research.

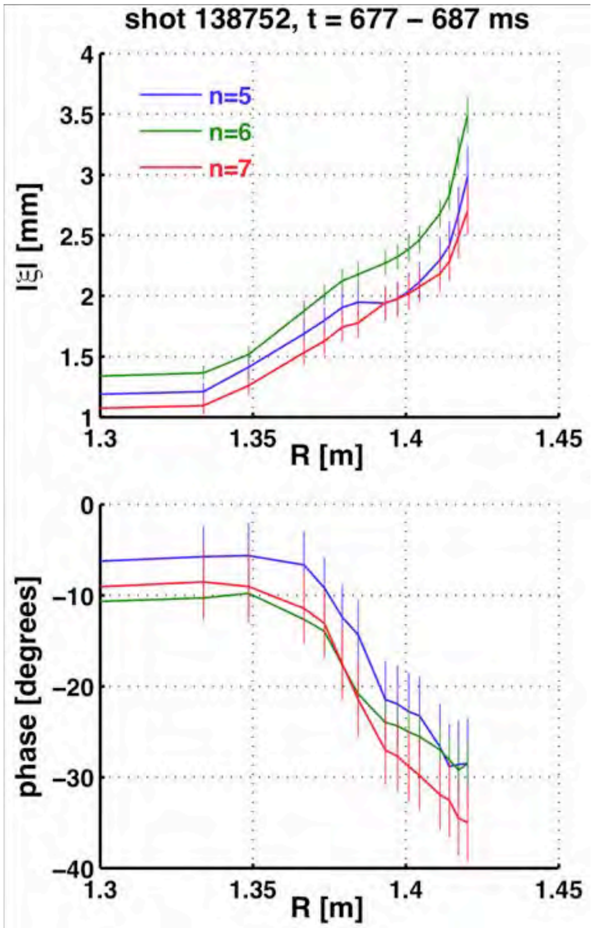

Fig. 5.24: Amplitude and phase of observed EHOs, as measured by the reflectometers. The separatrix is at 1.42 m in this discharge (138752).

These modes can be observed in the spectrograms of many other diagnostics, including edge soft X-rays when configured for low-energy emission measurements and Langmuir probes in the SOL near the outer strikepoint [37,38]. The low frequency of the modes, and their observation in diagnostics that are sensitive to the plasma edge, provides indication that the modes are indeed located in the vicinity of the separatrix.

In order to better assess the structure of these modes, their signature in the edge reflectometer [71] has been assessed. Fig. 5.24 shows the mode amplitude and phase for a discharge where the outer midplane separatrix is located at R=1.42 m. It is clear from the top frame that the mode displacements are in the range of 2-4 mm, and are peaked at the plasma edge. The different mode harmonics are also highly coherent, as indicated by the bottom frame.

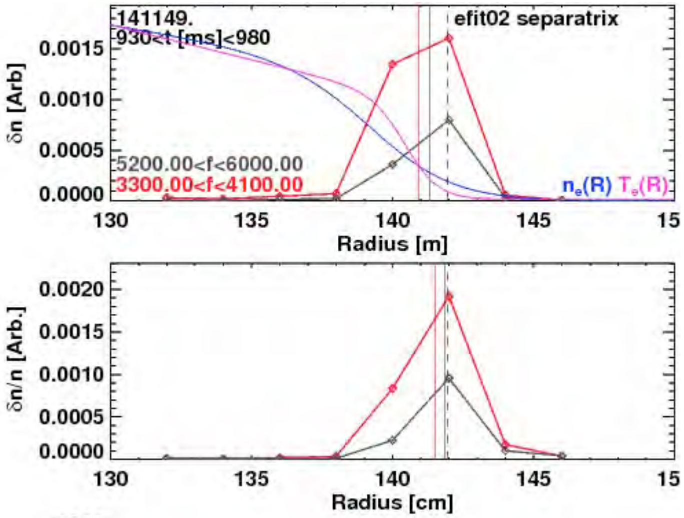

Fig. 5.25: Profiles of the BES fluctuation amplitude (proportional to δn_e) (top), and the amplitude normalized to the DC level (proportional to $\delta n_e/n_e$) (bottom). Both metrics show that the mode is localized to the plasma edge. The top frame additionally shows the tanh fit to the density and temperature profiles during this time period. The red curve is for an n=3 mode, while the black curve is for the n=4 EHO.

The edge-localized nature of these modes has been assessed via the NSTX BES [53,54] diagnostic as well; this data is available for a subset of the discharges where EHOs were previously identified. Figure 5.25 illustrates typical BES data for one of these modes. The top frame shows the radial profile of the density fluctuations, for peaks at ~3700 Hz and 5500 Hz. The primary fluctuation is localized to a just a few channels. The EFIT separatrix is shown as a dashed line, implying that the mode peak amplitude is at the separatrix. Note, however, that the separatrix location from these reconstructions is accurate to ~1 cm. Hence, the tanh fits to the density and temperature profile are also shown in the top frame. By comparing the fluctuation amplitude profile to the equilibrium profiles, it becomes clear that these modes are indeed located at the bottom of the pedestal, consistent with the reflectometer data. The lower frame of this figure shows the same fluctuation data, but with the fluctuation amplitudes normalized to the DC amplitude. This quantity is proportional to δn/n, and retains the strong peak at the bottom of the pedestal.

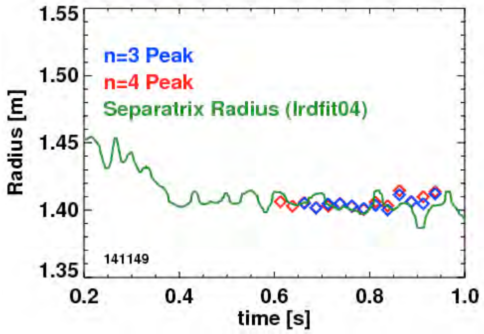

Fig. 5.26: Time evolution of the EHO peak amplitude radius and the separatrix radius.

The location of peak BES amplitude has been tracked, using the metric $R_{peak} = \sum R_i \frac{\delta I_i}{I_i} \Big/ \sum \frac{\delta I_i}{I_i}$. The result of such an exercise is shown in Fig. 5.26, which illustrates the positions of both the n=3 and 4 peak amplitudes as a function of time. As anticipated, they modes are located very near the separatrix for the duration of their existence.

4.1.2: Operational space for EHOs in NSTX

A Significant effort was dedicated to finding parameters where EHOs were possible in NSTX. However, clear trends were hard to find. Some observations include:

- Discharges with EHOs tended to have fairly large plasma wall gaps. No EHO discharge had an outboard plasma-wall gap less than 13 cm.
- Discharges with I_P=800kA were most likely to have EHOs. Higher plasma currents tended to eliminate EHO activity.
- There is some evidence that edge rotation shear in the range of -300 to -200 kHz/m may be favorable for EHO formation (see Figure 4 of Ref. [38]).

4.1.3: Peeling Ballooning Space

As part of the analysis of these cases, the peeling-ballooning stability [72] of these discharges was analyzed. This analysis used highly constrained kinetic EFITs as input to stability analysis with the MHD stability code ELITE [72]. In particular, once the equilibrium was reconstructed, variations in the edge pressure gradient (α) and current density were imposed to compute a family of nearby equilibria, with ELITE run for the full set of cases.

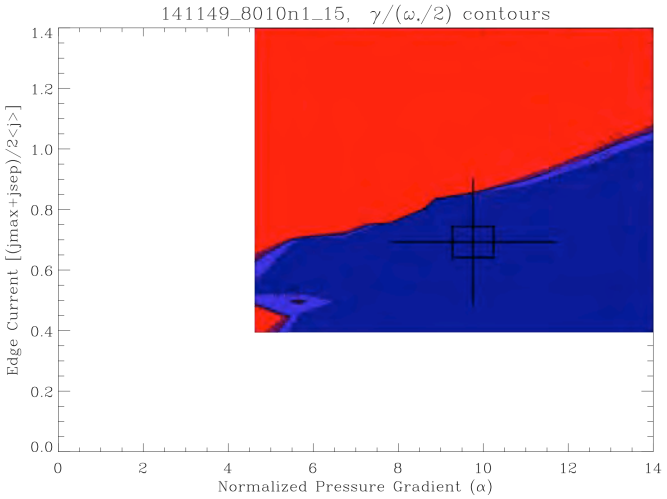

Fig. 5.27: ELITE calculation of the pedestal stability for a case with observed edge harmonic oscillations.

The results of this study are shown in Fig. 5.27, for the discharge 141149 discussed in Section 4.1.1. Blue indicates the stable region in this plot, while red indicates unstable configurations. The large cross indicates the experimental location of the discharge in this parameter space. The ballooning boundary, at large pressure gradient, is not visible in this diagram, as is often the case in NSTX [70] and other low aspect ratio configurations [73]. On the other hand, the peeling boundary, at large current density, is clearly visible. The experimental point resides near the peeling boundary. This is quite similar to the case of QH-mode in DIII-D, where the relaxed pedestal operating point is near the peeling boundary [74].

4.2: Prospects for Actively Driving EHOs in NSTX-U

It is conceivable that the lower collisionality pedestals of NSTX-U will result in stronger EHOs, potentially leading to a QH-mode like configuration. However, rather than rely on this assumption, recent efforts have attempted to assess if EHOs can be actively driven [37,38].

The method assumed in this study relies on use of the 12-strap NSTX-U High Harmonic Fast Wave antenna, shown in the bottom left of Fig. 5.28. The recent upgrade to a center-grounded configuration allows the top and bottom of each strap to be independently fed. An example configuration for EHO studies is shown in the upper left of Fig 5.28, where six of the available 12 straps are used, with odd parity about both the midplane and a line separating groups of three straps. Other configurations of current polarities are of course possible, as will be described below. The right portion of Fig. 5.28 illustrates the 3D NSTX plasma cross-section, along with the RWM coils in red and blue and the model shapes for the HHFW antenna straps in black. Compared to the RWM coils, which are located outside the vacuum chamber, these straps are capable of producing higher toroidal mode number perturbations due to their smaller toroidal extent, and higher frequency perturbations due to their location inside the vacuum chamber. Engineering considerations related to powering the straps for this application, while important, are not considered in this report.

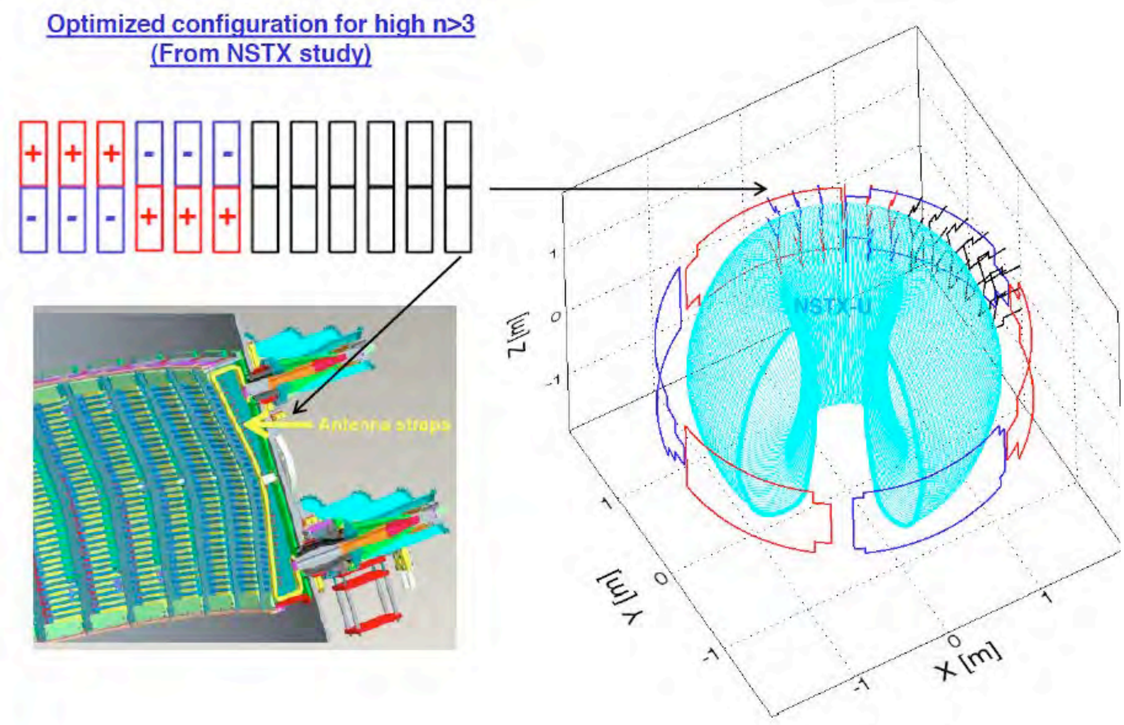

Fig. 5.28: NSTX-U antenna configuration for the driven EHO study. The upper left shows a schematic indication of the current polarities,, the lower left shows the mechanics of the current straps themselves, while the right figure shows the NSTX-U plasma boundary, the RWM coils (red and blue), and the modeled HHFW antennas (black).

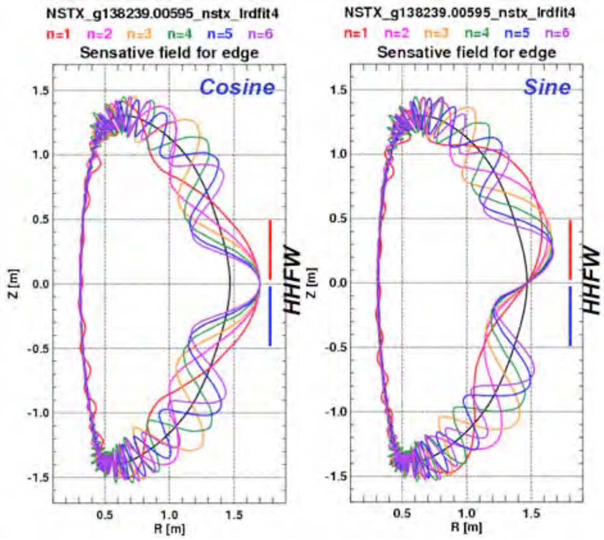

Fig 5.29: Dominant field component for n=1 to 6 perturbations, for a typical NSTX equilibria.

In order to assess the efficiency of driving edge perturbations with this antenna, the dominant external field for coupling to the plasma [75,76] is determined by the IPEC [77] code. This analysis essentially determines the configuration of the HHFW antenna currents that can most efficiently couple to the plasma and generate 3D distortions. As an example of this analysis, the dominant external field for each toroidal mode number n [37,38] is shown in Fig. 5.29. It is clear that the HHFW antenna will most easily couple to the sine part of the higher-n components, as its poloidal extent is comparable to the extent of the dominant field on the outboard side.

As part of an optimization study, 20-30 different combinations of antenna strap currents were tested for their coupling to the plasma via this overlap metric. The currents in each strap were always the same, and only the polarities varied. This constraint could be removed, through at the expense of more sophisticated power supplies. Fig. 5.30 shows in black the overlap field for the configuration that maximizes coupling to n=5 & 6 for the NSTX equilibrium (138239, q_{95}=9.3). Further, as shown in Ref. [37,38], the n≤3 part can be largely eliminated by the external RWM coils for low enough driving frequencies.

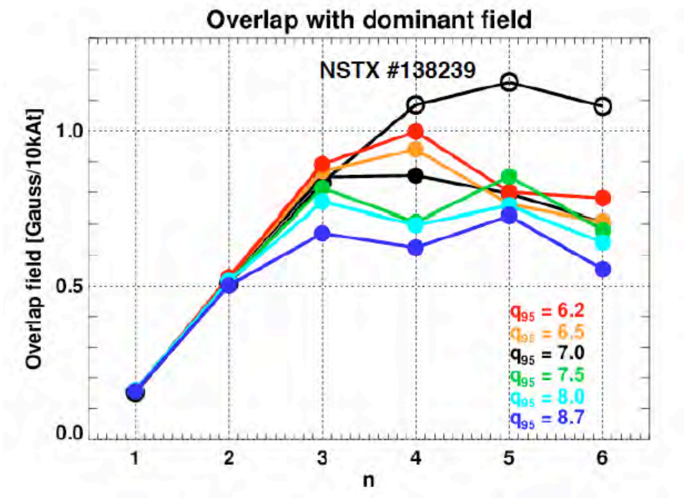

Fig. 5.30: Overlap of the applied field with the dominant field component as a function of toroidal mode number, for an NSTX-U q_{95} scan using model equilibria. The results for an NSTX case are also illustrated as the topmost black curve.

Fig. 5.31 connects the IPEC calculations back to the reflectometry measurements. The black points are the displacements for the n=6 reflectometry data, shown above in Fig. 5.24. The black lines show the displacement profile for 1 kA of current in the HHFW antenna straps. It is clear that currents at that level, which are comparable to both the RF currents and the currents driven in the RWM coils, could produce displacements comparable to those naturally occurring. Hence, for somewhat larger currents, it may be possible to drive the modes beyond their present amplitude, potentially leading to beneficial changes in the edge plasma.

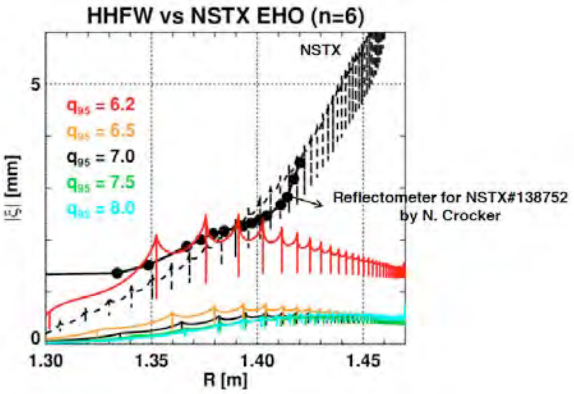

Fig 5.31: Measured displacements from reflectometery, overlaid on potential displacements for a single NSTX equilibrium and the NSTX-U q_{95} scan.

As a complement to the research presented in Ref. [37,38], these IPEC calculations were repeated for typical NSTX-U equilibria, over a range of q_{95}. The boundary shapes for these equilibria are shown in Fig. 5.32; these are high elongation and high triangularity equilibria of the type predicted to maximize the non-inductive fraction in NSTX-U [78]. β_N was fixed at 4.0 for all cases.

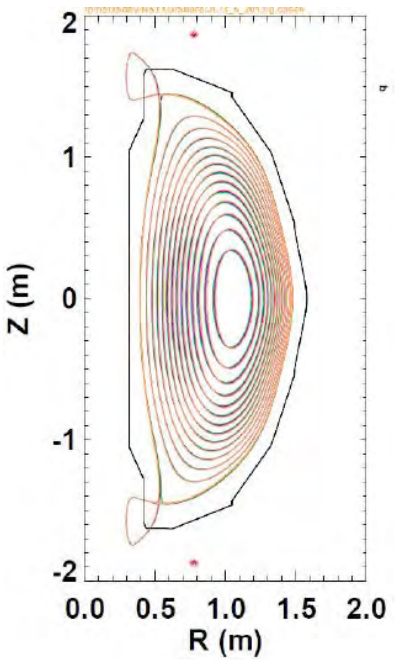

Fig. 5.32: NSTX-U equilibria for the q_{95} scan used in the IPEC study.

The coupling to the dominant external fields for these cases is shown in Fig. 5.30. The coupling magnitudes are similar to those computed for NSTX, especially for the lower q_{95} example. However, at higher q_{95}, the coupling falls off. As a consequence, Fig. 5.31 shows that the displacements at the plasma edge anticipated from 1 kA of current in the antenna are comparable to that achieved in NSTX for q_{95}=6, but become smaller as q_{95} is increased.

Hence, for the present configuration at β_N=4, it is anticipated that the technique will likely only drive large displacements at lower q_{95}. Furthermore, for this family of equilibria, it appears that it may be difficult to drive significant perturbation amplitudes with the existing antenna structure. However, the present cases are stable to n≥4 perturbations, even without a conducting wall. It is anticipated that if the β_N value is further raised, a larger plasma response may occur, potentially facilitating edge control with the HHFW antenna. The β_N dependence of this coupling will be explored in future studies.

Acknowledgement

This research was sponsored by the United States Department of Energy under contracts DE-AC05-00OR22725, DE-FG02-99ER54527, DE-SC0001288, DE-FG02-09ER55012 and DE-AC02-09CH11466.

References

[1] P.T. Lang, et al., Nuclear Fusion **53**, 043004 (2013).
[2] P. T. Lang, et al, Nuclear Fusion **44**, 665 (2004).
[3] P.T. Lang, et al., Nuclear Fusion **47**, 754 (2007).
[4] P.T. Lang, et al., Nuclear Fusion **48**, 095007 (2008).
[5] P.T. Lang, et al., Nuclear Fusion **51**, 033010 (2011).
[6] L.R. Baylor, et al., Phys. Rev. Lett. **110**, 245001 (2013).
[7] A. W. Degeling, et al., Plasma Phys. Control Fusion **45**, 1637 (2003).
[8] P. T. Lang, et al, Plasma Phys. Control. Fusion **46**, L31 (2004).
[9] F. Sartori, et al., *Synchronous ELM Pacing at JET Using the Vertical Stabilization Controller*, 35th EPS Conference on Plasma Physics, Hersonissos, Crete, Greece (2008).
[10] E. de la Luna, et al., "Effect of ELM Mitigation on Confinement and Divertor Heat Loads on JET, paper EXC/8-4, IAEA FEC (2010), Deajeon, Korea.
[11] E. de la Luna, et al., "Magnetic ELM triggering using the vertical stabilization controller in JET", P-5.174, 36th EPS Conference on Plasma Physics (2009), Sofia, Bulgaria.
[12] S.P. Gerhardt, et al., Nuclear Fusion **50**, 064015 (2010).
[13] T. E. Evans, et al., Nature Physics **2**, 419 (2006).
[14] M.E. Fenstermacher, et al., Nuclear Fusion **48**, 122001 (2008).
[15] T.E. Evans, et al., Nuclear Fusion **48**, 024002 (2008).
[16] P.B. Snyder, et al., Phys. Plasmas **19**, 056115 (2012).
[17] K.H. Burrell, et al., Phys. Plasmas **12**, 056121 (2005).
[18] K.H. Burrell, et al., Nuclear Fusion **49**, 085024 (2009).
[19] A.M. Garofalo, et al., Nuclear Fusion **51**, 083018 (2011).
[20] K.H. Burrell, et al., Phys. Plasmas **19**, 056117 (2012).
[21] K.H. Burrell, et al., Nuclear Fusion **53**, 073038 (2013).
[22] W. Suttrop, et al., Plasma Phys. Controlled Fusion **45**, 1399 (2003).
[23] Y. Sakamoto, et al, Plasma Phys. Controlled Fusion **46**, A299 (2004).
[24] N. Oyama, et al., Nuclear Fusion **45**, 871 (2005).
[25] W. Suttrop, et al., Nuclear Fusion **45**, 721 (2005).
[26] F. Ryter, et al., Plasma Phys. Control. Fusion **40**, 725 (1998).
[27] R. McDermott, et al., Phys. Plasmas **16**, 056103 (2009).
[28] D. Whyte, et al., Nuclear Fusion **50**, 105005 (2010).
[29] A.E. Hubbard, et al., Phys. Plasmas **18**, 056115 (2011).
[30] A.E. Hubbard, et al., Nuclear Fusion **52**, 114009 (2012).
[31] J.W. Hughes, et al., Nuclear Fusion **53**, 043016 (2013).
[32] R. Maingi, et al., Journal of Nuclear Materials **390-391**, 440 (2009).
[33] R. Maingi, et al., Phys. Rev. Lett. **105**, 135004 (2010).
[34] D.K. Mansfield, et al., Journal of Nuclear Materials **390-391**, 764 (2009).

[35] F. Scotti, et al., *Core Transport of Lithium and Carbon in ELM-free Discharges with Lithium Wall Conditioning in the NSTX*, submitted to Nuclear Fusion (2013).
[36] D.R. Smith, et al., *Measurements and simulations of low wavenumber pedestal turbulence in the National Spherical Torus Experiment*, submitted to Nuclear Fusion (2013).
[37] J.-K. Park, et al., *Observation of Edge Harmonic Oscillation in NSTX and Theoretical Study of Its Active Control Using HHFW Antenna at Audio Frequencies*, paper EX/P4-33, IAEA Fusion Energy Conference 2012, San Diego, USA.
[38] J.K. Park, et al., *Observation of EHO in NSTX and theoretical study of its active control using HHFW antenna*, submitted to Nuclear Fusion.
[39] D. Boyle, et al., Plasma Phys. Control. Fusion **53**, 105011 (2011).
[40] R.E. Bell, et al., Phys. Plasmas **17**, 082057 (2010).
[41] R.E. Waltz and R.L. Miller, Phys. Plasmas **6**, 4265 (1999).
[42] J. M. Canik, et al., Phys. Rev. Lett. **104**, 045001 (2010).
[43] J.M. Canik, et al., Nuclear Fusion **50**, 064016 (2010).
[44] J.M. Canik, et al., Nuclear Fusion **50**, 034012 (2010)
[45] J.E. Menard, et al., Nuclear Fusion **50**, 045008 (2010).
[46] R. J. Hawryluk, et al., "An Empirical Approach to Tokamak Transport", in Physics of Plasmas Close to Thermonuclear Conditions, ed. by B. Coppi, et al., (CEC, Brussels, 1980), Vol. 1, pp. 19-46.
[47] L.L Lao, Nuclear Fusion **25**, 1611 (1985).
[48] S.A. Sabbagh, et al., Nuclear Fusion **41**, 1601 (2001).
[49] S.A. Sabbagh, et al., Nuclear Fusion **46**, 635 (2006).
[50] J.E. Menard, et al., Phys. Rev. Lett. **97**, 095002 (2006).
[51] B.P. LeBlanc, et al., Rev. Sci. Instrum. **74**, 1659 (2003).
[52] R.E. Bell and R. Feder, Rev. Sci. Instrum. **81**, 10D724 (2009).
[53] D.R. Smith, et al., Rev. Sci. Instrum. **81**, 10D717 (2010).
[54] D.R. Smith, et al., Rev. Sci. Instrum. **83**, 10D502 (2012).
[55] S.P. Gerhardt, et al., Nuclear Fusion **53**, 043020 (2013).
[56] C.S. Chang, S. Ku, and H Weitzner, H. Physics of Plasmas **11**, 2649 (2004).
[57]M. Kotschenreuther *et al*, Comput. Phys. Commun. **88** (1995) 128.
[58] J.M. Canik, et al., “Edge microstability of NSTX plasmas without and with lithium-coated plasma-facing components”, Nuclear Fusion at press.
[59] R. Maingi, et al., Nuclear Fusion **52**, 083001 (2012).
[60] M.G. Bell, et al, Plasma Phys. Control. Fusion **51**, 12 (2009).
[61] R. Maingi, et al., Phys. Rev. Lett., **103**, 075001 (2009).
[62] M. Podesta, et al., Nuclear Fusion **52**, 033008 (2012).
[63] F. Scotti, *Modification of impurity sources and transport with lithium wall conditioning in the National Spherical Torus Experiment*, Ph.D dissertation, Princeton University, Department of Astrophysics (2013).
[64] E.A. Belli, et al, Plasma Phys. Control. Fusion **50**, 095010 (2008).
[65] W.A. Houlberg, et al., Phys. Plasmas **4**, 9 (1997).
[66] D.R. Smith, et al., Phys. Plasmas **20**, 055903 (2013)
[67] M. Kutner, et al., *Applied Linear Statistical Models*, 5th ed. (McGraw-Hill, 2005)
[68] Y. Chen and S. Parker, J. Comput. Phys. **220**, 839 (2007).
[69] W. Wan, et al., Phys. Plasmas **18**, 056116 (2011).

[70] A.C. Sontag, et al., Nuclear Fusion **51**, 103022 (2011)
[71] N. Crocker, et al, Plasma Phys. Control. Fusion **53**, 105001 (2011).
[72] P.B. Snyder, et al., Phys. Plasmas **9**, 2037 (2002).
[73] P.B. Snyder, et al., Plasma Phys. Control. Fusion **46**, A131 (2004).
[74] P.B. Snyder, et al., Nuclear Fusion **47**, 961 (2007).
[75] J.-K. Park, et al., Nuclear Fusion **48**, 045006 (2008).
[76] J.-K. Park, et al., Nuclear Fusion **51**, 023003 (2011).
[77] J.-K. Park, et al., Phys, Plasmas **14**, 052110 (2007).
[78] S.P. Gerhardt, et al., Nuclear Fusion **52**, 083020 (2012).

Appendix — XGC0 Neoclassical Ion Transport Calculations for QH-mode – D. Battaglia

1.0 Introduction

The goal of the work described below is to begin testing whether neoclassical ion transport plays a significant role in the physics controlling the particle transport in the edge pedestal plasma under QH-mode operation. For the work described here the XGC0 Particle-in-Cell (PIC) code was used to simulate a QH-mode plasma shot from DIII-D and compare the calculated neo-classical ion transport to experimental measurements.

XGC0 is a code that leverages high-performance computing to calculate the self-consistent full-f drift-kinetic solution for ion transport in the H-mode pedestal using a realistic diverted magnetic geometry and Monte Carlo neutral recycling model. The large computational resources required to solve the full-f solution is justified on the observation that kinetic ion effects (such as ion orbit loss and finite orbit effects) have significant impacts on the ion thermal, particle and momentum transport in the H-mode pedestal and scrape-off layer.

The code was recently updated to enable quantitative comparison to experimental measurements in order to evaluate the role of axisymmetric neoclassical transport in various H-mode transport regimes. These updates include: (1) addition of impurity ions to the simulation since most ion diagnostics measure the properties of plasma impurities, (2) synthetic diagnostics for typical profile diagnostics on NSTX and DIII-D, such as charge-exchange spectroscopy and Thomson scattering, and (3) improved code diagnostics that track the contributions of different transport processes on the energy, particle and momentum balance.

The ability to quantitatively compare the simulation to experimental measurements has enabled XGC0 to be used as an interpretative transport model. Ad-hoc anomalous transport is added to the neoclassical transport level if it is needed to improve the agreement between the simulation and experimental measurements.

2.0 QH-mode

Interpretative XGC0 was used to investigate the neoclassical ion transport in a steady-state counter-injection QH-mode discharge that obtained high-spatial-resolution edge pedestal measurements using an outboard edge sweep (discharge 106999).

Large anomalous particle, energy and momentum transport (~1 m^2/s) is required from the inner boundary of the simulation to the top of the pedestal ($\psi_N < 0.94$), suggestive of ion-scale turbulent transport (Fig. B-1). The requirement of large anomalous transport levels in the region of shallow gradients at the top of the pedestal is consistent with XGC0 simulations of DIII-D H-mode pedestals.

The unique observation from this QH-mode simulation compared to H-mode simulations is that an anomalous co-I_p torque of about 0.5 Nm is required from $0.93 < \psi_N < 0.96$ (inside edge of E_r well). This region corresponds to the location of the maximum EHO oscillations as determined from experimental measurements. The NTV-like induced drag on the counter rotation drives E_r positive and increases the neoclassical ion particle transport (where the impact on the particle transport rate increases with the ion charge) by reducing the "potential cliff" the ions encounter as they move radially outward through the pedestal. The increase in the neoclassical particle transport reduces the density gradient (especially the impurity density gradient) at the top of the pedestal and may provide a mechanism for regulating the pedestal pressure at the peeling-ballooning stability limit.

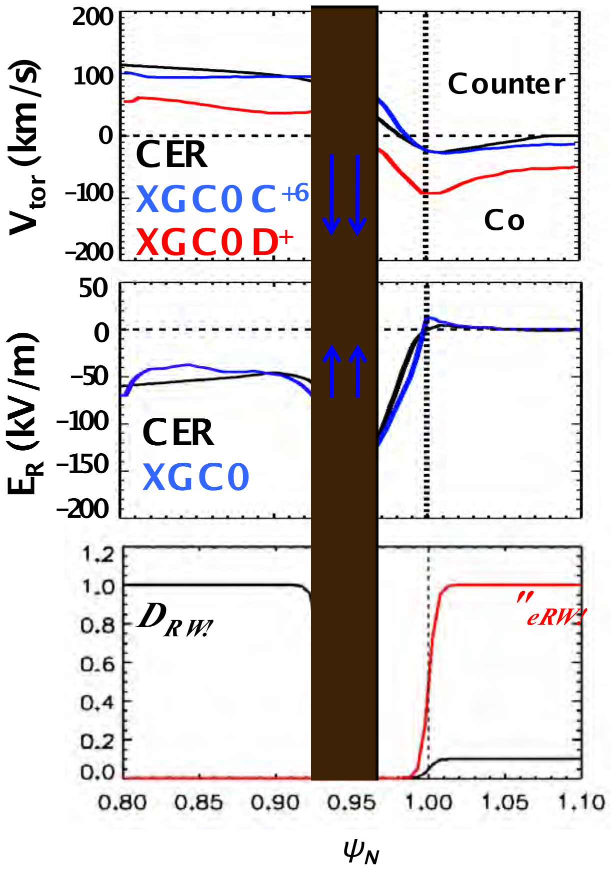

Fig. B-1. (Top) Simulated ion toroidal flows at the outboard midplane (red and blue) compared to the experimental measurement for C^{+6} (black). (Middle) XGC0 simulated E_r at the outboard midplane (blue) compared to the experimental measurement (black). (Bottom) Anomalous particle (black) and electron thermal (red) transport random walk (RW) added to the neoclassical transport in the simulation. Yellow shaded box indicates the region where 0.5 Nm of co-I_p torque is applied to improve the agreement between the simulated profiles and the experimental measurements.

3.0 Conclusions

The work with XGC0 has indicated that the local change in rotation, transport and the radial electric field induced by the EHO at the top of the pedestal can reduce the global particle confinement, especially impurity confinement. It also has indicated that the modification of the neoclassical transport in the pedestal by the EHO reduces the pressure gradient and bootstrap current, contributing to the mechanisms that regulate the growth of the peeling instability.

Reference

Chang, C.S., Ku, S., and Weitzner, H., Phys. Plasmas **11**, 2649 (2004).